AN EXAMINATION OF THE POTENTIAL AND LIMITATIONS OF OPTICAL REMOTE SENSING IN MONITORING SUBMERGED AQUATIC VEGETATION

Gillian S.L. Rowan

Department of Geography

McGill University

Montreal, Quebec Canada

August 2021

A thesis submitted to McGill University

In partial fulfillment of the requirements of the degree of

Master of Science

Abstract

Aquatic vegetation is a critical component of freshwater ecosystems, providing habitat for small fish and invertebrates, stabilizing sediments, altering flow regimes, and improving water quality. Vegetation communities are, however, facing new and escalating pressures due to climate change and increased human disturbances. Monitoring and managing these ecosystems are therefore vital if the services aquatic plants afford are to be maintained. Remote sensing has been suggested as a preferred method to monitor these habitats, but the technology hasn't yet seen extensive implementation particularly to submerged aquatic vegetation (SAV) in the freshwater context. The goal of this thesis is to facilitate the application of remote sensing techniques to SAV monitoring through both information transfer and filling in foundational knowledge gaps in the field. A systematic literature review was conducted of previous work in SAV monitoring using remote sensing, which was synthesized with relevant general principles of remote sensing, to create a resource for ecosystem managers and ecological researchers unfamiliar with the discipline. This resource provides an overview of all aspects of a typical optical remote sensing workflow, concentrating on applications to SAV monitoring, to instruct non-specialists in whether and how to adopt remote sensing as a research method. The majority of previous work focused on coastal systems and primarily on determining community extent. While these applications did produce moderate to good results, the narrow scope of the data precludes many critical ecosystem management and research questions from being answered. For this reason, original research was undertaken to implement optical remote sensing techniques to a larger range of targets in a non-ideal (i.e., freshwater) environment. This work assessed the spectral separability of targets under laboratory conditions at various grouping levels (i.e., species to kingdom, vegetation/non-vegetation), under multiple sampling conditions, and modelled across spectral resolutions. In situ imagery was additionally analyzed to compare the expected modelled accuracy to what is possible under field conditions. Samples from thirteen species of SAV were collected across two seasons and were found to be spectrally separable (leave-one-out nearest neighbour criterion of 0.8 to 1 depending on grouping) during the peak of the growing season. Spectral separability depended directly on the spectral resolution and number of bands of the sensor chosen. Airborne hyperspectral imagery was effective with individual class recall of up to 100%, and overall recalls of 88% and 94% when detecting vegetation types and between vegetation or non-vegetation, respectively. Image analysis was

limited to targets of canopy-forming or carpeting vegetation and large unvegetated patches due to the ~ 1 m spatial resolution. The targets present in this freshwater ecosystem would be conducive to mapping and monitoring using remote sensing techniques, however, imagery of the spatial and spectral resolution required for such applications is expensive and not widely available. Development of targeted and sufficiently high-spatial resolution sensors aboard space-borne platforms should therefore be prioritized if aquatic vegetation is to be effectively monitored at the regional to global scales.

Résumé

La végétation aquatique est une constituante essentielle des écosystèmes d'eau douce, fournissant un habitat pour la faune, stabilisant les sédiments, modifiant les régimes d'écoulement et améliorant la qualité d'eau. Les communautés végétales sont cependant sujets à de nouvelles pressions croissantes en raison du changement climatique et des perturbations humaines accrues. La surveillance et la gestion de ces écosystèmes sont donc essentielles pour le maintien des services rendus par les plantes aquatiques. La télédétection est suggérée comme méthode préférée pour surveiller ces habitats, mais la technologie n'a pas encore été mise en œuvre à grande échelle, en particulier pour la végétation aquatique submergée (VAS) dans le contexte de l'eau douce. L'objectif de cette thèse est de faciliter l'application des techniques de télédétection à la surveillance des VAS en transferant les informations de façon amenable aux non-specialistes et en addressant les lacunes dans les connaisances scientifiques actuelles. Une revue systématique de la littérature a été menée sur les travaux de surveillance des VAS à l'aide de la télédétection, ce qui a été synthétisée avec les principes généraux de la télédétection, afin de créer une ressource pour les gestionnaires d'écosystèmes et les chercheurs en écologie peu familiers avec la discipline. Cette resource touche sur tous les aspects d'un méthodologie de télédétection optique typique, avec une attention particulière sur la surveillance de la VAS, pour indiquer aux non-spécialistes si, et comment, adopter la télédétection dans leurs recherches. La majorité des travaux antérieurs se sont concentrés sur les systèmes côtiers marins et principalement sur la détermination de l'étendue des communautés végétales. Bien que ces applications aient produit des résultats de precision de modérés à bons, la portée étroite des données empêche de répondre à de nombreuses questions critiques de gestion des écosystèmes. Pour cette raison, des recherches originales ont été entreprises pour mettre en œuvre des techniques de télédétection optique sur un plus grand nombre de cibles dans un environnement non ideal, c'est-à-dire en eau douce. Ce travail a évalué la séparabilité spectrale des vegetaux sous conditions de laboratoire à divers niveaux de regroupement. L'imagerie in situ a été analysée pour comparer la précision modélisée attendue à ce qui est possible dans des conditions de terrain. Des échantillons de treize espèces de VAS ont été collectés sur deux saisons et se sont avérés etre spectralement séparables (critère de voisin-le-plus-proche de 0,8 à 1, selon le groupe) pendant l'apogee de la saison de croissance. La séparabilité spectrale dépendait directement de la résolution spectrale et du nombre de bandes du capteur choisi. L'imagerie hyperspectrale a été

efficace, avec un rappel de classe individuelle allant jusqu'à 100 % et des rappels globaux de 88 % et 94 % lors de la détection des types de végétation et entre la végétation ou la non-végétation, respectivement. L'analyse des images était limitée aux cibles de végétation formant des canopées ou en tapis et aux grandes parcelles sans végétation en raison de la résolution spatiale d'environ 1 m. Les cibles présentes dans cet écosystème d'eau douce seraient propices à la cartographie et à la surveillance à l'aide de techniques de télédétection, cependant, l'imagerie de la résolution spatiale et spectrale requise pour de telles applications est coûteuse et peu disponible. Le développement de capteurs ciblés et à résolution spatiale suffisamment élevée à bord de plates-formes spatiales devrait donc être une priorité si l'on veut surveiller efficacement la végétation aquatique aux échelles régionales et mondiale.

Table of Contents

List of tables

List of figures

List of abbreviations

6SV	Second Simulation of the Satellite Signal in the Solar Spectrum (Vermote et al., 1997)
ACE	Adaptive Coherence Estimator
AISA	Airborne Imaging Spectrometer for Applications
ANOVA	Analysis Of Variance
ASD	Applied Spectrographic Devices
ATM	Airborne Thematic Mapper
AUV	Autonomous Underwater Vehicle
AVHRR	Advanced Very High Resolution Radiometer
AVIRIS	Airborne Visible/Infrared Imaging Spectrometer
Bio-ORACLE	Bio-Ocean Rasters for Analysis of Climate and Environment
CASI	Compact Airborne Spectrographic Imager
CDOM	Coloured Dissolved Organic Matter
Chl-a	Chlorophyll-a
CIR	Colour Infra Red
COCI	Coastal Ocean Color Imager
CSA	Canadian Space Agency
CVA	Change Vector Analysis
DEM	Digital Elevation Model
DHPC	Directly-georeferenced Hyperspectral Point Cloud
DHPC	Directly-Georeferenced Point Cloud
DII	Depth Invariant Index

DN	Digital Number
ELM	Emipiric Line Method
ETM+	Enhanced Thematic Mapper plus
FDSC	Feature Dissimilarity Space Classifier
FWHM	Full Width Half Max
GCP	Ground Control Point
GNSS	Global Navigation Satellite System
GPS	Global Positioning System
GRVI	Green-Red Vegetation Index
HJ-CCD	Huan Jing - Charge-Coupled Device
HSI	Hyperspectral Imagery
IFRR	In-Flight Radiometric Refinement
IMU	Inertial Measurement Unit
INS	Inertial Navigation System
IR	Infra Red
LED	Light-Emitting Diode
libRadtran	library for radiative transfer
LiDAR	Light Detection And Ranging
LNN	Leave-one-out Nearest Neighbor
MERIS	MEdium Resolution Imaging Spectroradiometer
MiDAR	Multispectral Imaging, Detection and Active Reflectance
MIVIS	Multispectral Infrared and Visible Imaging Spectrometer

MNF	Minimum Noise Fraction
MODIS	MODerate resolution Imaging Spectroradiometer
MODTRAN	MODerate resolution atmospheric TRANsmission
MSI	Multispectral Imagery
MSS	Multispectral Scanner System
NASA	National Aeronautics and Space Administration
NDAVI	Normalized Difference Aquatic Vegetation Index
NDVI	Normalized Difference Vegetation Index
NIR	Near Infra Red
NPCI	Normalized total Pigment to Chlorophyll-a ratio Index
NRC-FRL	National Research Council of Canada – Flight Research Laboratory
NTRIP	Networked Transport of RTCM via Internet Protocol
NUSVC	Nu-Support Vector Machine
OBIA	Object-Based Image Analysis
OBIS	Ocean Biogeographical Information System
OLI	Ocean and Land Imager
OTU	Operational Taxonomic Unit
PACE	Plankton, Aerosols, Cloud, ocean Ecosystem mission
PCA	Principle Component Analysis
PHILLS	Ocean Portable Hyperspectral Imager for Low-Light Spectroscopy
PPC	Post-Classification Comparison
PPK	Post-Processing Kinematic

PRISM	Portable Remote Imaging SpectroMeter
R_{abs}	Estimated Absolute Reflectance
RADAR	RAdio Detection And Ranging
RBSVC	Radial-Based Support Vector Machine
RGB	Red Green Blue
ROV	Remotely Operated Vehicle
RPAS	Remotely-Piloted Aerial System
RS	Remote Sensing
RSR	Relative Spectral Response
RTK	Real-Time Kinematic
RTM	Radiative Transfer Model
SAM	Spectral Angle Mapper
SAMSON	Spectroscopic Aerial Mapper with On-board Navigation
SAV	Submerged Aquatic Vegetation
SeaWiFS	Sea-viewing Wide Field-of-view Sensor
SfM-MVS	Structure from Motion-MultiView Stereo photogrammetry
SHOALS	Scanning Hydrographic Operational Airborne Lidar Survey
SIMPER	SIMilarity PERcentages
SNR	Signal-to-Noise Ratio
SPOT	Satellite Pour l'Observation de la Terre (Satellite for Earth Observation)
SVI	Spectral Vegetation Index
SWIR	Short-Wave Infra Red

SWOT	Surface Water and Ocean Topography
TID	Temporal Image Differencing
TM	Thematic Mapper
UAV	Unmanned Aerial Vehicle
uCASI	micro-Compact Airborne Spectrographic Imager
UV	Ultraviolet
VIS	Visible spectral region
VR	Virtual Reality
VTOL	Vertical Take-Off and Landing
WAVI	Water-Adjusted Vegetation Index
WISE	WaterSat Imaging Spectrometer Experiment

Author Contributions

The second and third chapters of this thesis are written in manuscript style; both have been published in peer-reviewed journals, in *Remote Sensing* and *Frontiers in Environmental Science*, respectively.

Gillian Rowan (GR) and Margaret Kalacska (MK) both contributed to the conceptualization of the two chapters. GR developed the methods and reviewed the literature included in chapter two as well as prepared the original draft. MK and GR reviewed and edited the manuscript.

GR and MK developed the methods of the third chapter. Raymond Soffer (RS) developed and applied the radiometric correction used on the imagery, and contributed a written explanation of the method for inclusion. Deep Inamdar (DI) implemented the DII transformation and created the georeferenced data product used in the research. GR undertook the analysis and wrote the original draft of the paper. J. Pablo Arroyo-Mora (JPAM) contributed a figure to the paper. JPAM and RS funded and acquired the imagery used in the study. GR, DI, JPAM and MK acquired the ground calibration data, GR acquired the underwater validation data. All authors reviewed and edited the manuscript.

All other content within this thesis was written by GR and reviewed by MK.

Acknowledgements

It took a lot to get me to this point, so I have many people to thank. Firstly, I am infinitely grateful to my supervisor, Prof. Margaret Kalacska. She took a chance on me, a student with no experience in or knowledge of remote sensing but a desire to learn, and changed my life. Since then, Margaret has taught me not only remote sensing, but also how to approach problems critically and creatively. She has dedicated countless hours to making me a better scientist and to preparing me for a research career. Her high expectations and consistent encouragement made me want to push myself to my full potential. Maybe most of all, Margaret showed her incredible dedication to her students in how many times she read and re-read my work, so that I could produce a thesis worth being proud of. Margaret, thank you so much for everything over these past three years.

I'd also like to thank Prof. Andrew Hendry, a member of my supervisory committee, for his support, guidance, and creativity in our discussions. I always left our meetings with new avenues to investigate and feelings of excitement about my work and where it might take me.

I would like to thank our collaborators at the NRC-FRL, specifically Dr. Pablo Arroyo-Mora and Raymond Soffer. Pablo brought expertise and enthusiasm to all our meetings, setting high standards while also making sure that we love what we do. Thank you, Pablo, for all the help, feedback, and advice you've given me. Ray, thank you for your incessant effort to make the data we use and the research we do as high quality as it can be, and for taking the time to teach me. My research wouldn't have been possible without all the hard work from both of you to get the field campaign off the ground. I genuinely can't thank you enough.

I need to thank Deep Inamdar, an absolute legend of a friend and labmate. Thank you, Deep, for the advice, support, jokes, pizza nights, and video calls. I wouldn't have made it without you. Thanks to Oliver Lucanus for collecting many of the photos I used in this work and for keeping field work fun. Thanks E-Skye, Patrick, and Kathryn for your help in the field, and your support throughout my degree. I really hit the jackpot in getting to know and work with you all in ARSL.

My gratitude goes out to the Natural Sciences and Engineering Research Council of Canada and the Canadian Airborne Biodiversity Observatory for supporting this research. I would also like to thank Mr. Roger Warren for his incredible generosity in supporting students

like me through the Rathlyn Fellowship in GIS. I am additionally grateful to the staff of the Long Sault Parkway provincial park, without whom field work and data collection would have been impossible.

Finally, the biggest thank you to my friends and family. To Lesley, Fanny, Dan, Patrick, Jennifer, Annalise, Victor, and Kelsey for making me happy on even the hardest days. Thanks to my parents for making me the curious, determined, stubborn person that I am today, and for giving me my love of the water that still drives me in all aspects of my life. Thank you for supporting me in all my adventures. To Zach, for challenging me when I need a push and believing in me when I don't. And to Nolan, for cheering me on so enthusiastically I started to think you were being sarcastic. You'll never know how much I appreciate having you here when things get tough (other times too, but you know what I mean). Whenever I think I'm ready to give up, you fine people pick me up, dust me off, and keep me going. I'm so grateful have you all in my life.

1. Introduction

1.1. Thesis Context

While applications of remote sensing in terrestrial environments have been thoroughly investigated and leveraged across academic fields and industries, substantially less attention has been paid to applying these technologies to the aquatic environment, especially so for freshwaters (Figure 1.1) [1,2]. This inequality can be attributed to the complexity introduced by the presence of an overlying water column, freshwater scientists' general inexperience with remotely sensed data, and the historically low interest in studying these systems relative to their terrestrial and marine counterparts. The combination of the vital ecosystem services provided by submerged aquatic vegetation (SAV) and its increasingly threatened status are however drawing more interest and investment into the management of freshwater ecosystems [3-6]. Remote sensing instruments, platforms, and data are meanwhile becoming more accessible to researchers through public access data sharing platforms and technological commercialization and miniaturization. Aquatic researchers and ecosystem managers are thus progressively adopting remote sensing techniques for data collection to improve the monitoring of these systems.

Remote sensing is however a highly technical field, incorporating aspects of physics, electrical engineering, computer science, and geography. Without a primer in each of these subjects, a newcomer to the field may not understand the data they are working with, or reading about in others' publications, leading to a high barrier of entry to the field. Furthermore, if such a researcher attempts to implement remote sensing tools in their work and find they do not provide the expected results, they may be inclined to disregard the discipline all together. Finally, while remote sensing experts will always be needed for technological innovations, researchers from other fields with user-level knowledge are generally the ones to implement remote sensing in new, creative, and exciting ways [7]. Making the theories and techniques used in remote sensing easily available in an accessible manner is therefore of utmost importance if the discipline is to be fully potentiated.

It must be noted that this disconnect between ecologists/biologists and remote sensing experts is not attributable to either one group or the other. While this thesis focuses on acquainting ecosystem researchers with remote sensing theories and techniques, analogous work is needed to inform remote sensing experts on ecological principles. Even the most rigorous and

technically advanced remote sensing application would be practically meaningless without understanding the system or processes being studied. Furthermore, considering that applying remote sensing often requires extensive ground truth data and/or expert judgement, poor knowledge of the research subject may result in biased or blatantly incorrect results. To reap the full rewards offered through remote sensing, increasing multi-disciplinary collaboration and knowledge exchange amongst researchers is thus essential.

Most remote sensing work in aquatic environments has focused on waters that are both shallow and clears, which are most commonly coastal, as these traits facilitate the retrieval of optical data (see Figure 1.1). Freshwaters, however, tend to have higher coloration and turbidity, both of which vary across small spatial and temporal scales [8]. They are thus more difficult to characterize and account for in optical remote sensing applications. Additionally, freshwaters tend to be managed and regulated at the national level, and so have not benefited from the same level of multinational collaboration that international (i.e., primarily coastal and marine) waters have (e.g. [9,10]). Due to this combination of factors, less work has implemented remote sensing in freshwaters than in coastal waters, leaving many foundational knowledge gaps regarding the type of questions remote sensing can be used to answer in freshwaters and the methodologies that are most effective. Before large investments of time and capital are made into applying remote sensing to freshwater habitats, there should be an investigation of if these ecosystems are amenable to mapping and monitoring via remote sensing, what information can be reasonably expected, and what type of remote sensing analyses may be well suited to these applications.

1.2. Research objectives

The high-level objectives of this thesis are to 1) create a resource for non-specialists who are considering applying remote sensing to SAV research (in both fresh and marine waters) and, 2) address some of the foundational knowledge gaps that exist in applying optical remote sensing to monitoring SAV in freshwater ecosystems.

Prior to this work, there has been no comprehensive resource available to entry-level remote sensing users in aquatic studies that addresses all considerations of a remote sensing workflow from project planning to data analysis. As aquatic remote sensing is more complex than terrestrial applications, articles discussing techniques and processes specific to the aquatic environment are also often written for more advanced users. Aquatic researchers unfamiliar with

the concepts and theory behind remote sensing were thereby left to assemble knowledge from sources primarily discussing terrestrial ecosystems or to decipher the highly technical aquatic remote sensing literature. This "missing piece" motivated the first objective (and first chapter) of this thesis.

While some work has been conducted in assessing the suitability of SAV to identification and mapping using optical remote sensing, the subjects considered have primarily been single, or a small set of, SAV species or types examined with a single kind of data. This limits how the results can be extrapolated to inform other applications. The second objective of this thesis was conceptualized to produce generalizable data to inform future work. The specific objectives were to 1) determine the spectral separability of a set of SAV species, 2) examine the consequences of sampling conditions and project parameters, and 3) compare how the theoretical maximum separability between SAV targets translates into in situ mapping success.

The original research in this thesis is based on data collected in the Long Sault Parkway Provincial Park, in southeastern Ontario, Canada, which is a part of the traditional territory of the Audenosaunee, Mohawk, Haudenosaunee, and Huron-Wendat Peoples. Access to the Park was granted by Park management. Airborne imagery was funded and collected by the National Research Council – Flight Research Laboratory.

1.3. Thesis structure

This thesis is divided into four chapters. This first chapter presents the context surrounding the development of this thesis, the research objectives, and the structure of the thesis. A published review article presenting all necessary considerations in implementing remote sensing for monitoring SAV is provided as the second chapter. The third chapter presents original research on determining the spectral separability of SAV and a practical application in the form of a manuscript to be submitted for publication. The fourth and last chapter summarizes the findings of the thesis and outlines directions of future research that could further the work of this thesis.

1.4. Figures

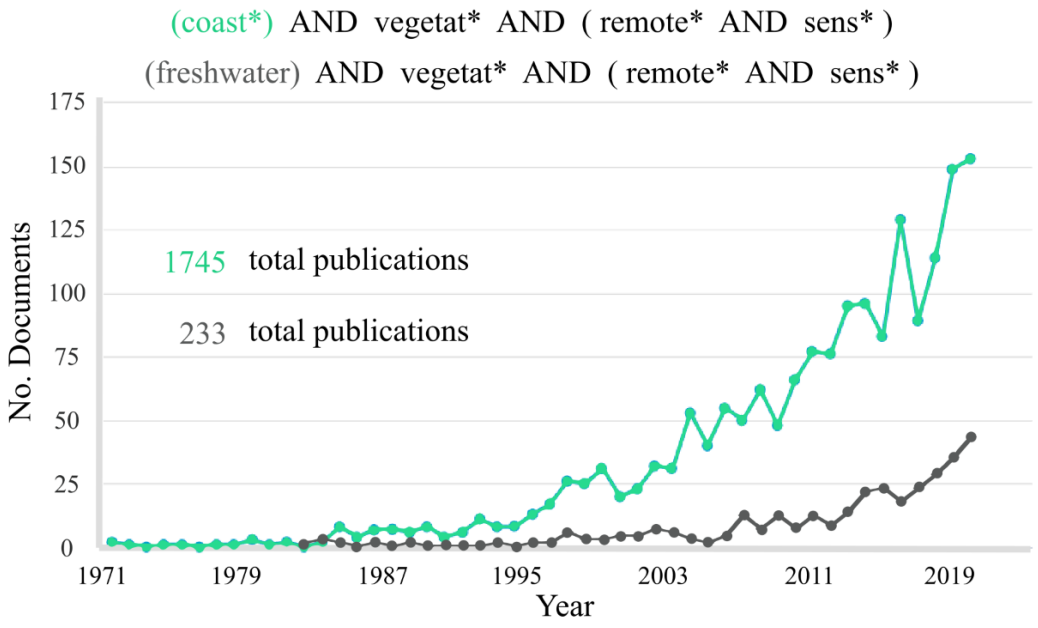

Figure 1.1 A comparison of the catalogue of previous research pertaining to aquatic remote sensing in general and freshwater remote sensing specifically. Records were retrieved from Scopus using the search terms noted, including publications from the 2020 calendar year and earlier. Figure originally presented in [1].

2. A Review of Remote Sensing of Submerged Aquatic Vegetation for Non-Specialists

Rowan, G.S.L.; Kalacska, M. A Review of Remote Sensing of Submerged Aquatic Vegetation for Non-Specialists. **Remote Sens. 2021**, **13**, 623. https://doi.org/10.3390/rs13040623

2.1. Context within the thesis

This chapter presents a comprehensive literature review describing the state of the art in remote sensing of SAV. The scope of the chapter was meant to include all that a non-specialist in remote sensing would need to consider when planning their own data collection campaigns, as well as to introduce concepts used in published works that may not be familiar to someone without formal training in remote sensing or geomatics. Simply, the goal of this chapter was to present everything a non-specialist would need to understand to reach a user-level of knowledge in aquatic remote sensing and to discuss the work that has been conducted thus far. The literature review highlighted the potential for remote sensing to be used in monitoring SAV but also the lasting need for further research and innovation in the technologies and methods available.

Per the thesis submission guidelines, the text of this chapter is exactly that of the published article.

2.2. Abstract

Submerged aquatic vegetation (SAV) is a critical component of aquatic ecosystems. It is however understudied and rapidly changing due to global climate change and anthropogenic disturbances. Remote sensing (RS) can provide the efficient, accurate and large-scale monitoring needed for proper SAV management and has been shown to produce accurate results when properly implemented. Our objective is to introduce RS to researchers in the field of aquatic ecology. Applying RS to underwater ecosystems is complicated by the water column as water, and dissolved or suspended particulate matter, interacts with the same energy that is reflected or emitted by the target. This is addressed using theoretical or empiric models to remove the water column effect, though no model is appropriate for all aquatic conditions. The suitability of various sensors and platforms to aquatic research is discussed in relation to both SAV as the subject and to project aims and resources. An overview of the required corrections, processing and analysis methods for passive optical imagery is presented and discussed. Previous applications of remote sensing to identify and detect SAV are briefly presented and notable

results and lessons are discussed. The success of previous work generally depended on the variability in, and suitability of, the available training data, the data's spatial and spectral resolutions, the quality of the water column corrections and the level to which the SAV was being investigated (i.e., community versus species.)

Keywords

remote sensing; submerged aquatic vegetation; hyperspectral imaging; species discrimination; extent mapping

2.3. Introduction

Submerged Aquatic Vegetation (SAV) is a key component of aquatic ecosystems as it creates habitat for fauna, regulates water flow, stabilizes sediments, and contributes to biogeochemical cycling [5,11-15]. SAV refers to all plants that obligately grow underwater, though they may have floating or emersed reproductive organs. Here, we refer to both freshwater and marine plants, as well as macroalgae (though not plants, they are spectrally similar). SAV growth has been shown to limit phytoplankton concentrations and reduce turbidity, improving water quality [16]. Seagrasses are especially notable for their role in capturing as much as 18% of all oceanic carbon and storing it as what is known as "blue carbon" [5]. SAV is therefore a vital ecosystem indicator of both biotic and abiotic processes and a significant carbon sink helping to mitigate climate change [4,5,17,18]. Despite the numerous physical, ecological and economic services SAV provides, it is in a state of global decline [5,14,19,20]. Several federal and international water quality frameworks, such as those in the European Union, the United States and Australia and New Zealand, include SAV extent or health as assessment indicators [17,21]. Other policies consider the conservation and protection of SAV as its own goal [4]. There is therefore a need for accurate, representative and timely knowledge of SAV extent and community composition [19]. The economic value of areas with SAV and the services they provide further increase the importance of proper monitoring [21,22].

Conventional SAV research involves in situ visual assessment of extent, species distribution or plant health using quadrats or transects [5,17,22]. This manual monitoring is costly, time consuming, can be dangerous (e.g., wildlife, parasites, traffic, etc.) and often has a high error rate [22-24]. These errors stem from observer misidentification, poor estimation and location accessibility biases that may not represent the full ecosystem heterogeneity [17,25]. Other

traditional methods include comprehensive sampling and the use of grabs or grappling hooks to collect specimens, which are destructive to the organisms being studied [26,27].

Remote sensing (RS) is increasingly being used as a tool in aquatic studies, often in conjunction with conventional techniques, to address some of the limitations of in situ methods [4,26,28,29]. RS is time efficient and increasingly affordable for researchers working at local, regional and global scales [28,30]. Accessibility issues are reduced as data are gathered at a distance, allowing the survey of fragile or dangerous sites while the operator remains at a single point of safety [31,32]. RS products can be used in quantitative analysis and can be compared over space and time when acquired and processed correctly [11,33]. The precise, quantitative data acquired by RS can also be used to monitor the slow, progressive changes in various ecosystems. As shown in Figure 2.1, the Landsat series of satellite-based sensors, for example, has an over 40-year historic catalogue of inter-comparable imagery [11]. Finally, RS may be the only realistic way to efficiently monitor remote and under-funded regions [4].

Innovations in aerospace technologies have allowed the evolution of manned aircraft-mounted (hereafter called “airborne”) sensors and satellite platforms; each increasing the spatial scale of the RS data available to users. Satellite RS has largely dominated the discipline, as can be seen through the substantial volume of work exploiting this data source and the large selection of active sensors shown in Figure 2.1 [34]. Technological advances, though, particularly in terms of unmanned aerial vehicles (UAV), are continuously providing new opportunities. The recent commercialization of UAVs and innovations leading to their increased affordability have made UAVs an appealing option for small-scale studies [32,35,36].

RS has been less extensively applied in aquatic studies than terrestrial ones. This can be attributed to the lack of early generation products specifically designed for use in water, high costs, as well as to the challenges of working in an aquatic environment and the SAV themselves [37-39]. The water column complicates analysis by attenuating the strength of benthic reflectance signals and introducing heterogeneity within a scene [40]; early applications of RS to macrophytes therefore relied solely on qualitative visual inspection of aerial photographs to extract SAV cover and distribution [22,40]. The small size of SAV features necessitates very high spatial resolution data which is expensive and may be unavailable to researchers working with a small budget [40]. The inconsistent application of calibration and correction methods to account for the atmospheric

and water column effects makes sharing and comparing imagery and data across studies difficult [17].

RS is rapidly evolving. As such, users unfamiliar with the discipline may not be aware of the applications, technological opportunities and products available to them. Additionally, no single RS method can be effectively employed across all conditions for all research questions [39,41]. It is therefore important to be informed of the options available, their strengths and limitations and how they may be combined. There is wide consensus in the RS community that while experts are vital for technological innovation and methods development, it is users from other fields applying RS methods to their own work that push RS forward through new and creative applications [7]. In short, there is a need to make RS more accessible to non-specialists. This paper is thus intended as a preliminary guide for those considering applying RS in aquatic botany, with a focus on optical approaches.

This review introduces and discusses the essential concepts in SAV RS to lay a foundational understanding of the discipline for non-specialists that are interested in applying RS in their work. It briefly presents the essential concepts in RS then examines specific considerations in applying RS to SAV. A selection of previous applications is presented to highlight some of the successes and challenges encountered in the field. While seagrasses and the research surrounding them are included in this text, the reader interested exclusively in seagrasses is additionally directed to [42].

While there is significant work being done on corals and some concepts may be translated from that field to the study of SAV, this paper does not directly discuss RS applications to corals and coral reefs. Similarly, mangroves, marshes, wetlands and riparian vegetation are not discussed here as the RS techniques applied to these habitats are vastly different from those applied to fully submerged targets.

This paper presents the following five aspects of RS application to SAV studies that any researcher should be aware of and consider: (1) a technical background on the use of RS in the aquatic medium; (2) a description of the types of sensors and data produced; (3) an overview of the relevant RS platforms and their operational levels; (4) an overview of how optical RS data is processed and analyzed; (5) examples of RS applications in SAV research.

2.4. Review Article Methodology

A literature review was conducted of English language peer-reviewed articles, theses, books and conference papers relating to the RS of SAV with no time constraints. The literature was found by keyword search using the logic ("Remote* sens*" OR "hyperspectral" OR "multispectral" AND "Aquatic vegeta*" OR "macrophyt*" OR "hydrophyt*") on Scopus. This returned 4139 references, of which the first four hundred most relevant English language entries were selected. Duplicates were removed and the remaining items were screened according to their abstracts (articles and conference papers) or introductions/summaries (theses and books). The bibliographies of selected references were also consulted to extract other relevant sources. A total of 305 references about SAV studies using RS (predominantly optical) were selected for review, though not all of those were included in this text. A small selection of other references has also been included in this work regarding general RS and data processing.

2.5. Technical Background

2.5.1. Key Concepts in RS for Aquatic Research

Earth observation RS measures the energy reflected or emitted by an object or surface, hereafter referred to as a target, to infer information about that target. The information obtained can be qualitative, such as presence/absence or cover classes, or quantitative, such as a reflectance profile or temperature. Data from RS is also positional, meaning that each piece of information obtained represents a discrete known location.

Spectroradiometry, and passive optical RS generally, provides information about the composition of targets based on how they reflect or emit energy. Active RS, on the other hand, measures the distance from the sensor to the target which can be used to determine the target's position and/or structure. It can, with some sensors, also record backscatter intensity providing some information about the condition or identity (e.g., RADAR). Considering aquatic research, active RS can be applied, for example, to measure and model habitat structure (e.g., [43]) or vegetation presence and absence (e.g., [41]). Table 2.1 presents a list of essential RS concepts that should be reviewed by anyone new to the field and may be helpful to those who are familiar with RS but are not experts.

In its simplest form, SAV extent mapping in optically clear waters may be done through visual inspection, so only imagery and user judgment are required. More involved research

objectives, such as species discrimination or health analysis, may also require reference spectra from the macrophytes of interest, validation data and specialized analytic tools and software. It is therefore important to define what information is needed from any RS project and which data inputs are required before beginning a data collection campaign.

2.5.2. Resolutions

The four types of resolution presented in Table 2.1 are discussed below as they relate to SAV monitoring. While pixel size may be resampled during post processing, spatial resolution depends on the sensor and imagery acquisition parameters and cannot be improved post-collection. Moderate to high spatial resolution is vital in SAV research because of the often-linear distribution of SAV along coastal and bathymetric contours and the patchiness of SAV growth [44,45]. Imagery acquired at a high spatial resolution can thus be used to identify far smaller features than from coarse images, as shown in Figure 2.2. Giardino et al. [44] found that pixels as small as 4 m may still be too large to be suitable for SAV studies in small lakes [44].

The strong similarity between SAV species' spectral profiles demands very high spectral resolution to allow discrimination. Additionally, not all sensors have spectral ranges suitable for SAV studies as water absorbs most energy in the infrared (IR) region and signals in the ultraviolet (UV) region are often unreliably weak, thus limiting SAV research to operating primarily in the VIS and marginally in the NIR regions [46].

High radiometric resolution is advantageous when analyzing surfaces with very similar reflectance values, such as SAV, as small differences in reflectance intensity are captured. For example, Landsat 5 acquires 8-bit data while Landsat 8 acquires 12-bit data, which results in 256 and 4096 possible values per wavelength per pixel respectively [47]; Landsat 8 may thus allow better discrimination between targets even though the two satellite sensors share very similar band configurations.

The temporal resolution of satellite imagery is determined by a satellite's revisit time. Landsat missions have a 16-day temporal resolution while the commercial PlanetScope satellite constellation achieves daily revisits [47,48]. The temporal resolutions of other platforms (e.g., UAV) are determined according to the research project planning [49]. For SAV monitoring, a short revisit time is often desired because of the rapid growth and maturation of aquatic

vegetation. Additionally, identification may be most successful when considering the effect of seasonality. In temperate climatic zones, spring measurements tend to be brightest because of exposed light sediments below still-developing leaves. Dense summer canopies with full cover cause the benthic reflectance to be exclusively from the plants. Fall measurements capture heterogeneous changes due to senescence [17]. A study using multitemporal data would therefore capture the highest amount of spectral variation for each species and may produce the best identification results [16,17,46]. A thorough discussion of the implications of the four types of resolution in freshwater SAV research is presented in [30].

2.5.3. Underwater Light Environment

The water column complicates optical RS and differentiates analysis of data from those acquired of terrestrial scenes. Water molecules scatter, reflect and absorb electromagnetic energy, adding complexity to the path of light travelling between the sun, the target and a sensor [50], as depicted in Figure 2.3. The water column decreasingly scatters light with increasing wavelength, resulting in very strongly scattered UV energy and negligible scattering of wavelengths longer than blue. While water absorbs some energy across the spectrum, it absorbs light most strongly for wavelengths greater than 680 nm. Together, this means that optical RS of aquatic environments is largely limited to the visible region (VIS) of the spectrum [50], though some information can often be garnered from the near infrared (NIR) region if the water column is very thin (less than ~ 1 m) [26]. Water's very strong absorption of radiation in the IR can facilitate the distinction between above and below water targets [51]. Increasing water depth increases scattering and absorption, thus reduces signal strength across all wavelengths though most quickly in the IR, as illustrated in Figure 2.4 [52].

Natural waters however also carry dissolved organic and inorganic materials and plankton that each reflect and absorb a portion of the light passing through the water column. Characterizing the underwater light environment is therefore complex as these substances change the reflectance properties of a water column and can vary greatly across small temporal and spatial scales [50]. For example, because the reflectance profiles of sediments suspended in the water column have been shown to depend on the size of those sediments, the reflectance profile of the water column will thus be altered by a disturbance that resuspends sediments and by the amount of time that passes since the disturbance to allow for re- sedimentation [53]. Figure 2.5

presents the absorption profiles of major water column constituents in marine environments. The absorption profiles of natural waters are thus determined by combining the absorbances of each of these materials (and those of any other materials present in the waters), adjusted for the relative amounts of each component. The relationship between particulate and dissolved matter in the water column and their contributions to a spectral signal are complex, being both depth and wavelength dependent [50,51,54]. It is therefore important to characterize the effect of the water column if the absolute target reflectance is to be calculated; methods to do so are discussed Section 5. A thorough examination of the spectral effects of water column constituents is presented in [44].

When waves curve the water's surface, light is concentrated by convex wave crests and dispersed by concave wave troughs, resulting in the familiar web pattern of bright lines that one sees in a swimming pool [50]. Concentrating and dispersing light does not alter the wavelengths of light reflected by a target but does create disparities in the intensity of light available to be reflected over space and time [50]. Waves can therefore produce variation in the magnitude of the spectral reflectance profile of a material without affecting the shape of a target's profile. A wave crest or trough does however change the thickness of the water column and may thereby alter the shape of the water-leaving signal, particularly in very shallow waters where wave height is a significant portion of the total water column thickness. Furthermore, the differences in refraction caused by wave crests and troughs produces unequal magnification of benthic features which can distort the perceived shape of underwater targets [55].

The measured spectrum of a target therefore depends on the thickness of the water column, its constituents and its behavior. Areas that are sufficiently clear and shallow to see the benthos are called "optically shallow waters" and it is to these areas that optical RS can be applied; waters that are either too deep or turbid to do so are called "optically deep" and are more suited to study from acoustic RS. Clear coastal waters under ideal conditions may be optically shallow up to 40 m [5] while inland freshwaters are often optically deep at just a few meters [50,56].

2.5.4. Spectral Properties of SAV

When radiation reaches a leaf, it is either absorbed, transmitted or scattered by the leaf components (primarily the pigments and cellular structure), with light scattered back away from

the leaf appearing to be reflected [57]. Green vegetation, including many SAV species, has an easily identifiable spectral profile because of the consistent absorbance properties of its pigments. Chlorophylls, lutein and a-carotene all absorb blue light (around 445 nm) very strongly and do not absorb green light (around 550 nm) much at all. Chlorophyll-a (Chl-a) and -b also absorb red light (around 645 nm) [17,57]. This produces the characteristic "green peak" in the VIS. Accessory pigments, like carotenes and xanthophylls, create additional absorption features in the VIS that can be used for distinguishing groups or species [57]. Increasing the concentration of any pigment will reduce reflectance across the spectrum but will do so inconsistently to reinforce and widen any associated spectral features. High concentrations of accessory pigments can therefore attenuate the overall reflectance magnitude and the relative prominence of features indicative of the major pigments [58]. Vegetation also displays a distinct and drastic increase in energy reflection in the NIR called the "red edge" and the "IR plateau" due to the multiple scattering of IR energy in leaf tissues [57]. The red edge and IR plateau are however heavily affected by water's absorption in that region, making these features more difficult to analyze underwater than in terrestrial situations [59]. As shown in Figure 2.6a), the spectra of two SAV species differ in shape, particularly in the VIS where reflectance is determined by pigment concentrations. It is additionally shown that the magnitude of reflectance within a species is significantly reduced when the plant is placed under even a thin water column.

The measured reflectance of SAV varies across seasons, depths, light intensities and habitat types. Epibionts and sediments on the plants can also confound reflectance signals registered in situ as shown in Figure 2.6b). Therefore, if a spectral library is to be used in image analysis across many scenes or conditions, sufficient variation should be included in the library to account for the changes in each of these factors [58].

2.5.5. Supplemental Datasets in Aquatic RS

RS has been applied to determine SAV distribution, cover classes, canopy density, health and species. Measurements from aquatic RS have also been used as inputs for modelling fish habitat and distributions [60,61]. However, assessing the biophysical properties of SAV through RS has yet to be extensively explored and those studies that did, examined superficial characteristics such as biomass or plant height [17,62-64]. More advanced applications of RS have

likely not yet become popular because of the substantial amount of supplementary data required for accurate results.

The three primary types of supplemental data involved in SAV RS are vegetation ground-truth data, depth and bathymetry and water column optical properties. Vegetation ground truth data could include spectral profiles, biophysical metrics, presence and absence data and so forth depending on the study goals. Collecting these data often uses traditional SAV sampling methods (i.e., quadrats and transect surveying), in situ spectral measurements or geolocated observations from ships. A thorough example of vegetation ground truth sampling is presented in [65]. Depth and bathymetry information is sometimes readily available as many organizations have created bathymetric maps of major water bodies for navigation purposes. Using these pre-existing data sets as inputs into water column corrections (discussed below) may improve the accuracy of the correction and thereby facilitate further analysis. It must however be noted that plant depth and bathymetric depth are not equivalent; preexisting bathymetric depth datasets are more useful when considering carpeting or short growing SAV than when investigating tall plants that reach far above the benthos. Otherwise depth in optically clear environments can be modeled from high spatial resolution satellite (or airborne) imagery [66,67]. Quantifying the effect of the water column radiation is essential if a study is to examine the reflectance of an underwater target as opposed to the reflectance leaving the surface of the water over a target. While there are models that estimate the effect of the water column without directly measuring it [67,68], researchers may achieve better results by including directly measured parameters. This can include quantifying the concentration of dissolved substances through spectrophotometry and measuring the light penetration at various depths in situ to calculate attenuation [69,70]. Obtaining these supplementary datasets can be financially and time demanding while their utility will depend on conditions at the specific study location. The cost of supplementary data must therefore be weighed against the potential improvements in results and accuracy during study planning.

2.6. Sensors

Sensors can be passive or active, acoustic or optical, depending on the source and type of measured energy. Sensors also vary in how many discrete bands of energy wavelengths they record. Table 2.2 presents the types of sensors that are commonly used in SAV RS according to these criteria, as well as examples of each type and sources with previous applications.

2.6.1. Available Sensors

As described in Table 2.2, The Light Detection And Ranging (LiDAR) sensors used in aquatic studies are termed "bathymetric LiDAR" because they use green light as opposed to the conventional IR which is heavily affected by water column absorption [71]. The Scanning Hydrographic Operational Airborne Lidar Survey (SHOALS) system, can measure bathymetric features up to 40 m in depth. SHOALS' typical 4-m spatial resolution may however be too coarse to resolve small SAV patches and provides only structural and positional data [72]. Radar, while useful for detecting water features, sea ice, surface characteristics and the canopy structure of emergent vegetation (e.g., [73-75]), is not applicable in SAV studies because the microwave energy used is nearly entirely reflected at the water's surface [18,71,76].

Acoustic sensors are advantageous in aquatic settings because of the high transmission of sound waves through water. They perform well in turbid or optically deep waters where optical methods fail [41]. As plant canopies reflect only a part of the acoustic energy with the remainder passing through to the substrate, acoustic scanners can receive multiple reflection signals that detail multiple layers of vegetation and the material below them, as shown in Figure 2.7. A single beam echosounder produces transects of data (Figure 2.7), while a multibeam echosounder can create acoustic images with two dimensions of pixels [41]. Side scanners also produce acoustic images and are especially effective in macrophyte studies as their horizontal plane intersects vertically growing plants [41,71,77].

The exclusively positional data provided by acoustic sensors cannot provide information about the species, health or maturity of vegetation; the applications of such sensors are thus limited to structural information. The accuracy of hydroacoustic methods has also been questioned by some studies. It has been found that hydroacoustic methods produce higher SAV height and percent cover measurements than those from divers or imagery. Hydroacoustic methods may therefore not capture modest changes in SAV conditions and are not suited to direct comparison with data gathered through other methods [77,78]. Still, ongoing innovations in hydroacoustic RS—such as the Dual-frequency Identification Sonar, which produces acoustic video footage—are expected to make acoustic RS more appealing and accessible for work in turbid waters [41].

In addition to the criteria in Table 2.2, passive optical sensors are additionally grouped by how they record information. Non-imaging, point measurement spectrometers collect a single

spectrum at a time and produce signatures such as those shown in Figure 2.6. Most imaging sensors are either whiskbroom or pushbroom, meaning they collect one pixel or one row of pixels at a time, respectively [79]. There are also full frame multi- and hyperspectral options, for example the Ultris 20 from Cubert acquires spectra for a 400 × 400 pixel array at once across 100 bands [80].

Panchromatic and RGB film photographs provide historical records of macrophyte conditions as far back as the late 1920s in some areas [30,81,82]. These aerial images can be used as raw inputs for maps or supporting information for interpreting satellite imagery [71]. Modern digital RGB cameras can additionally be used to collect data for simple analyses; Flynn et al. used an RGB Go Pro Hero 3+ mounted on a consumer grade UAV to map green *Cladophora glomerata* cover against a yellowish-brown background with 92% overall accuracy in a shallow river [83].

Wavelengths covered by bands on multispectral sensors are selected to avoid regions with near complete attenuation from the atmosphere and placed to detect specific features such as the green peak, red edge and IR plateau [84]. Thermal bands may be chosen to record sea-surface temperatures [85]. There is a plethora of multispectral sensors on orbiting satellites, each strategically designed with specific spectral, spatial and radiometric characteristics dependent on their intended uses [44,86].

Some imagers, such as the hyperspectral Compact Airborne Spectrographic Imager (CASI), allow the user to define the band placement and width according to features of interest [58,87]. This flexibility makes them especially well-suited to macrophyte studies where band placement in the VIS wavelengths can be prioritized. The information contained within the additional bands of hyperspectral imagery (HSI) allows many more variables to be calculated than from multispectral imagery (MSI) of the same scene and improves the accuracy of atmospheric and water column corrections [44]. Though MSI contains less spectral information than HSI, it is well suited to aquatic applications such as ocean color investigations or detecting SAV cover and is less expensive than HSI of the same spatial resolution [23].

Handheld and portable spectroradiometers that collect point-measurements are often used for ground-truthing or sample measurement under laboratory conditions. Because these measurements are taken close to (or in contact with) the targets, they capture the reflectance of the

targets with very little (or no) contribution from other sources. Classifications on these pure spectra are therefore far more accurate than on image pixels that may contain more than one material, blurring and atmospheric effects. The RAMSES hyperspectral radiometer (TriOS, Rastede, DE, USA) for example, is designed for aquatic applications such being mounted on a boat or being submerged into the water column [88]. Other common examples of portable, hand-held hyperspectral sensors include the ASD Fieldspec series (Malvern Panalytical, Boulder, CO, USA) [89], the SVC HR-640i (Spectral Vista Corporation, Poughkeepsie, NY, USA) [90], the Flame series (Ocean Insight, Orlando, FL, USA) [91] and Spectral Evolutions' SR series (Spectral Evolution, Haverhill, MA, USA) [92], each having different features like underwater housings or fiber optic measurement tips.

2.6.2. Advancing Technologies

Water's absorption of electromagnetic radiation diminishes the strength of signals from aquatic targets; a sensor with a high signal-to-noise ratio (SNR) thus allows the low magnitude target signal to be discriminated from atmospheric and sensor noise [44]. Muller-Karger et al. [93] suggest an SNR of 800 or more to be ideal for sensors designated for coastal RS, though few current sensors comply with such a high SNR requirement. Macrophytes often grow individually or in small patches and, as with terrestrial vegetation, may have very similar spectral profiles across different species. SAV monitoring therefore necessitates high spatial and spectral resolution data that can resolve subtle features. As the near UV and blue regions are not strongly absorbed by water, these regions could provide essential information about aquatic targets. Furthermore, when successfully captured, blue wavelengths are suggested to be useful for discriminating between species [58]. Short wavelengths are, however, highly susceptible to scattering the water column and atmospheric aerosols, so the blue region signal is often especially weak. A sensor well suited to aquatic research would therefore have a high SNR across its spectral range; high radiometric, spatial and spectral resolutions; and would be sensitive to the near UV and blue regions. Such sensors are being actively designed and developed.

The Portable Remote Imaging Spectrometer (PRISM) airborne sensor, for example, was designed to address aquatic research needs. Its spectral range is from 350 nm to 1053.5 nm with bands 2.83 nm wide. The 14-bit radiometric resolution allows for 16,384 discrete radiance values

and the SNR of 500 in the blue region is an improvement over most other sensors. Depending on the flight parameters of its deployment, pixels of less than 1 m can be achieved [94].

The Canadian Space Agency (CSA) has planned the WaterSat microsatellite mission to improve its RS capabilities in inland waters (particularly rivers and lakes below 10 km in width) and in near-shore coastal areas. The proposed specifications for the WaterSat optical imager are aligned with the above outlined aquatic needs: 100 m spatial resolution over a 300 km swath width and 10 nm spectral resolution from 400 nm to 1000 nm [95]. Clearly the proposed 100 m spatial resolution would not be well suited to small SAV patches, rather it would be appropriate for assessing SAV communities at large. A prototype for this optical sensor, the Water Imaging Spectrometer Experiment (WISE), was developed in 2018 [96] and is currently being tested. The Pre-Aerosol, Clouds and ocean Ecosystems (PACE) sensor, planned to be launched into orbit in 2022/2023, will provide ocean color information and data relating to phytoplankton and atmospheric conditions at a 1 km spatial resolution [95,97]. If the WaterSat and WISE prove successful, a similar sensor called the Coastal Ocean Color Imager will be added to the PACE mission, thus providing large spatial scale multispectral, and finer spatial scale hyperspectral, imagery. NASA is additionally developing two new active sensors for aquatic observation purposes: the MiDAR, designed to help correct for the distorting effects of waves, and the Surface Water & Ocean Topography (SWOT) sensor which will allow improved measurements of in-land and marine surface height to better understand hydrological dynamics [55,98]. The airborne prototype, AirSWOT is currently being tested [99].

2.7. Platforms

RS systems include all components required to collect, store, process and analyze RS data. On a satellite platform, the user interacts solely with the imagery. For user operated platforms (e.g., manned aircraft, UAV, ROV) however, not only is the choice of sensor important but also the platform upon which it is mounted and any additional hardware. While the operational levels and set-ups of platforms vary, all systems that provide spatially explicit information incorporate a device for doing so. This is especially important for aquatic research as landmarks that may later help situate imagery are rare.

Most RS systems include one or both of a Global Navigation Satellite System (GNSS) receiver and an inertial measurement unit (IMU). A GNSS receiver records its positional

coordinates at a set interval, by calculating its position relative to satellites transmitting their known locations. The best results are produced when many well-spaced satellite signals are intercepted [100]. Time-stamped positional information collected in this way allows contemporaneous measurements to be registered with the associated coordinates. While a conventional GNSS receiver can achieve geolocational accuracy on the scale of a few meters [101], realizing better geographic accuracy necessitates more involved positioning systems and corrections. Real-time kinematics (RTK) and post-processing kinematics (PPK) can improve this accuracy by incorporating correction transmissions from base stations (either temporary, local base stations at the field site or permanent, commercial base stations elsewhere) with known locations [102]. Platforms using RTK receive the base station corrections and apply them concurrently to data collection while PPK incorporates the corrections after data collection is complete in post-processing [103]. The three geolocation methods are illustrated in Figure 2.8. By measuring how many signal cycles occurred between the base station and receiver, the distance between the two is known with accuracy equal to the wavelength of the signal [114]. While GNSS uses only the coded signal, RTK and PPK use both the coded and carrier signal types and can thus obtain positional accuracy on the centimeter scale [104]. As RTK and PPK are dependent on base station corrections, their accuracy is limited by the accuracy of the base station position [103]. Any error or uncertainty in the base station position will translate into equal error and uncertainty in the position of the receiver. IMUs collect information on the acceleration and attitude of the platform. Considering the acceleration and rotational changes during the data acquisition allows the user to calculate the position and look direction of the sensor throughout acquisition [100]. Attitude information provided by the IMU can be used to trace the direction of the sensor lens and indicates how the area imaged differs from one instance to the next, as illustrated in Figure 2.9. If the positional accuracy of the image registration through such methods is inadequate or the equipment is unavailable, placing or finding easily visible ground control points (GCPs) with precisely known locations within the image and registering the image to those points can also be effective [21]. In aquatic settings however, placing GCPs may be difficult due to accessibility or currents. As very high accuracy GPS receivers do not function underwater, using GCPs to position an image with high accuracy is limited to shallow and intertidal sites [105].

RS platforms for aquatic applications can be situated within the water column, at or near the surface, in the near atmosphere or in orbit. As such, they are inconsistently influenced by atmospheric and water column effects and produce imagery of vastly different quality, spatial resolution and spectral resolution. The platforms employed in aquatic RS can be categorized as on-water or off-water platforms and as moving or fixed [41]. Sensors mounted on on-water platforms are negligibly—if at all—affected by the atmosphere and so do not require atmospheric correction. Fixed platforms collect information about a single point over a given period. Moving platforms collect a snapshot of data across multiple locations [106]. On-water moving platforms comprise submerged vehicles, hand-held equipment and vessels; on-water fixed platforms include buoy- and pier-mounted systems. Unmanned aerial vehicles (UAVs), aircraft and satellites are all off-water moving platforms.

2.7.1. ROVs and AUVs

Remotely Operated Vehicles (ROVs) and Autonomous Underwater Vehicles (AUVs) are used to overcome accessibility issues in aquatic environments. ROVs and AUVs are motorized instruments that can collect data underwater replacing a person in snorkel, scuba or submersible equipment. ROVs are tethered to the point of operation and receive power and instruction from this tether. The tether also allows data to be transmitted in real time to the operator. ROVs are therefore valuable tools in complex sites, where water conditions are unpredictable or unideal and for bottom sampling [107]. AUVs are entirely unattached, with their own navigation, power and data storage equipment onboard. This allows their missions to be pre-programmed and leaves the user free to address other tasks during the AUVs' operation, though this also means that an AUV may be lost during a mission [107-109].

ROVs and AUVs range greatly in ability and price point, both of which should be considered when choosing a vehicle. While small, relatively fragile ROVs may be suitable for conducting research in shallow waters with weak flow regimes such as lakes, ponds and protected inlets, much larger and sturdier instruments are required to collect data near deep-sea hydrothermal vents [107]. These more advanced units are more expensive to acquire and operate and are thus often developed and managed by governmental agencies or large research facilities [107,110].

While open sourced or low-cost ROVs and AUVs may not be suited to specialized sampling or extreme environments, they do offer the advantage of customization and convenience. Davie et al. [52] showed that simple additions of hardware to the Starbug AUV facilitated and improved depth correction during post-processing. These aquatic vehicles can otherwise be easily upgraded by changing or adding to their stock sensors [52]. Roelfsema et al. found that using an AUV to collect ground-truth data was more repeatable than snorkeling surveys as an AUV strictly follows a preprogrammed route whereas a snorkeler relies on initial headings or visual cues and may drift. The use of an AUV was also shown to extends the depths to which they could collect ground-truth data [111].

There are certain risks associated with the use of ROVs and AUVs. In the case of imperfect waterproofing or sealing, data on the device or the device itself may be compromised [111]. In benthic surveys, the vehicle may become entangled in debris or vegetation which could lead to mission complications or loss of the vehicle. Malfunctions due to temperature or pressure extremes can additionally cause vehicular damage or loss [109]. Apart from potential risks to the research operation, ROV and AUV use can be damaging to the environments in which they are employed, particularly through the spread of invasive species [112].

2.7.2. Hand-Held, Vessels and Fixed Platforms

Sensors mounted on vessels, piers or buoys and hand-held devices can be used to collect data above or below the water's surface. For spectral data collection, however, it is suggested that only in collecting measurements both above and below the surface can a researcher account for all factors contributing to the measured signal [17]. In the case of a sensor being mounted on a large platform—such as a boat, pier or researcher—the influence of the platform should be considered in planning the collection geometry and procedure. A boat or pier may shadow the target if the sensor is poorly placed. A researcher may stir up sediments or disrupt epibionts—or the SAV itself—during collection [17,58]. If the field observations are taken to be used as ground truth or validation data for airborne or satellite imagery, scale discrepancies must also be accounted for through sampling designed to be representative of the whole scene being validated. Point source spectra acquired by spectroradiometers should not be used directly from the instrument. Spectra should be processed to absolute reflectance to allow for valid comparisons of

spectra of the same target over time or acquired at different locations, by different instruments or reference targets [113].

2.7.3. Unmanned Aerial Vehicles

UAVs range dramatically in size and flight capabilities [36,114]; those referred to here are ones that are available to civilian researchers and are thus relatively small (<25 kg) and operate at low-altitudes. Most regulatory bodies limit this kind of drone operation to the pilot's visual line of sight [103]. The units are lightweight and can be deployed by a small team of users with limited available space. UAVs range in complexity from balloons to gliders to motorized vehicles [33]. There are two groups of motorized UAVs: fixed-wing and rotary-wing. Rotary-wing UAVs ascend vertically (referred to as Vertical Takeoff and Landing—VTOL) and are thus not constrained by needing a runway [114]. Most fixed-wing UAVs operate similarly to traditional aircraft in that they require an open area to take off and land in but some modern fixed wing systems also incorporate VTOL capabilities.

The expansion of UAV employment in RS provides many advantages. UAV-mounted sensors are preferred in situations when very high spatial resolution optical data over a small physical area is needed (e.g., Figure 2.2a) [26,36]. These systems can be deployed quickly with varying sensor configurations, thus making them well suited to environmental monitoring missions [32,87]. Their proximity to the target lessens the atmospheric contribution in the registered signal. The expansion of UAVs is pushing sensor development towards lightweight, financially accessible sensors of similar quality to those traditionally flown on aircraft or satellites [32].

The application of UAVs in RS is constrained by their limited payload tolerance, preventing most heavy multi- and hyper- spectral sensors from being flown on them. This limitation is however being addressed through innovations in developing smaller sensors and stronger UAVs (e.g., [115-118]). As small UAVs tend to be battery powered, their flight durations are further limited to flying only so long as the charge lasts. Rotary-winged UAVs are especially affected as vertical ascent and hovering are energy-intensive operations [114]. Joyce et al. [105] provide an extensive look into the logistical, practical and regulatory considerations of implementing UAVs in aquatic research.

2.7.4. Manned Aircraft

Airborne imagery is especially useful when high spatial resolution information is required over a larger spatial extent than can be achieved with a UAV or when the desired sensor cannot be accommodated by a UAV due to size or weight restrictions. It provides a link between very high-resolution ground or UAV data and satellite data and can aid in the interpretation of the latter [119]. Figure 2.10 presents an example of the imagery obtained from one flight line collected using a CASI-1500 mounted in a twin otter aircraft. The 1 m pixels are sufficiently small to allow underwater features and SAV patches to be resolved while the spatial coverage of the imagery is far larger than what would be possible using a UAV.

Airborne campaigns can be planned to acquire imagery suited to various purposes as the image properties are largely dependent on the flight parameters. The altitude and flight speed determine the across-track and along-track pixel dimensions respectively [120,121]. The altitude will also affect the swath width imaged during the mission, with lower flights covering smaller geographic locations for the same sensor configuration [122]. The stability of the aircraft during flight will contribute to how well positional and attitude distortions can be corrected. Note the distortions and gaps in the SE corner of Figure 2.10. These are caused by unintentional changes in aircraft attitude and the intentional turning of the aircraft at the start of the flight line (the aircraft travelled from south to north). There are visible attitude adjustments, seen as the very curvy portion that resulted from aircraft roll, after the turn as the aircraft stabilizes along the flight line, shown by the straighter northward segment. An experienced pilot is thus essential for a successful mission.

Airborne imagery is expensive to procure either directly or from a data provider, which may be financially restrictive [32]. It is therefore sometimes useful to use less costly products such as satellite imagery to identify priority areas to be analyzed with airborne imagery instead of procuring airborne imagery for an entire region [71].

2.7.5. Satellite

Satellite platforms and the sensors they carry tend to be referred to collectively, a convention that is followed in this text. Data collected from orbiting platforms generally have near-global coverage and can have temporal resolutions of less than a day (e.g., AVHRR,

SkySat), though most satellites or constellations have revisit times of a day up to two weeks. Open access satellite data products, such as those provided by the United States Geological Survey from the Landsat missions and those provided through the Copernicus program of the European Space Agency are, however, limited in their spatial, spectral and temporal resolutions. Moderate (e.g., 10–30 m) (Figure 2.2e,f) and low spatial resolution satellite products (e.g., 500 m–1 km) are often too coarse to capture the natural variation in aquatic vegetation distribution that is of interest to researchers [71,123]. For example, patches must have a diameter of 85 m to be reliably identified by the 30 m moderate resolution products from Landsat (Figure 2.2f) and SPOT satellites [124]. Large pixels also increase the chance of multiple materials or species contributing to the single signature registered for that pixel. Satellites thus have limited applicability in identifying SAV to the species level but have often been used to map broad SAV community extent [18]. Newer satellite systems are addressing this spatial limitation; the commercial multispectral satellite products from Maxar's WorldView series and Planet's SkySat, for example, can achieve multispectral spatial resolutions of 1.24 m and 50 cm, respectively [125,126]. The small number of spectral bands on multispectral satellites further restricts the information contained within each pixel.

Figure 2.11 presents a non-exhaustive list of sensors, organized by operating platform level, that have been used in aquatic RS, including many currently operating satellite sensors or constellations. The applications of each sensor and the accuracy achieved is shown. As seen in Figure 2.11, the open-access products appropriate to and available for, use in SAV research are limited to moderate spatial resolution satellite imagers such as Sentinel-2 (10–60 m) [127], Hyperion (30 m) [127] and Landsat (30 m) [47]. These are only useful if studying large features such as extensive seagrass meadows. Commercial systems like WorldView-3 have very high spatial (0.31 m panchromatic and 1.24 m multispectral) [126] and moderately high spectral resolutions (29 bands through the VIS and IR regions) [126] and can be used to accurately answer a wider range of SAV research questions. However, they are commercial products and their acquisition can be financially unrealistic [49]. Furthermore, imagery that is considered of sufficient quality to vendors may not be well suited to certain research applications or locations due to cloud cover, positional accuracy, glint, and so forth [16,21].

2.8. Corrections and Analysis

2.8.1. Correction of Passive Optical RS Imagery

While photographs and RGB imagery can sometimes be visually interpreted as-is, imagery being used in quantitative analysis or to compare between different dates or locations, must first undergo a range of corrections. The three necessary for RS optical imagery are radiometric correction, atmospheric compensation and geometric correction. Water column and air-water interface corrections are additionally commonly applied to imagery of aquatic environments.

Sensors record reflected radiance from the surface (and in-scattered from nearby objects) in the form of digital numbers (DN), with the range of possible DN values corresponding to the radiometric resolution. Radiometric correction converts the raw DN data to radiance, which is the amount of energy reaching the sensor, given in Spectral Radiance Units (1 SRU = 1 µWcm-1 sr-1 nm-1) [128]. This correction accounts for the sensor-specific detection and sensitivity variations and is often done using calibration files provided by the sensor manufacturer or another calibration provider [129]. Satellite imagery is provided to the user having already undergone radiometric correction (although a scaling factor or simple function may need to be applied to the data as delivered). Digital RGB (or black and white) photographs do not require this correction because the spectral response of the cameras rarely has been characterized in such a way as to allow for this type of processing.

Next, for imaging sensors, the scattering and absorption effects of the gases and aerosols in the atmosphere must be compensated for to isolate the target's signal. The magnitude of atmospheric contribution to a signal is directly related to the thickness of the atmosphere between the target and the sensor and the composition of the atmosphere [130-132]. While spectral signatures collected through contact measurements are not affected by the atmosphere, for spaceborne sensors, the atmospheric contribution can be the predominant contributor to the signal received in certain wavelengths (e.g., absorption of the signal at 1.4 µm and 1.9 µm by atmospheric water vapor) and a less significant contributor in others. The scattering and attenuation by the atmospheric constituents are wavelength dependent. While always required for quantitative analysis of MSI and HSI, atmospheric compensation is especially important when comparing scenes from different regions or collection dates as the effect of the atmosphere is inconsistent in space and time [133]. Atmospheric compensation can be accomplished using a scene-specific calibration methods such as the empirical line method (ELM) [134] or through radiative transfer

models (RTMs) (see Chapter 6 of Manolakis et al. [135] for a comprehensive description). In the ELM, materials such as calibration panels, calibration tarpaulins, concrete, bright sand or deep water are often used as calibration pixels. The reflectance spectra of both bright and dark calibration pixels, ideally characterized on the ground as close in time to the imagery collection as possible, are used to define the relationship between the at-sensor radiance and the target's actual reflectance [23,128,136]. The ELM is considered to be reliable, including for aquatic scenes and is most accurate when the conditions are constant between the ground and sensor measurement collections [129]. Such calibration is only effective if appropriate and well-characterized materials are present in the scene; deep-water pixels may not be suitable calibration pixels when the target is also underwater or when there are effects such as glare contaminating the pixels [18].

RTMs use parameters such as sensor altitude, ground elevation, aerosol optical depth and atmospheric composition to model the interaction of radiation through the atmosphere and estimate what portion of the recorded radiation was reflected by the target versus what portion originated in the atmosphere [18]. A variety of RTMs are available for atmospheric correction—such as MODTRAN [137], LibRadTran [138] and 6 SV [139]—each with its own strengths and limitations. Such RTMs are often applied with specialized software tools or dedicated user interfaces [133].

Imagery is geometrically corrected to assign coordinates to every pixel in the image and remove image distortions. This is done by accounting for changes in sensor altitude or attitude, differences in terrain elevation and sensor optics [140]. Systems equipped with both a GNSS and IMU produce the most geographically accurate and precise imagery. By combining the inputs of where the sensor is, how it is directed and the scene elevation, a ray can be traced onto the ground to the location being imaged in each pixel [129].

2.8.2. Corrections Specific to Aquatic Applications

Compared to terrestrial RS, aquatic applications have the additional processing requirements of accounting for the effect of the water column [71]. In shallow waters, the reflectance signal is most dependent on the vegetation density and the bottom reflectance. Measurements in very shallow water may also be heavily influenced by internal reflection if they are taken at a large angle from nadir [141]. As depth increases, the water column increasingly

contributes to the measured profile. This can result in sparse crown cover in deep waters spectrally resembling dense canopies in shallower areas [22,23]. Bathymetric data is therefore helpful as an additional variable in performing a water column correction. Even the simplest method of accounting for depth, masking out deep-water pixels, has been shown to improve the accuracy of classifications [22,71,142,143]. Specialized algorithms can also correct for the effect of the water column as a function of depth. Consider, for example, a definition of aquatic radiance as follows (Equation 1)

$$L_i = L_{si} + d_i R_i^{-Kifz}, \quad (1)$$

where L_i is the sensor recorded radiance in wavelength i, L_{si} is the radiance of deep water pixels, d_i is a constant representing the total irradiance just below the surface of the water, R_i is the bottom leaving reflectance, K_i is the effective attenuation coefficient of the water, f is a geometric factor to account for pathlength (nadir measurements would use a factor of 2) and z is the depth.

Operating under the assumption that water quality is consistent across an image, Lyzenga [141] created an RTM for water column correction based on Equation (1) that can account for different water conditions and bottom types and is solvable to estimate water depth (z) or bottom composition [141,144]. Modifications to Lyzenga's RTM like those by Sagawa et al. [145] and Tassan [146] have been designed to apply the RTM to specific research conditions and goals. Lyzenga based water column corrections are not however appropriate for research questions in which the absolute spectral reflectance values are needed [143].

In cases where absolute reflectance values are required, such as in studies comparing sensor values to in situ measurements, empirical or empirically based methods can be used. Purkis and Pasterkamp [143] describe one such model, adapted from [147], used to calculate target reflectance, R_i, as (Equation (2))

$$R_i = \frac{\frac{1}{0.54}R_{Ai} - (1-e^{-2Kiz})\,R_{si}}{e^{-2Kiz}}, \quad (2)$$

where R_{Ai} is the apparent reflectance measured just above the water's surface (obtained through either in situ measurements or by atmospherically correcting imagery) and R_{si} is the reflectance of optically deep water. This model accounts for the effects of the atmosphere,

surface refraction and depth while maintaining full spectral information. Purkis and Pasterkamp [143] found classification accuracies using this model to be sensitive to the depth used: roughly modelling the depth into five intervals and applying the actual target depths produced classification accuracies of 53% and 73%, respectively. The effectiveness of water column correction procedures may therefore be dependent on the quality of supplemental data available.

Water column correction algorithms can also be developed for a specific situation. To do so, Cho and Lu [148] measured the reflectance of white (100% reflectance) and black (<5% reflectance) targets at various depths to calculate absorption and reflectance parameters which could then be applied to imagery with known bathymetry. Algorithmic correction methods that rely on the spectral information as input parameters, however, are limited by the quality of the data and therefore by optical depth. The interested reader is directed to the methodology of [23] for a sample application of pre-existing algorithms.

Akkaynak and Treibitz [149] have developed the Sea-thru water column correction model, to represent the physical interactions of light in the water column. Sea-thru considers that the backscattering and diffuse attenuation coefficients differ and that these coefficients change amongst bands and images. The method therefore computes the two different coefficients for each band and image using each image itself as the input data. The developers show that Sea-thru can effectively be used to remove the effect of the water column in large RGB images sets [149]; its applicability to MSI and HSI has not yet been determined.

As for atmospheric correction, planning for depth correction should begin before data collection to ensure that all data needed to facilitate later processing is collected. For example, Davie et al. [52] incorporated a color correction key into the field of view of their camera during imagery collection using a customized system of mirrors installed on their low-cost AUV. Knowing the above-water reflectance of each color in the key as measured by the camera, they calculated the attenuation of each RGB band for every image. They were then able to distinguish between algae, sand and rock reliably [52].

Evaluating the results of water-column corrections has not yet been a prominent area of research, though some work has evaluated individual models [23,143,150,151]. For example, O'Neill and Costa [23] compared the water-column corrected spectra achieved through algorithmic manipulation to the "true" measurements of the substrates laid out on a dry, black

background. It was found that the water column correction's success was dependent on depth and wavelength considered. Purkis and Pasterkamp [143] evaluated the performance of a water column correction method applied at five different complexity levels and found that only the two most complex correction methods provided at least moderate classification accuracies [143]. Evaluating the performances of various correction methods against one another cannot always be easily done as each model is best suited to a set of conditions; it is impossible for any one method to be deemed "best" across all aquatic ecosystems [44]. Researchers should therefore carefully examine the assumptions and constraints of a model before applying it to their data.

The air-water interface complicates the analysis of RS imagery because of white caps, sun glint, wave action, reflection and refraction. White caps and sun glint increase the radiation reflected towards the sensor [21]. The best way to minimize the impact of sun glint and wave action is to collect imagery during calm surface conditions, gathering imagery when the sun is at a 15° to 30° elevation angle and travelling along a path perpendicular to the incident sunlight [21,23,50,152,153]. The methods for removing the effect of glint can rely on statistical models of the water surface behavior according to atmospheric conditions (i.e., wind) or on spectral analysis of the imagery itself, and they are inconsistently effective across water conditions [152]. Algorithms used to remove the effect of sun glint often rely on the assumptions that there is no upwelling radiance in deep water pixels or in certain wavelengths that are heavily absorbed by water [152,154-156]. If these methods are not appropriate or effective on the imagery under investigation, sun glint pixels may simply be masked out. To the best of our knowledge, there are no analogous algorithms to correct pixels affected by white caps; these are instead masked out or not used in the analyses.

When imagery is collected with the sensor nadir to the water's surface—and the radiance reaching the sensor is therefore largely perpendicular to the water's surface—refraction and reflection have very minor effects on the radiation's path. However, as the angle of incidence increases (away from the nadir) a higher percentage of the light is reflected and the path of light is altered through refraction [50]. When waves disrupt the water's surface, the angle of incidence of light is altered and becomes inconsistent across the image, thus producing inconsistent reflection and refraction between pixels and across time. Though these distortions can be small in magnitude, they add uncertainty to the locations, shapes and reflectances of objects. Fluid

lensing [55] is a new analytical method to account for such wave distortions. Fluid lensing uses very high frequency videography to track the movement of waves and identify where the wave crests are in each frame. By reconstructing a scene using only image segments affected by wave crests, fluid lensing homogenizes the effect of waves across the composite scene, effectively removing distortion. It also exploits the magnification caused by convex wave crests to increase the spatial resolution of the imagery without changing the system configuration [55].

Finally, refraction diffuses upwelling radiance as it re-enters air, resulting in the above-water radiance intensity being only roughly 54% of the below-water radiance per unit area [50]. This produces a weaker at-sensor signal than would have been measured just below the water's surface. Researchers primarily account for the effects of reflection and refraction by avoiding data collection on windy days and by using a nadir sensor configuration to reduce the angles of incidence and refraction.

2.8.3. Analysis of Passive Optical RS Imagery

Computer-aided image interpretation allows more imagery to be analyzed more rapidly than ever before. This has expanded the use of quantitative analysis as compared to the previous largely qualitative, manual, visual interpretation of SAV cover and canopy density. However, while digital analysis is faster, it is limited by the information available to the model being implemented [17]. For computer-aided analysis of MSI or HSI to be accurate, the data used to train the model or classifier must represent the total variation of a scene. Some of the most common computer-aided analyses applied in SAV research are described below. Readers are directed to [157-161] for examples of the quantitative analysis of photographs not covered here.

2.8.3.1. Hyperspectral Dimension Reduction

Hyperspectral imagers produce highly complex data. The large number of bands (e.g., >100) requires unfeasibly large training sample sets for pixels to be accurately recognized in classification processes if all bands are used [162,163]. Figure 2.12 presents a theoretical illustration of the decrease in recognition accuracy for various training set sizes as the datasets being examined become more complex. Classification on the fully spectral set of HSI often therefore produces results of limited accuracy. High dimensional data (the dimensionality being equal to the number of bands being considered) can, however, be projected onto a lower dimension, thus reducing the complexity, without losing much useful information. This is the

foundational theory of dimension reduction [162]. Per Figure 2.12, dimension reduction improves the accuracy of both target detection and scene classification because in addition to decreasing the complexity it effectively eliminates redundant (and often correlated) bands. It additionally reduces process times and storage requirements by reducing the amount of data being worked with [162]. Dimension reduction can be performed in a variety of ways. The most common methods include band/feature selection and the orthogonal transformation methods of principal component analysis (PCA) and minimum noise fraction (MNF).

Band selection, also referred to as feature selection, entails sub-setting the available spectral bands to the optimal set for analysis of a given problem [58,164-166]. Importantly, band selection retains the original units and physical meaning of the data, as opposed to transformations which do not. Bands are selected if they are both relevant and not redundant by maximizing the accuracy of the analysis (e.g., classification) [166,167]. A band is considered relevant if its inclusion improves the prediction accuracy of the chosen model, that is, if it contains useful discriminatory information about the target. A band is not redundant if it is not completely correlated with another band or set of bands included in the subset [166]. Feature selection can be performed with a variety of algorithms (see [167] for a review). Some biological and ecological researchers have successfully used statistical methods such as ANOVA or SIMPER to perform band selection (e.g., [58,87]), however these methods are not recommended for high dimension data as they do not consider band redundancy or classification accuracy.

Transformations change the units of the features being considered by combining multiple features into one or through rotation to produce orthogonal features (e.g., PCA). Using transformative dimension reduction methods can produce more accurate classification results than using feature selection algorithms but the features produced through transformation may not be easily interpretable as they are no longer directly related to the target's physical state [166]. The PCA and MNF transformations follow the same principle of producing orthogonal component vectors; PCA orders the vectors according to variance while MNF orders the transformed components according to SNR [168].

2.8.3.2. Indices

Spectral Vegetation Indices (SVIs), such as the most widely used Normalized Difference Vegetation Index (NDVI) [169], can be used to distill single values from multiple bands,

simplifying analysis and comparison across different locations or times. Different materials have different SVI value ranges, thus pixels can be labelled as a certain material based on which range their calculated SVI value falls into. Table 2.3 presents several vegetation indices that have been applied to SAV, their formulas and a selection of one or more sources that have applied each index.

Although originally developed for broadband terrestrial satellite imagery, NDVI remains one of the most popular SVIs for vegetation-related RS research. Recent work by Costa et al. [29] showed that NDVI can accurately estimate seagrass biomass without requiring destructive sampling [29]. Some work contests the utility of NDVI in underwater studies because of the high absorption of red and NIR radiation by the water column [33,170]. Espel et al. [171] found that using NDVI and the Green-Red Vegetation Index (GRVI) produced worse classification results than using the band values themselves [171]. Hyun et al. [172] found that while NDVI was not suitable for detecting SAV in raw imagery, it can be effective if the attenuation according to depth is accounted for.

The obstacle of IR attenuation has also been addressed by modifying the NDVI to use the red edge region instead of NIR [173]. Indices such as the normalized difference aquatic vegetation index (NDAVI) and the water adjusted vegetation index (WAVI) were developed with the aquatic medium in mind and have been shown to produce better separability in the aquatic environment than other SVIs presented in the literature [174,175]. The normalized total pigment to Chl-a ratio index (NPCI) provides an indication of vegetation health by analyzing the ratio of total pigments to Chl-a, as healthy vegetation tends to have more Chl-a than other pigments [170]. Some researchers have also performed successful analysis using indices they developed for their specific study and targets [176]. As expected, each index may perform best for different conditions and retrieves different vegetation characteristics [177]. Combining indices can also provide additional information, such as estimates of ecological diversity [25]. In addition to being used as primary tools of analysis, index values can be used as variables in more advanced analyses like decision trees [178,179].

It is vital to remember that indices are developed with a specific sensor and application in mind. They do not therefore necessarily translate well when applied to different sensors, environments or questions; their function and structure should be thoroughly examined before

adopting an index from one project to another. Additionally, indices are all designed to be applied to the reflectance values of imagery, not the radiance or DN. They can therefore only be properly applied to radiometrically and atmospherically corrected imagery.

2.8.3.3. Classification and Target Detection

Many SAV research questions in RS studies are answered with classification and target detection analyses. Classifications assign a thematic identity (label) to most/every pixel in an image using either a spectral library provided by the researcher, training pixels from the image itself or statistical measures of separability (i.e., unsupervised clustering). The results of classifications illustrate how multiple materials known to be present are distributed throughout a scene. Target detection locates pixels in an image that resemble a reference spectrum and is usually employed to verify if and where a material of interest occurs in a scene [180]. Classification and target detection can be used to determine SAV extent, canopy density, stressors (such as disease and salinity), the taxonomic composition of a canopy and where a SAV species occurs [22,170,178,181-183].

Supervised classification requires the user to identify materials of interest in a scene according to previous knowledge, ground-truths or other data sources. The pixels identified compose a set of training data for each known material in the image [49]. One method, the Spectral Angle Mapper (SAM), interprets each spectrum as a vector in *n*-dimensional space, where *n* equals the number of bands. The angle between a reference spectrum and the pixel spectrum is calculated and should the angle fall within a defined threshold, the pixel is labelled as that reference material [184]. SAM therefore evaluates the shape of the spectra but not the magnitude, which is beneficial when examining imagery with uneven illumination conditions such as underwater environments affected by waves [128]. Species discrimination through classification is possible but spectral differences may be subtle and there is often relatively high intraspecific variation and low interspecific variation [17,18]. Including spatial information, as is done in object-based image analysis (OBIA) through grouping contiguous sets of spectrally similar pixels together, can further improve classification results by analyzing patterns of pixel distributions [38,185,186].

Target detection (e.g., Adaptive Coherence Estimator, Mixture Tuned Matched Filter, etc.) identifies if and where a single target material of interest exists in a scene and is typically

employed for rare or scarce materials [180]. If the target material is abundant, the classification methods described above usually suffice. Target detection would therefore be used in SAV studies in applications such as detecting if an invasive species is present or mapping the distribution of an endangered species. Statistical target detection relies on probabilistic tests, such as the likelihood ratio test or the generalized likelihood ratio test [187]. In these statistical approaches, the null hypothesis of the target material not being present in a pixel is tested against the alternative hypothesis that the pixel contains the target material. This process produces a map in which each pixel is either target or background. In all such tests, the probability threshold is inversely related to the odds of recording a false positive [187]. If, for example, it is vital that every individual of an invasive plant is flagged, the user can set a low probability threshold. This will improve the chance that all pixels containing the invader are found, though there may be more false alarms.

Considering that pixels may be larger than the ground features they represent and the way optical images are generated (e.g., see [121]), several materials often contribute to the measured signal of a pixel. Unmixing estimates how much of a pixel's signal originates from each of the possible materials and thus relatively how much of each material there is in the pixel. Unmixing methods follow one of two general assumptions: the contributions are either linear or non-linear. Linear mixing infers that a material's contribution is directly proportional to its relative surface coverage of the pixel [168,188]. Non-linear mixing occurs when the materials within a pixel are mixed homogeneously or when there are multiple reflections of light between the different materials [168]. Non-linear mixing may also arise when materials partially transmit light, such as in the case of thin leaves, allowing the underlying materials to contribute to the signal without being considered as "cover." In these situations, the spectral contribution is indirectly related to the material's cover and the relative abundance is more difficult to calculate.

Due to the reduced growing season in temperate latitudes, SAV matures and senesces rapidly relative to terrestrial plants. This means that the pigment concentrations and leaf structures in macrophytes that are the primary determinants of their reflectance spectra can vary widely depending on the date of observation [57]. Seasonality thus influences the separability of different species of SAV and thereby can affect how successful classification and target detection analysis is. Some research has shown that the end of the growing cycle is best suited for discrimination between species [71].

2.8.3.4. Time-Series and Time Sequence Analyses

Time series and time sequence analyses present a special problem in image analysis because of atmospheric variability. Time series refers to multiple measurement acquired equally spaced in time, whereas time sequence refers to multiple measures with varying sampling intervals. Time series analyses are popular in SAV studies to examine the dynamics of a population's or a community's spread and growth [189-191]. In monitoring applications, temporal analysis can be used to examine if a management program is effective [192]. Time series and time sequence analyses can be done in a variety of ways, common examples of which are described below.

Post-classification comparison (PPC) detects changes in environmental variables by classifying two images of the same scene from different times and identifying the differences between the classification results. This, though, means that an error in the first image that did not occur in the second image and vice versa, would be falsely marked as a change, thus compounding the likelihood of misclassifications over time [71]. Such compounding errors can be reduced using the alternate method of temporal image differencing (TID). In TID, one image is classified, then the values of a single band in both images are used to identify a change if the difference in band values between two corresponding pixels is above a defined threshold. TID's success is dependent on a reliable classification of the original image and appropriate selection of the band to be compared [49].

If the analysis is being performed on reflectance images or transformed data with many bands (e.g., stack of SVIs from different dates), Change Vector Analysis (CVA) is recommended as it can consider all bands at once. In CVA, an *n*-dimensional vector is created to represent the change between the spectra of two co-registered pixels from different images in a time series. The vector is then assessed against a user-defined magnitude threshold. This analysis technique allows for intra-group variation to be classified as static depending on the threshold and is therefore valuable when classifying complex materials, such as vegetation [71].

2.8.4. Structure-from-Motion Photogrammetry

Analysis of optical MSI or HSI largely focuses on the reflectance values that provide information on the composition of the scene. An image is, however, a two-dimensional representation of a three-dimensional surface; structural information is not captured.

Structure-from-Motion Multiview Stereo photogrammetry (SfM-MVS) analysis on a set of 2-D photographs recreates the 3-D surface of a landscape for structural applications. Photographs should be collected in a grid pattern with high overlap between neighboring images. Common points, seen from different angles in different photographs, can be used to infer the relative external orientation and internal camera parameters (e.g., focal length) of the photographs—and thus the position of the points therein—to create a 3-D point cloud [31,193,194]. The surfaces between the points in the cloud can then be connected to produce a 3-D mesh or interpolated to create a Digital Elevation Model (DEM), as outlined in Figure 2.13. The reader is referred to [194] for a detailed description of the process.

3-D meshes produced through SfM-MVS can be used as visualization products, VR simulations or as data inputs for qualitative or quantitative analysis. The use of SfM-MVS has been endorsed as a time and cost-efficient method of filling in the data gaps in nearshore bathymetry and ground cover maps [195]. Rugosity, grain size and fractal dimension are important physical traits in classifying aquatic habitats and can all be computed through quantitative analysis of DEMs or 3-D mesh surfaces [193,196]. Measures from an SfM-MVS model are often more accurate and precise than traditional methods and can be applied to an entire scene as opposed to the few transects that can reasonably be conducted in situ [197]. Canopy volume and plant biomass information can also be reliably estimated using DEMs produced through SfM-MVS of terrestrial and emergent vegetation [198], though it has yet to be demonstrated for SAV. SfM-MVS can create very high-resolution digital elevation models when LiDAR is unavailable [31,199], such as in the case of most underwater research. SfM-MVS has been a popular tool for studying highly structured environments such as coral reefs (e.g., [200,201]) but has yet to see the same level of adoption in SAV studies. Recent work by Kalacska et al. [193] demonstrates the viability of applying SfM-MVS to freshwater fluvial environments and provides a preliminary set of recommendations on employing the method in such ecosystems. An example of an SfM-MVS 3D point cloud of a tropical freshwater river with emergent, floating and submerged macrophytes is shown in Figure 2.14.

SfM-MVS relies on the scene being immobile so that the relationships between different points is consistent. This is not always possible underwater. Variable currents, wave action and researcher disturbances can all cause the vegetation being imaged to move, especially so for tall

vegetation. SfM-MVS is therefore best suited to short or carpeting SAV, in calm waters, with an experienced photographer that is an adept swimmer.

2.9. Applications

Previous applications of RS to the aquatic environment have included work in freshwater, brackish and marine ecosystems and have answered a variety of spatially explicit questions. In the case of SAV studies, these can be largely broken down into: "What SAV is here?" and, "where is this SAV found?" The first is an identification problem, either of the species, growth type or another biophysical state, while the second is a question of mapping extent or presence and absence. This section presents a selection of previous work to provide insights when considering implementing RS for SAV research.

2.9.1. Identification

Determining if a group of species are distinct from one another is often the first step in studies aiming to map vegetation at the species level. McIlwaine et al. [87] extensively examined the spectral separability of eight macroalgal species. These analyses identified which bands were most valuable in discriminating species and higher-level groups. While not all species could be differentiated, three groups were spectrally distinct as were pairs of species from separate groups. Everitt et al. [202] similarly evaluated the spectral separability of nine freshwater SAV species using multiple comparison analysis and stepwise discriminant analysis to select the best bands for spectral discrimination. The consequent species classification using the identified bands was between 96.3% and 100% accurate [202].

Besides examining species, Fyfe [58] investigated the effect of habitat type, season and fouling on spectral response. She conducted statistical analyses on the profiles of leaves collected across three sites and two years to determine if three species of seagrasses, *Zostera capricorni*, *Posidonia australis* and *Halophila ovalis*, are spectrally distinct. The seagrasses were separable when considering the VIS-NIR region and the VIS alone, suggesting that these spectral differences should be perceivable through a water column. Additionally, there were consistent patterns of intraspecific variation between samples of *Z. capricorni* grown in brackish and marine habitats [58]. This suggests that some intraspecific variation could be both a product and indication of SAV habitat.

At the canopy-level, Dierssen et al. [203] used PRISM airborne imagery to differentiate between species of seagrass and macroalgae that form wracks off the coast of Florida. During analysis, the researchers employed indices such as NDVI and the floating algal index to identify vegetation at or near the surface. The fine spectral (2.83 nm bandwidth from 349.9 nm to 1053.5 nm) and spatial resolutions (1 m) afforded by the PRISM sensor allowed them to discern between the types of vegetation and age the debris in the wracks [203].

Visser et al. [26] used sub-resolution data from hand-held and UAV-mounted sensors to perform OBIA when spectral analysis alone was unable to discriminate between species. By combining the texture, shape and spectral information of the targets, they successfully distinguished three species of SAV. Later, Visser et al. [38] expanded on the OBIA method to discriminate between five species of SAV, areas of species mixing, general vegetation and background materials. They used spectral thresholds in multiple bands and geometric analysis to identify plants' properties such as stem length or leaf shape. Although the classification accuracy was modest (61% overall accuracy), they believe that OBIA shows promise in SAV research [38].

Brooks et al. [173] gathered data using hand-held, vessel-mounted and UAV-mounted sensors to determine if the invasive *Myriophyllum spicatum* could be discriminated from amongst the other SAV species present. Analysis using full-dimensional multispectral measurements could not successfully distinguish *M. spicatum* from the background vegetation. Hyperspectral data and multispectral data transformed into modified NDVI values, however, did show *M. spicatum* to be distinct from native vegetation.

When taxonomy is unimportant, SAV can be identified by growth type or physiological characteristics. To do so, Chen et al. [178] used 16 m spatial resolution, 4-band GF-1 satellite imagery, field measurements and a decision tree analysis using band ratios to classify emergent vegetation, submerged vegetation and alga with over 90% accuracy. Seasonality and canopy density were critical determinants of separability while the spatial resolution of the imagery was shown to limit the max separability as the large pixels often contained more than one material. The methods used produced inconsistent classification accuracies with changes in depth and water type [178]. Nelson et al. [40] used the larger 30 m spatial resolution, 6-band Landsat 5 TM imagery of a set of Michigan lakes to test how well macrophyte growth types could be predicted

through modelling. While the model they produced performed well (61–98% classification accuracy) for the calibration lakes, it did poorly when applied to a set of validation lakes [40]. This inconsistent model success is potentially due to the lack of variation captured by their set of calibration lakes which thereby limits the conditions that the model is suited to. This work highlights both the strong potential of RS as a monitoring tool and the need for extensive input data in developing robust classification models. Finally, Rotta et al. [62] calculated bottom-reflectance index values from SPOT-6 imagery and related those values to field observations to infer SAV height. Though the model produced only moderate accuracy (R^2 = 0.54) and was limited to depths of less than roughly 5 m, further calibration could improve the model's performance [62].

2.9.2. Location of SAV (Extent Mapping)

Detection studies seek to locate targets, such as community extent, a certain SAV species or a growth type. Simple band ratios have been shown to be effective at detecting SAV extent in shallow waters from Landsat imagery [59] though their success depends on water depth and the SAV being detected. In mapping community extent and density with Landsat imagery, Ackleson and Klemas [22] found that the unsupervised classification algorithm produced more accurate results when pixels over deep water were masked out. The deep-water pixels were confused with dense canopy cover and vice versa [22]. Wolter et al. [16] found that incorporating a multitemporal differencing technique improved classification accuracy. By subtracting the red reflectance at the start from the end of the growing season and using this difference as a band along with the visible green and red, the effect of the water column was reduced and SAV was more reliably detected [16]. Work by Giardino et al. [204] combined mapping community extent and species identification. Water column constituent concentrations, depth and SAV community extent were modelled using field measurements and airborne MSI as input data. They thereby probabilistically classified the bottom cover as *Chara* ssp., other SAV or substrate [204]. Santos et al. [191] used airborne HSI spanning several years to examine the dynamics of a community of invasive species at the scale of a 2220 km^2 delta. They found that there was a slightly negative spread rate of the invader across the study time and a relatively short inter-annual persistence which suggests that the invasion may be weakened with time [191].

Locating a species of SAV instead of a community may require different data and analyses. Williams et al. [205] conducted a preliminary exercise of species mapping using hyperspectral airborne imagery to match the spectral features of two species to those present in pixels' spectra. The contributions of active water column constituents, such as chlorophylls, were minimized through band selection. Although the results seemed align with reality, the lack of appropriate validation data meant that no measure of accuracy could be calculated [205]. O'Neill and Costa [23] mapped the extent of *Zostera marina* using both airborne and high-resolution satellite imagery. They found that performing dimension reduction on the airborne imagery produced the most accurate results and that the products of different classification algorithms varied widely. Notably, the map accuracy decreased after water column correction because of the additional error introduced, highlighting the importance of appropriate and verified water column corrections. Such species-specific mapping is especially valuable considering invasive species. Kumar et al. [206] used Landsat 8 imagery as input data to a model of the invasive *Hydrilla verticillata*'s presence. The model effectively predicted *H. verticillata*'s presence/absence as validated by a concurrent field campaign [206]. Such models allow managers to better and more frequently monitor plant growth and the effects of their control efforts.

In a study comparing macrophyte monitoring techniques, Stocks et al. [41] had two teams of researchers use hydroacoustic sensors, satellite imagery and hand-held geolocation devices to create maps of macrophyte cover in two lentic environments with different turbidity levels. In comparing the resulting maps between teams and amongst techniques, they found that vertical hydroacoustic and optical RS methods were consistent between operators while acoustic side-scanning and manual delineation of polygons were subject to user error. In turbid waters, the vertically oriented acoustic data far outperformed the optical footage taken from an RGB camera [41]. Vis et al. [24] similarly conducted a cross validation experiment to compare the utility of various SAV extent mapping methods. In comparing optical RS, hydroacoustic data and three environmental models, they found that optical RS was the least accurate. However, the available optical imagery was 10 years older than the ground data and had been spatially resampled to a coarser size. The significant temporal and spatial variability in macrophyte communities and the lag between imagery and reference data collection could explain why optical RS was shown to be inaccurate. Echo sounding RS was shown to be the most accurate method of detecting macrophyte type, supporting the use of this technology for SAV studies in turbid waters [24]. As

inland waters are often turbid and this turbidity varies over space and time, the ability to operate both optical and acoustic sensors (and combine them if necessary) is an asset for lentic or fluvial RS researchers.

Nahirnick et al. [207] used an off-the-shelf, consumer grade UAV and RGB Go Pro camera to collect very fine resolution imagery of the *Z. marina* habitat in three locations. Using SfM-MVS postprocessing to produce an accurate orthomosaic, they mapped presence and absence with 86.5% to 96.3% accuracy [207]. They found that using OBIA helped achieve high accuracy classifications on images with varying illumination and environmental conditions [207].

2.10. Discussion

As with most new technologies, the regulatory environment surrounding low altitude or surface RS is still in development and may differ amongst governments. It can however be largely broken down into two categories: policies regulating the platforms and those regulating data collection. Satellite RS is governed by international laws, such as the Outer Space Treaty or various United Nations resolutions, as satellites do not orbit in the territory of any State and States can collect imagery of one another [208]; a discussion of the legalities of satellite RS is presented in [208].

Legislation regarding the use of platforms such as aircraft, UAVs or vessels are primarily concerned with safe operation and respecting territorial boundaries. Aircraft and vessels must follow all relevant licensing, operational and navigational regulations in the study's administrative district(s). Most localities also have regulations relating to un-manned flight. In Canada for example, all UAVs over 250 g must be federally registered and flown by a licensed pilot. They cannot be flown near airports or in military airspace without permission and permission is also required for operations within a national park [209]. Operations may also be restricted near or over bystanders minimize the risk of personal injury. The American Federal Aviation Association has implemented similar regulations for all UAVs in their airspace [114].

Recent advances in aquatic RS have focused on post-processing methodologies and analytical tools. Data collection procedures however are not yet standardized, making comparisons across studies of the same location difficult, and studies of different locations or by different researchers can rarely be meaningfully compared. Spectroradiometer measurements are heavily influenced by the collection conditions, may not be reproducible and contain

uncertainties and sources of error that are not well defined [210]. Without a widespread commitment to normalizing data and to quantifying uncertainties during data collection, processing and analysis, users can be left with little idea of how representative the data are. This is an area of intense focus and effort for the European Space Agency, through the Quality Assurance Framework for Earth Observation and NASA, through their Earth Science Data and Information System Standards Office [211,212].

When used appropriately, RS is a novel tool for policymakers and ecosystem managers across the globe. However, the current lead time and expertise needed for a beginner to implement a new RS system is an obstacle. Automation is therefore a primary goal for aquatic RS [23]. Being able to produce reliable, rapid and accurate information without extensive user input would allow the proliferation of RS into environmental management. Complete automation is unlikely but advances such as creating more complete spectral libraries will make RS more user-friendly and widely applied [23,46].

Besides applying RS to the identification and detection of SAV, there has been progress in harnessing it to collect data as environmental variables for modelling. Research projects such as the "Spectral Library of Dutch Waters" have endeavored to gather spectral information and samples of a wide variety of water types and qualities to clarify the relationship between water column constituents and spectral response [213]. The Bio-ORACLE (Ocean Rasters for Analysis of CLimate and Environment) database, for example, contains 23 global rasters incorporating satellite and in situ measurements that can be used for modelling shallow water species distributions [25]. The Ocean Biogeographical Information System (OBIS) database for marine biodiversity research illustrates regional disparities in marine RS research. Creating a global network of aquatic RS infrastructure and researchers could efficiently fill these data gaps. Developing such databases will allow more accurate modelling and predictions considering the changing climate.

2.11. Conclusions

Inland and marine aquatic habitats rely heavily on SAV for the ecosystem services they provide. SAV communities are changing across the planet; extensive monitoring is therefore desperately needed. RS provides a time, cost and labor efficient monitoring method for large

scale SAV studies. The interactions between light, the water's surface and the water column, however, complicate the analysis of aquatic RS data compared to terrestrial studies.

Still, SAV has been accurately and efficiently monitored using RS in clear, shallow waters. Depth and turbidity obscure the measured reflectance of SAV and thereby reduce the accuracy with which RS can be applied to detect and identify SAV. There are a variety of empirical and analytic models available to correct for the effects of the water column; not all models are successful in all water conditions and there has yet to be a comprehensive evaluation of these methods. High spatial, spectral, radiometric and temporal resolutions are vital to achieving meaningful and accurate results in SAV studies due to the strong similarities between benthic substrates, patchiness of SAV growth, weak water-leaving signal and rapid development of SAV, respectively.

Using RS to map the extent of SAV cover has been most explored in previous applications and has produced remarkably accurate results (up to 99% overall classification accuracy). Other applications that seek to examine SAV at a more granular level (canopy density, growth type, species extent, etc.) have been less well explored. Data fusion techniques that allow users to more readily combine datasets are likely to improve the performance of these higher-level investigations.

Technological innovations—like PRISM, WISE, SHOALS and MiDAR—are producing raw data that are more appropriate to aquatic applications than traditional sensors. Computational advances, such as Sea-Thru and fluid lensing, are improving the water column corrections and providing researchers ever-more accurate and detailed information about the benthic environment. Combined, these advancements will allow researchers to ask more complex questions and produce more accurate results for a larger range of ecosystems. With this anticipated high-quality imagery and an understanding of RS, ecosystem managers could create targeted conservation and preservation plans (e.g., weeding out invasive species before they establish themselves; protecting endangered species and spawning sites; culling diseased individuals; or, optimizing SAV to improve water quality). This would improve the effectiveness and time- and cost-efficiency of conservation efforts.

There is a growing body of work applying RS to SAV monitoring. New analysis methods and sensors are being developed to better address the needs of the aquatic RS community. There

are concerted efforts by inter-organizational and international groups to create global RS data repositories for aquatic environments. SAV monitoring is a global priority plagued by high costs, labor intensity, access issues and limited spatial scale—problems for which RS is becoming a more and more attractive solution.

2.12. Tables and Figures

Table 2.1. A list of essential remote sensing concepts mentioned in this study that researchers new to remote sensing (RS) should familiarize themselves with. Readers are directed to explanatory resources such as [135,140,214] for further detail.

Concept	Definition
Acoustic remote sensing	Measures backscatter of acoustic waves which are vibrations of the medium (e.g., water) through which the waves propagate.
Active sensor	A sensor that generates its own signal to illuminate the target.
Anomaly detection	A type of target detection in which there is no a priori target information.
Classification	An analytical method in which pixels in an image are given a thematic label as belonging to groups that have either been defined by the user or algorithmically generated.
Full-Width-Half-Maximum (FWHM)	The width at half of the peak transmittance of the weighting function that describes the range of wavelengths a particular band is sensitive to. If a sensor has bands with narrow FWHMs finer spectral details can be resolved. For example, the uCASI (Figure 2.2a) has a narrow FWHM for each band (i.e., 2.6 nm) in contrast to 66 nm for band 2 of Sentinel-2.
Near Infrared (NIR)	The region of the electromagnetic spectrum between 700 nm and 1100 nm.
Optical remote sensing	Measures reflected electromagnetic radiation.
Passive sensor	A sensor that measures ambient energy, usually reflected solar radiation, thermal radiation, or microwaves.
Pixel size	The distance between pixels. It encompasses most of the area on the ground contributing signal to a pixel. Most often this metric is used to describe an image after it has been geometrically corrected to square pixels but can also refer to the raw unaltered geometry (see [121] for an example).

Table 2.1. (Continued)

Concept	Definition
Radiometric resolution	Distinct levels into which the incoming signal is divided, the number of which determines how many energy intensity levels can be distinguished as being different by the sensor. This is typically given in the form of bits used to encode the pixel values in binary format where each bit corresponds to an exponent of 2 (e.g., an 8-bit image has 2^8 or 256 digital numbers referred to as grey levels). Many modern imagers acquire data in 10, 12 or 14-bits.
Spatial resolution	The smallest resolvable detail achievable by a given system configuration. Spatial resolution can be divided as: very high < 1 m; high 1 m < x < 5 m; moderate 5 m < x < 30 m; low > 30 m.
Spectral profile/signature	Response of a sensor to radiation across wavelengths sensed. Often represented as a curve of radiation reflected by a target.
Spectral resolution	Ability of a sensor to define fine wavelength intervals. A finer spectral resolution allows for a narrower wavelength range for a particular band. While the number of bands recorded by a given sensor can range from < 10 to > 200, the narrowness of the spectral interval that can be resolved defines the resolution. This is often reported as the FWHM of the spectral response function of each band.
Target detection	An analysis method in which the known spectral, thermal, or microwave response of a material is located in an image.
Temporal resolution	The time interval between successive measurements of the same target.
Ultra-violet (UV)	The region of the electromagnetic spectrum between 270 nm and 400 nm.
Visible spectrum (VIS)	The region of the electromagnetic spectrum between 400 nm to 700 nm comprising all visible wavelengths of light.

Table 2.2. The types of remote sensors that have been commonly applied to the study and monitoring of SAV, categorized by type, energy measured and number of bands (*n*). Example sensors and sources detailing applications of these sensors are also listed.

Type	Energy	*n*	Name	Description	Examples	Sources
Active	Acoustic	1	Side-scan sonar	Emits energy from above, at or near the water's surface.	Hummingbird SSS	[41,77,215]
	Acoustic	1–2	Echo-sounder	Emits energy horizontally from within the water column.	DIDSON, DT- X, Sonic2024	[41,64,216,217]
	Electro-magnetic	1	Bathymetric LiDAR	Emits green light (~530 nm) that penetrates the water column.	SHOALS, EAARL	[72,218]
Passive	Electro-magnetic	1	Panchromatic	Film and digital sensors that are sensitive to a wide wavelength range of light (usually the VIS) and produce greyscale images comprised of a single band.	Film, PAN band on SPOT	[157,158]
		3	Red-Green-Blue (RGB)	Film and digital sensors that capture visible light to produce true color images.	DSLR camera, Go Pro	[83,185,207]
		4–30	Multispectral	Sensors that record up to 15 non-contiguous bands, potentially across the entire reflective optical spectrum.	Sequoia sensor, MEIS, Landsat	[186,219,220]
		30+	Hyperspectral	Sensors that record dozens to > 100 narrow, contiguous bands.	ASD fieldspec, CASI, Hyperion	[46,221,222]

Table 2.3. A selection of SVIs of interest in SAV studies, whether due to their popularity, target material or use. Their full names, abbreviations, equations and sources that use each are listed. L represents a water column correction factor determined for a specific image.

Name	Abbreviation	Equation	Source(s)
Normalized difference vegetation index	NDVI	$\frac{(NIR\ band - red\ band)}{(NIR\ band + red\ band)}$	[29,171,173,223]
Normalized difference aquatic vegetation index	NDAVI	$\frac{(NIR\ band - blue\ band)}{(NIR\ band + blue\ band)}$	[173-175]
Water-adjusted vegetation index	WAVI	$(1 + L) * \frac{(NIR\ band - red\ band)}{(NIR\ band + red\ band)}$	[173-175]
Green-red vegetation index	GRVI	$\frac{(green\ band - red\ band)}{(green\ band + red\ band)}$	[171]
Normalized total pigment to Chl-a ratio index	NPCI	$\frac{(red\ band - blue\ band)}{(red\ band + blue\ band)}$	[170]

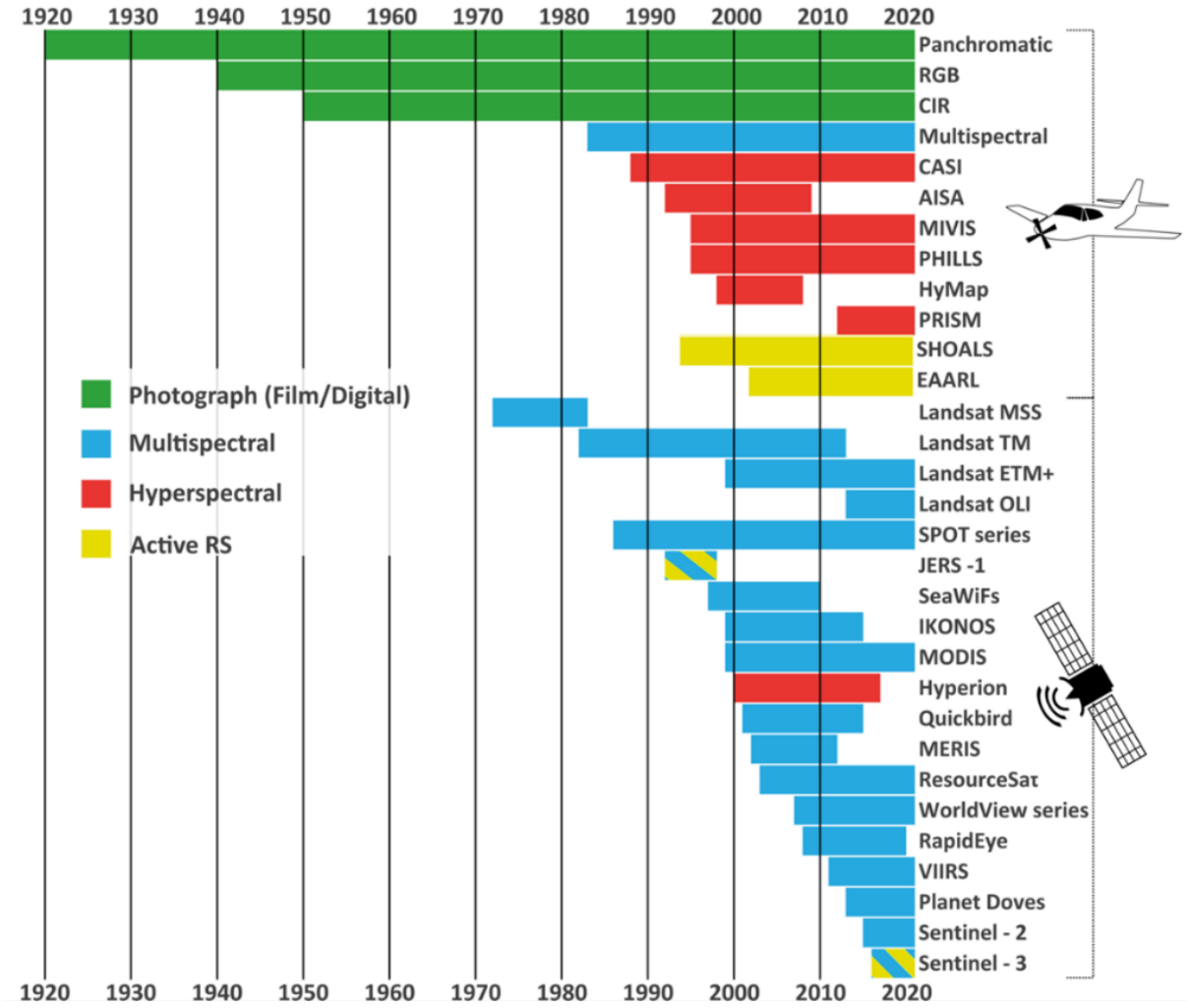

Figure 2.1. Operation chronology of a selection of remote sensors used in Submerged Aquatic Vegetation (SAV) research by platform and sensor type.

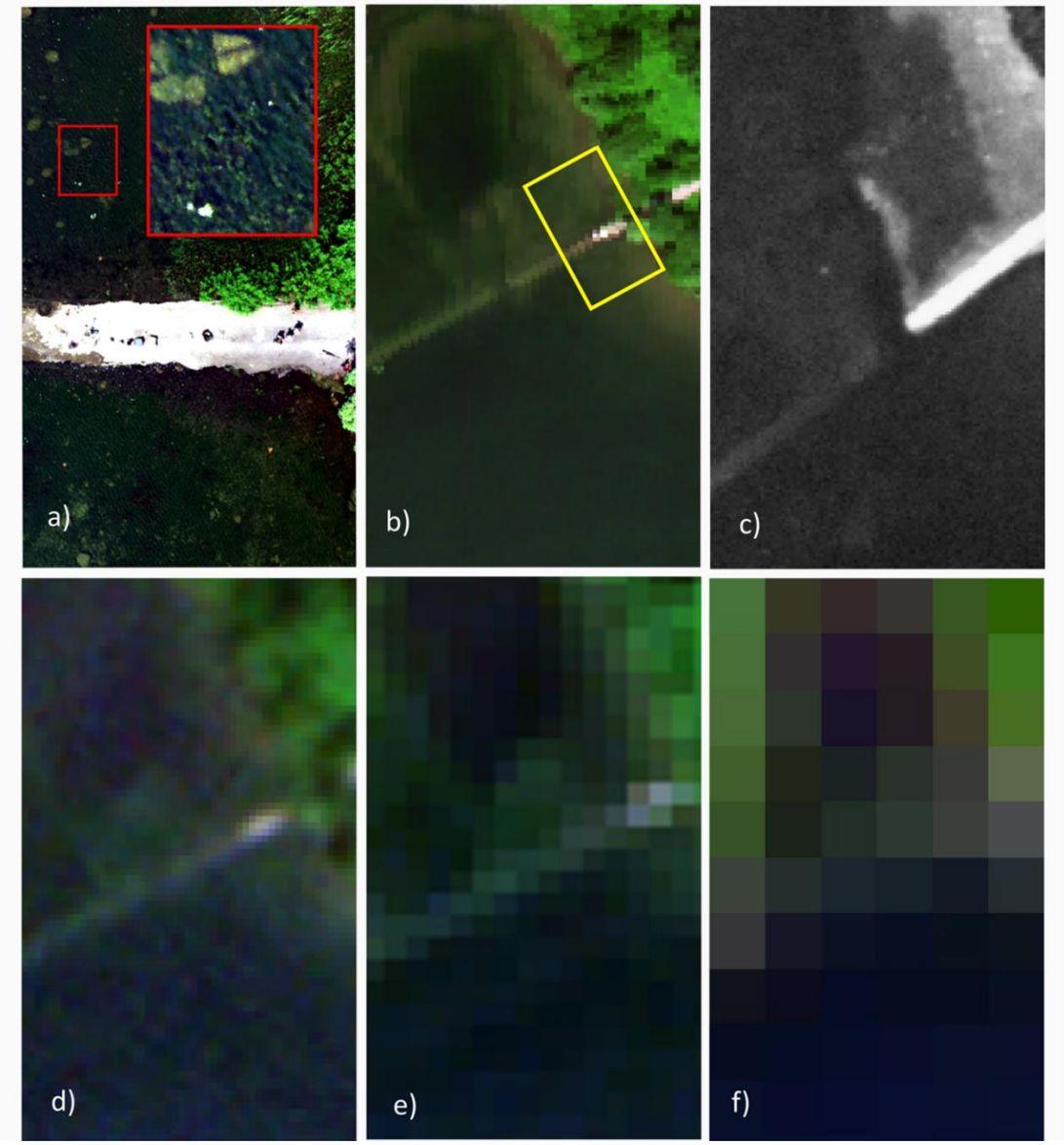

Figure 2.2. Comparison of spatial resolutions in representing natural and man-made features (most notably a flooded road) in the Saint-Lawrence River, Ontario, Canada. (**a**) 3 cm resampled pixel size image acquired from an unmanned aerial vehicle (UAV) platform with the uCASI sensor (288 spectral bands). Subset is shown as a true color composite R:648 nm/G:548 nm/B:449 nm. (**b**) 1 m resampled pixel size image acquired from an airborne hyperspectral platform (CASI-1500, 288 spectral bands) Subset is shown as a true color composite R:641 nm/G:550 nm/B:471 nm. The yellow box indicates the spatial extent of frame (**a**). (**c**) Panchromatic film photograph from a KH-9 satellite taken in 1980 at a spatial resolution of 2 to 4 feet. (**d**) 3 m resampled pixel size image from the commercial PlanetScope satellite constellation (Dove-PS CubeSat). (**e**) 10 m resampled pixel size Sentinel-2 satellite image. (**f**) 30 m resampled pixel size Landsat image. For d-f, the respective RGB bands are displayed as true color composites.

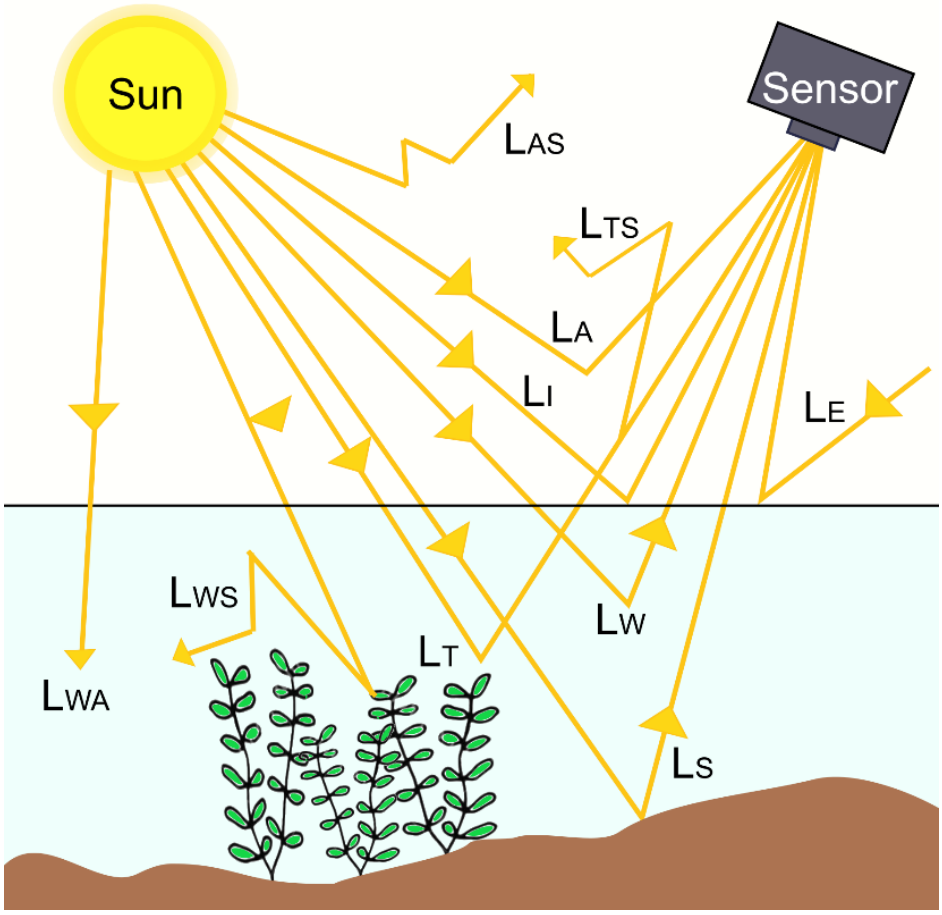

Figure 2.3. A simplified illustration of the interactions of light as they originate from the sun and are recorded by an optical sensor. The labels are as follows: L_T = Radiance reflected by the target; L_{TS} = Radiance reflected by the target then scattered out of the path to the sensor; L_S = Radiance reflected by the non-target substrate; L_A = Radiance reflected by the atmosphere to the sensor (also referred to as path radiance); L_{AS} = Radiance scattered by the atmosphere; L_W = Radiance reflected by the water column into the sensor; L_{WS} = Radiance scattered by the water column; L_{WA} = Radiance absorbed by the water column; L_I = Radiance reflected by the air-water interface; L_E = Radiance that is scattered into the scene by the ambient environment.

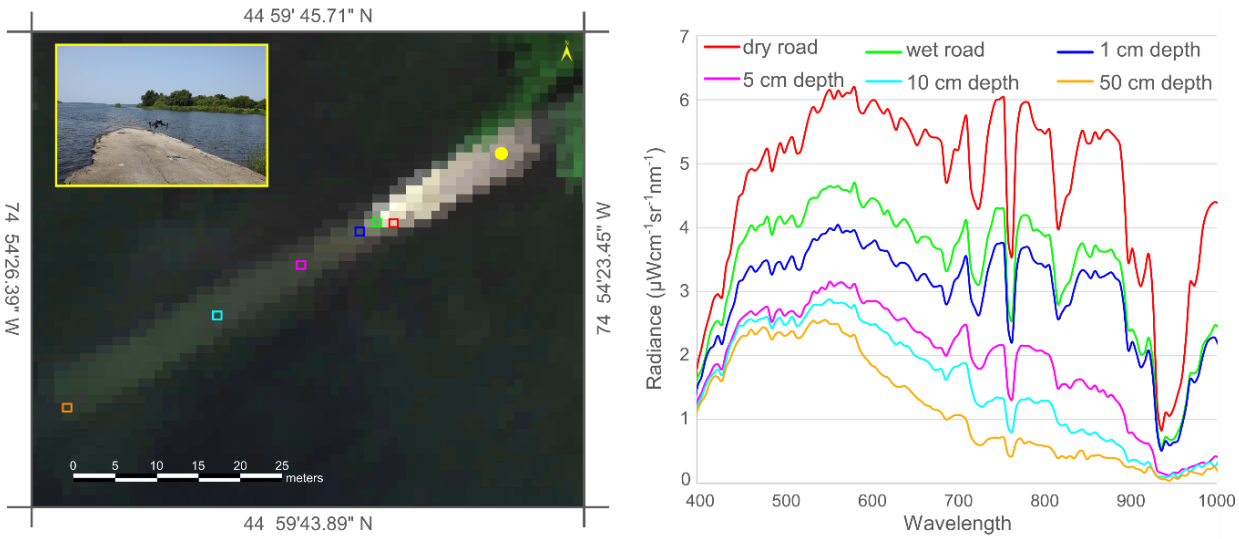

Figure 2.4. The attenuative effect of the water column on the recorded signals of a flooded cement road at the Long Sault Parkway, ON, from airborne hyperspectral imagery (HSI) (CASI-1500). The colored boxes identify the pixels for which the spectra are shown on the right in units of radiance. The pixels chosen represent an increasing effect of the water column, with the dry road pixel being entirely unaffected by water. The inset photo shows what the flooded road looks like from the ground and was taken at the point indicated by the yellow circle. Note that the spectra here are in radiance, prior to atmospheric correction, as such the strong atmospheric water absorption features (e.g., 940 nm) can be seen in the spectrum from the dry road.

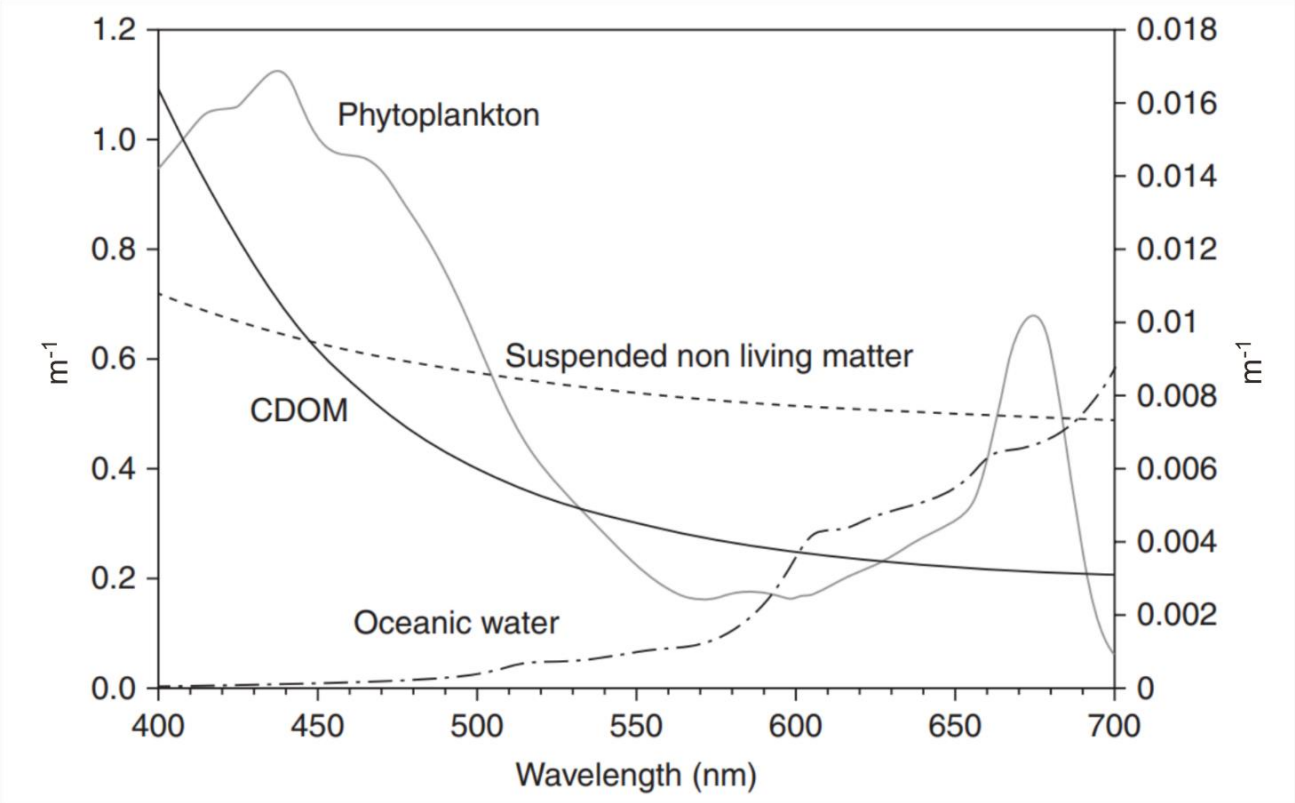

Figure 2.5. The absorption profiles of four major constituents of natural waters. “Oceanic water” refers to very clear seawater. Colored Dissolved Organic matter (CDOM), oceanic water and suspended non-living matter all use the primary axis; only the phytoplankton spectrum uses the secondary axis. Reprinted from Subsea Optics and Imaging, Johnsen et al., Underwater hyperspectral imagery to create biogeochemical maps of seafloor properties, 508-535. Copyright (2013), with permission from Elsevier[224].

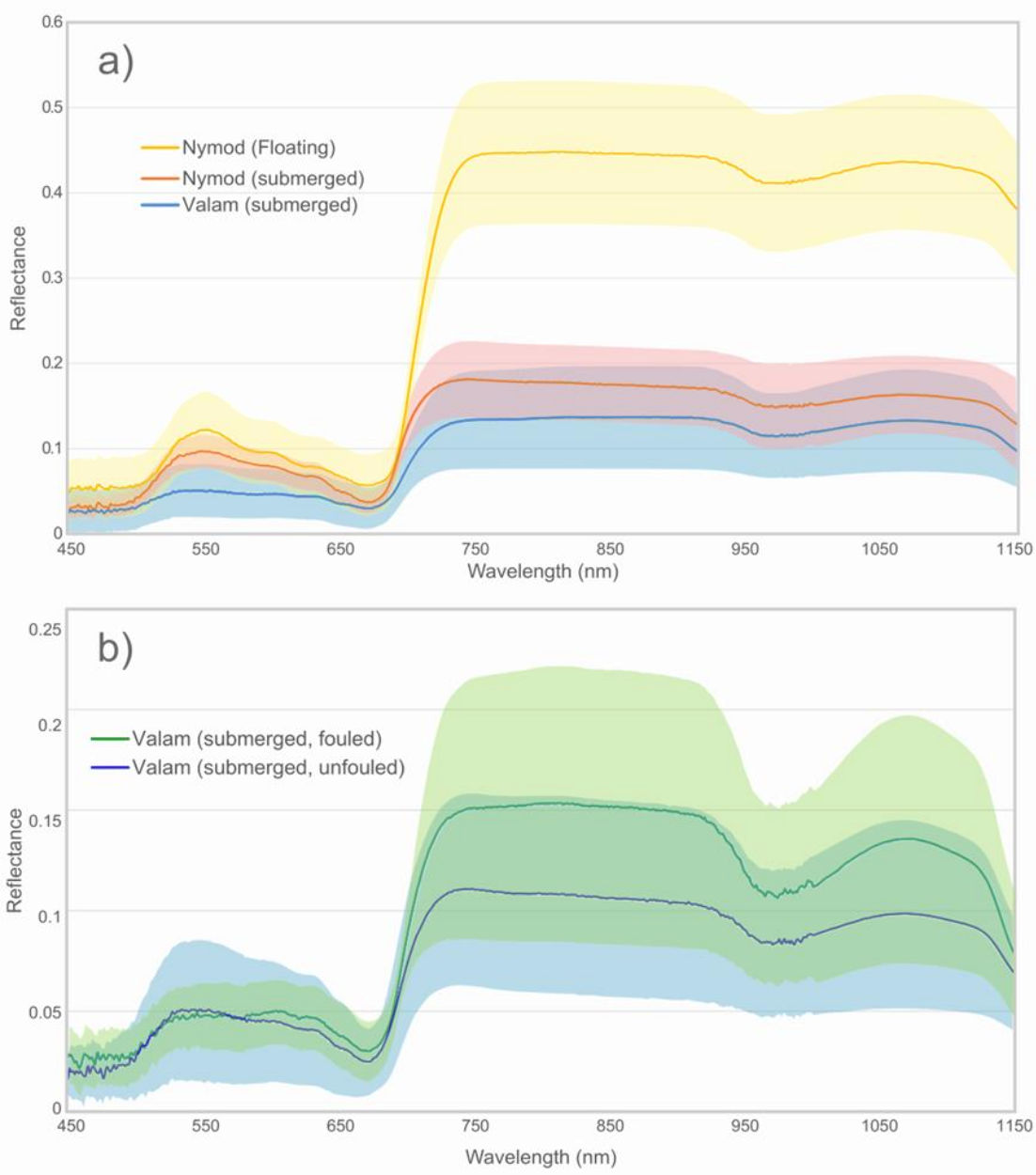

Figure 2.6. Examples of vegetation spectra, with one standard deviation from the mean shown as shading; (**a**) A comparison of the effect of a thin layer of water (<5 mm) on the measured reflectance of a single species and the difference in profile shape between species. Note the prominent green peak in the spectrum of Nymod near 550 nm and the red-edge around 680 nm. The measured spectra of the submerged plants are lower across the spectrum, especially so in the NIR region. Valam does not display as prominent a green peak due to its higher relative concentration of accessory pigments making the leaves appear reddish-brown. (**b**) A comparison of the effect of epibiont and sediment fouling on the same plant sample. The profile of the fouled plant has a different shape and less spectral variability in the visible region than that of the unfouled plant. Nymod = *Nymphaea odorata*; Valam = *Vallisnaria americana*.

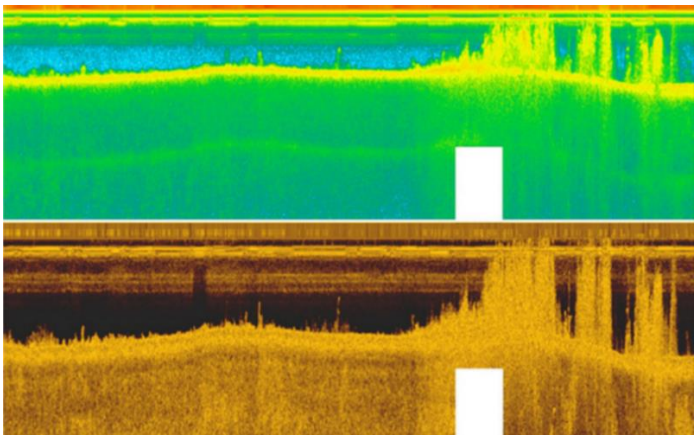

Figure 2.7. Output from a single beam echosounder at 200 kHz (**upper panel**) and 800 kHz (**lower panel**) wave frequency. Macrophyte presence is identified by the areas of signal reflections (in the upper right hand of each panel) above the lake bottom. From Stocks et al., 2019 used according to CC-BY-ND http://creativecommons.org/licenses/by-nd/4.0/. Accessed 07-10-2020 [41].

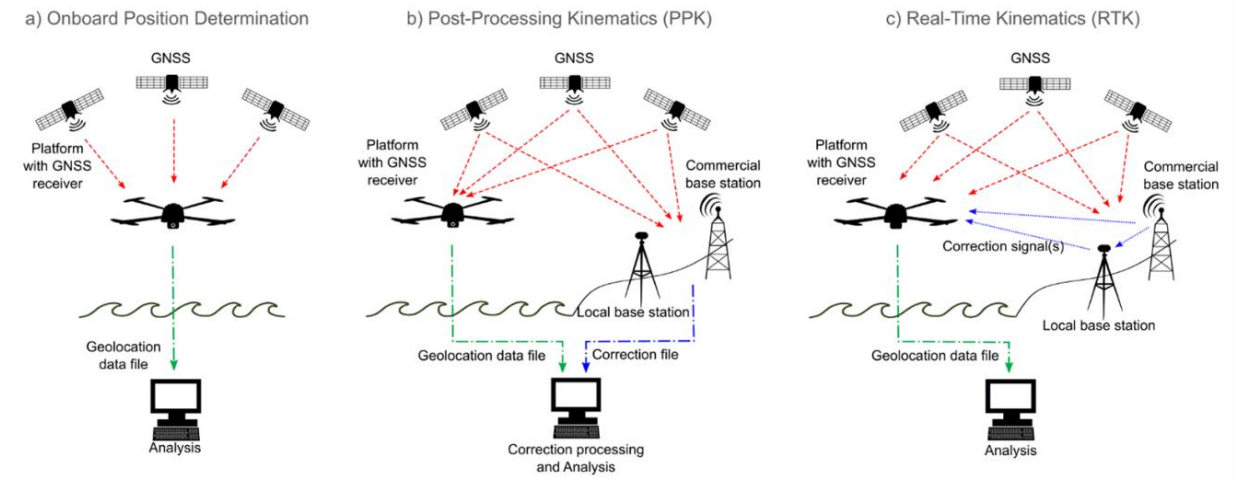

Figure 2.8. The three methods used to acquire geolocational data in RS using UAVs and manned aircraft (labeled "platform" in the figure). (**a**) Platform location is determined using trilateration of three or more satellite signals. (**b**) Platform location is determined by the user applying a correction to the Global Navigation Satellite System (GNSS) receiver-generated location file. The correction file is downloaded from either a local base station operated by the user or from a commercial base station operated by external parties, such as governments. (**c**) Platform location is determined by applying a correction signal from a base station concurrently to data acquisition.

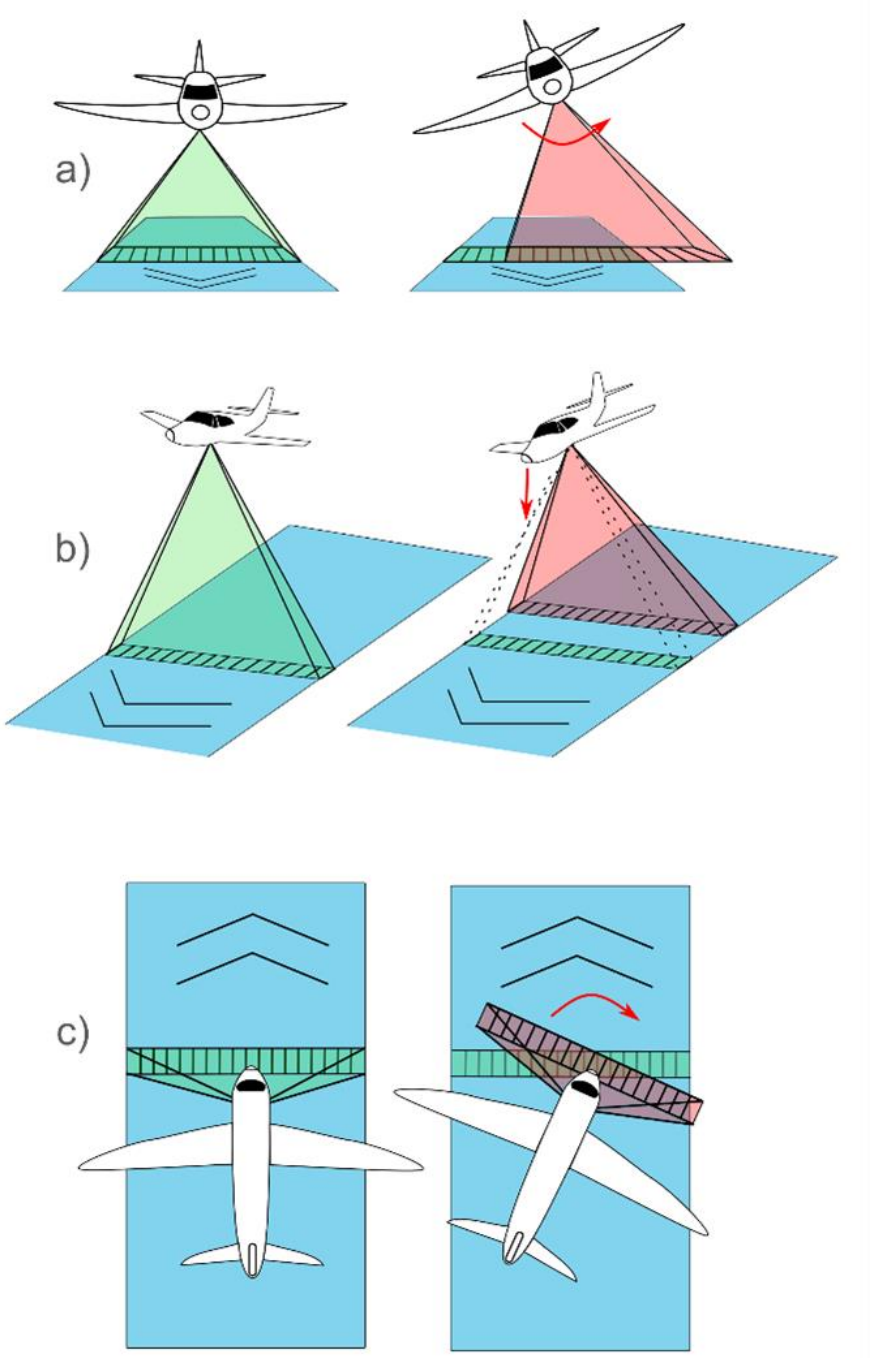

Figure 2.9. The effect of platform attitude on the look direction of a sensor. (**a**) A "rolled" aircraft will cause a sensor to image an area adjacent to the intended flight line. (**b**) A change in platform pitch will cause the sensor to image a portion of the flight line that is not directly below it; rapid changes in pitch may therefore cause duplicate imaging of some targets (downward pitch aiming the sensor backward) or gaps (upward pitch aiming the sensor ahead). (**c**) A change in yaw will angle the view of the sensor so consecutive rows of pixels are not parallel, resulting in gaps and duplication.

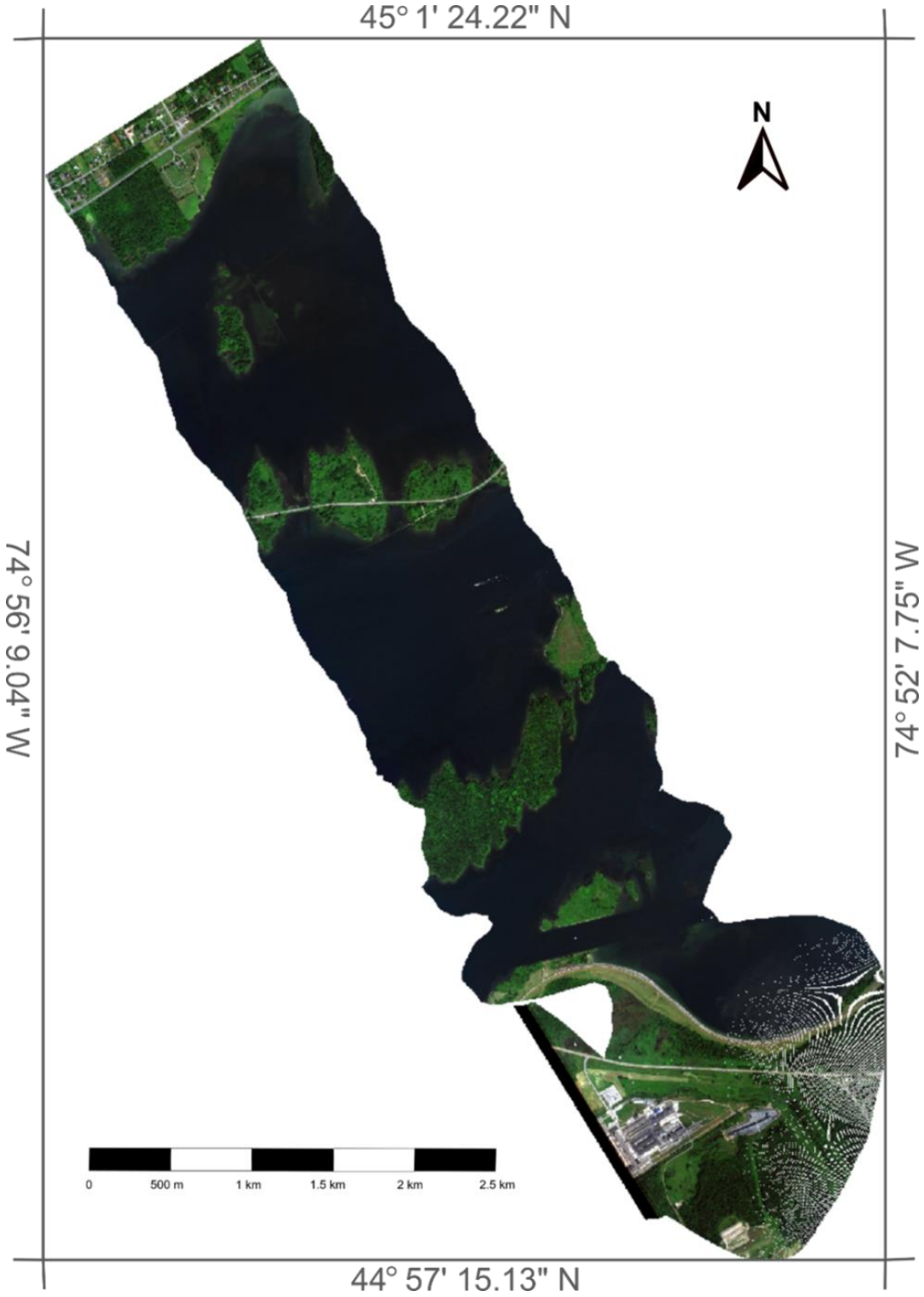

Figure 2.10. An example of imagery collected by a CASI-1500 onboard a manned aircraft acquiring imagery over the Long Sault Parkway, ON, Canada. Imagery was collected by a twin otter aircraft in partnership with the National Research Council of Canada. The NoData artefacts during the turn are portions of the ground over which no pixels are resolved in the geocorrection.

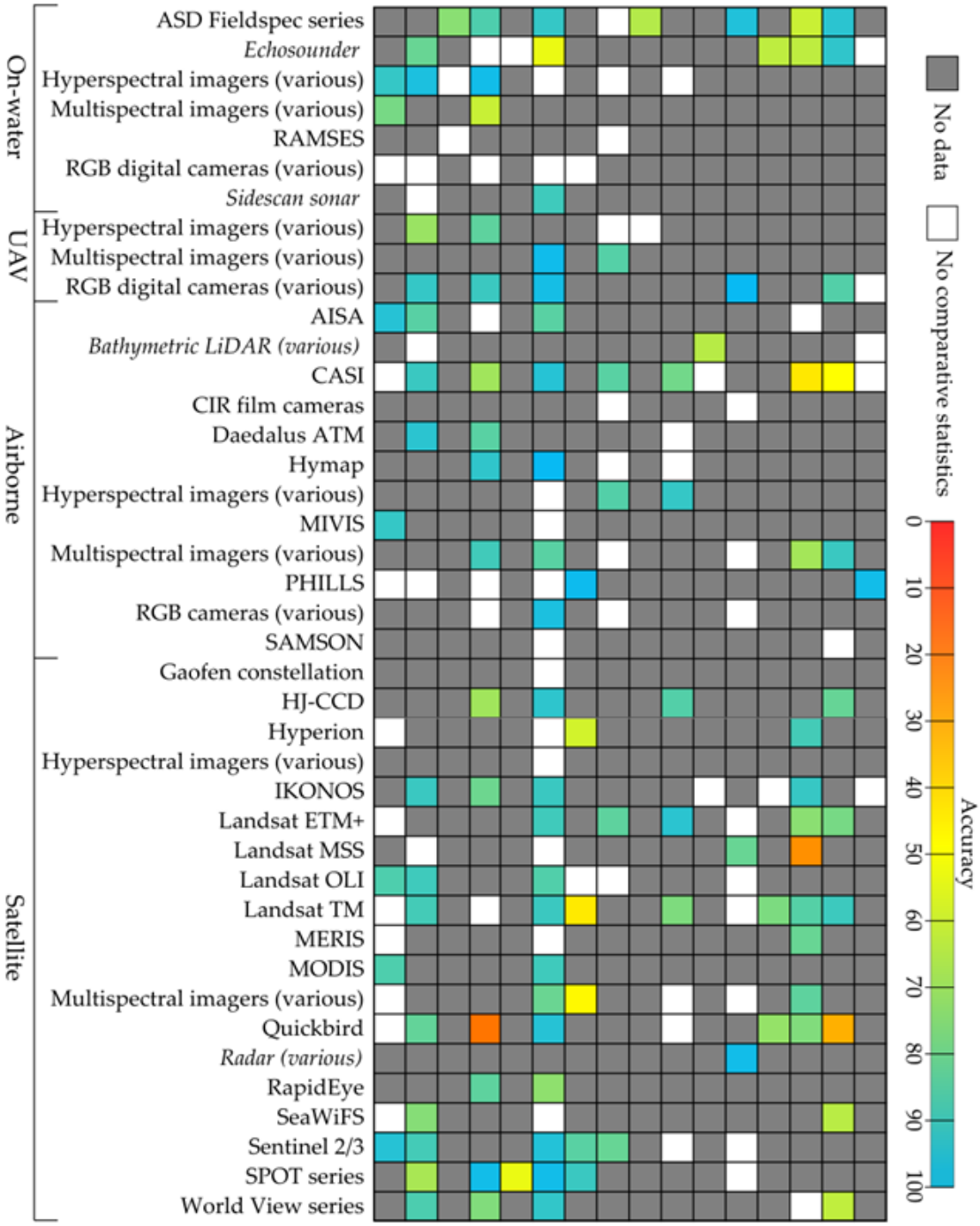
Bathymetry
Biomass
Canopy density
Community composition
Emergent / Floating cover
Faunal community metrics
Functional group
Health
Invasive species detection
Leaf Area Index
SAV cover
SAV height
Species cover
species profiling
Substrate material
Water optical properties
No data
No comparative statistics
Accuracy
0
10
20
30
40
50
60
70
80
90
100
On-water
UAV
Airborne
Satellite
ASD Fieldspec series
Echosounder
Hyperspectral imagers (various)
Multispectral imagers (various)
RAMSES
RGB digital cameras (various)
Sidescan sonar
Hyperspectral imagers (various)
Multispectral imagers (various)
RGB digital cameras (various)
AISA
Bathymetric LiDAR (various)
CASI
CIR film cameras
Daedalus ATM
Hymap
Hyperspectral imagers (various)
MIVIS
Multispectral imagers (various)
PHILLS
RGB cameras (various)
SAMSON
Gaofen constellation
HJ-CCD
Hyperion
Hyperspectral imagers (various)
IKONOS
Landsat ETM+
Landsat MSS
Landsat OLI
Landsat TM
MERIS
MODIS
Multispectral imagers (various)
Quickbird
Radar (various)
RapidEye
SeaWiFS
Sentinel 2/3
SPOT series
World View series

Figure 2.11. An illustration of the extent and accuracy of previous aquatic RS work regarding SAV. The maximum accuracy found (reported as percent overall accuracy or R^2) is depicted for each sensor-application pairing. Colored squares are on a gradient scale from 0 to 100, representing either percent overall accuracy or $R^2 \times 100$. White squares indicate that the sensor-application pair was encountered but no suitable overall accuracy measure was provided. Grey squares indicate that no source employed that sensor-application pairing. The large number of white and grey squares respectively demonstrate the need for consistent accuracy reporting and the huge research gaps to date in aquatic RS. Active sensors are italicized. All sources cited in this text were reviewed in the compilation of the figure, as well as references [225-342].

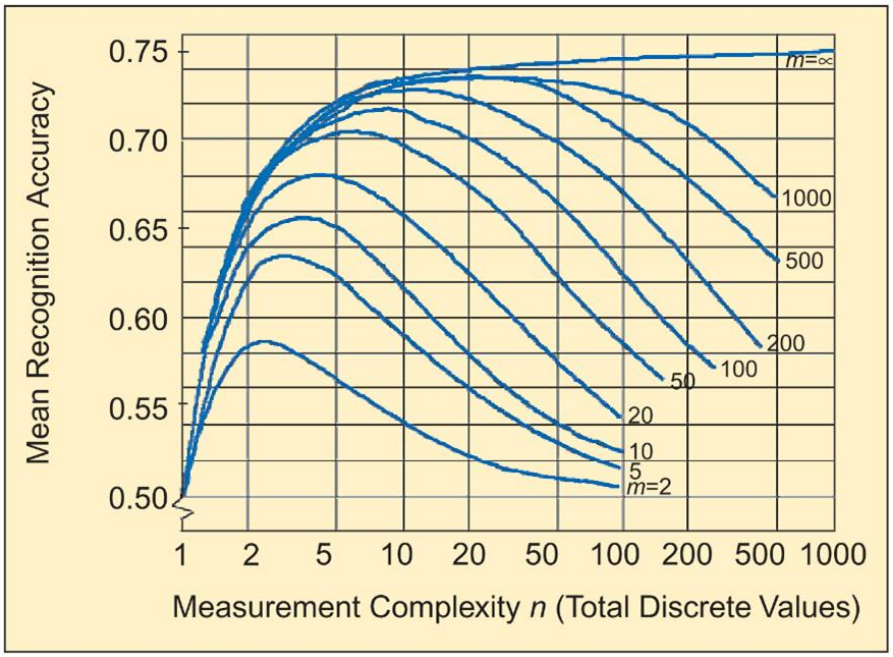

Figure 2.12. The relationship between data complexity, training set size and mean classification accuracy. Complexity is here calculated as the number of bands raised to the exponent of the number of possible DN values per band ($2^{\#\ of\ bits}$). For HSI (and MSI with many bands), huge training sets would be required to obtain adequate classification accuracies if all bands are used. m = training set size. © 2002 IEEE. Reprinted, with permission, from Landgrebe, D. (2002), Hyperspectral image data analysis, IEEE Signal Processing Magazine. [162].

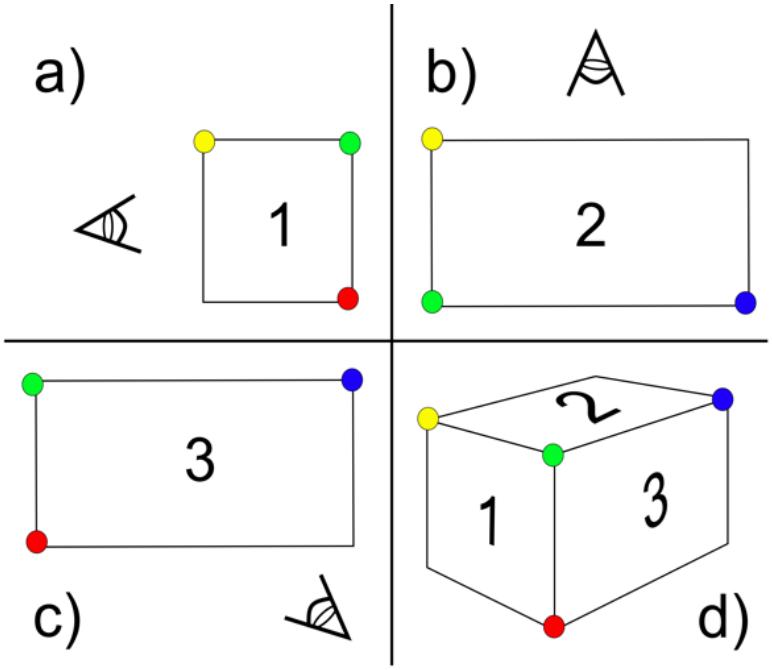

Figure 2.13. A simplified illustration of the principle of Structure-from-Motion Multiview Stereo photogrammetry. Common points at the corners of a rectangular prism seen from various angles are used to reconstruct a three-dimensional representation of the object. (**a**) the side; (**b**) the top; (**c**) the front; (**d**) the reconstructed rectangular prism. In reality, hundreds to thousands of key points (uniquely identified points) per photograph are needed with hundreds to thousands of matches between photographs to reconstruct a surface in 3D.

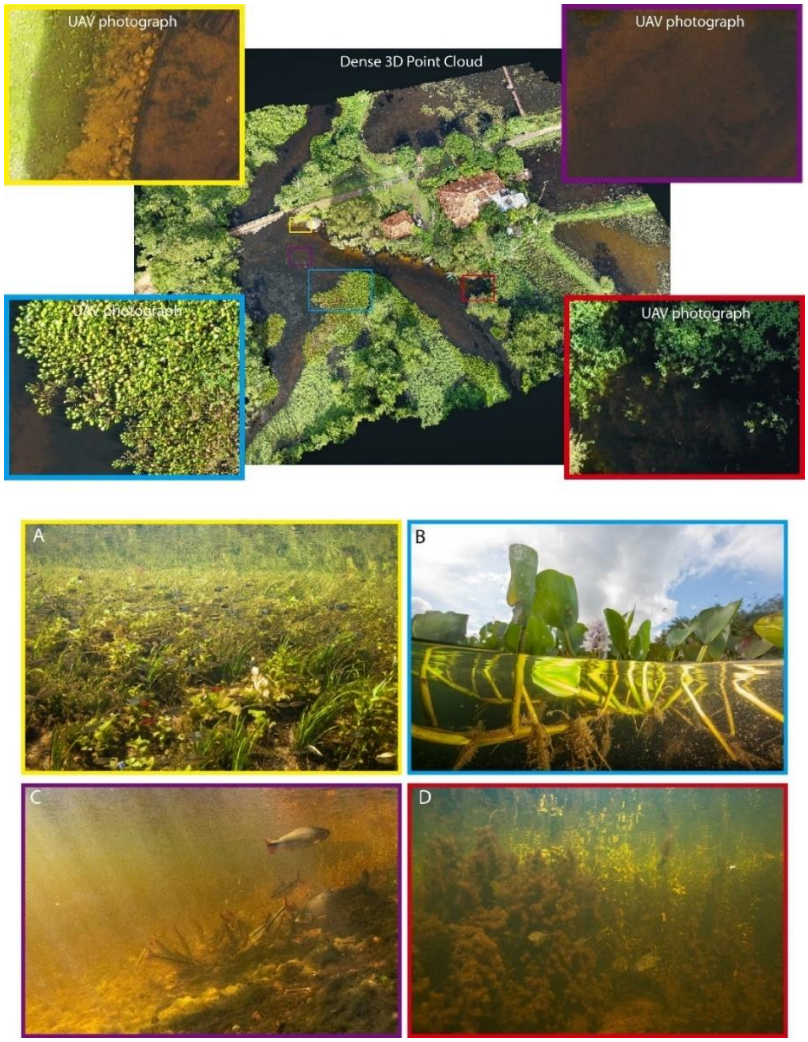

Figure 2.14. Dense 3D point cloud from the Salobra river, Mato Grosso do Sul, Brazil generated through a Structure-from-Motion Multiview Stereo workflow from 768 UAV photographs. Photographs were acquired with a DJI Mavic 2 Pro UAV with an integrated Hasselblad L1D-2C camera. The camera has a 1” sensor (77° field of view) producing an image size of 5472 × 3648 pixels. A median of 67,753 key points were found per photograph with a median of 13,416 matches per photograph. Final ground sampling distance of the model is 1.2 cm. Extensive floating water hyacinth (*Eichhornia crassipes*) can be seen. The interactive point cloud can be accessed at https://bit.ly/waterhyacinth3D . Panel A (yellow) illustrates a shallow (<30 cm) area with several species of SAV which produce a habitat utilized by small characins. Panel B (blue) illustrates floating *E. crassipes* in deep (>2 m) water frequented by giant otters (*Pteronura brasiliensis*) and caimans (*Caiman yacare*). Panel C (purple) is a mid-range depth (1–2 m) with large patches of algae on the substrate. This open water habitat is frequented by larger fish species such as *Prochilodus lineatus*. Panel D (red) shows a bed of *Camboba* sp. in deep water (>2 m). The dense stems provide habitat for species such as *Pygocentrus nattereri* and *Serrasalmus maculatus.*

3. Multi-scale spectral separability of submerged aquatic vegetation species in a freshwater ecosystem

Rowan, G.S.L., Kalacska, M., Inamdar, D., Arroyo-Mora, J.P., Soffer, R. Multi-scale spectral separability of submerged aquatic vegetation species in a freshwater ecosystem. **Frontiers in Environment Science. 2021, 9,** 438. DOI: 10.3389/fenvs.2021.760372

3.1. Context within thesis

The research in this chapter was conducted to fill in some of the foundational knowledge gaps that existed in aquatic remote sensing. It presents original research exploring the spectral properties of a set of thirteen SAV species collected from a freshwater habitat under both idealized and in situ conditions. The theoretical maximum separability between the species is determined, as well as the effects on separability of two sampling conditions (leaf fouling and season) and two project design choices (class coarseness and sensor selection). The same set of species were then mapped in airborne hyperspectral imagery to examine how the theoretical maximum separability translated to practical results. The limitations of the in-situ mapping exercise are discussed to guide future work on planning methodologies and shaping their expectations of possible results. This work illustrates how optical remote sensing could be applied to map SAV across a wide range in scope of various factors including spatial and spectral resolutions, and question specificity. Per the thesis submission guidelines, the text of this chapter is exactly that of the published article.

3.2. Abstract

Optical remote sensing has been suggested as a preferred method for monitoring submerged aquatic vegetation (SAV), a critical component of freshwater ecosystems that is facing increasing pressures due to climate change and human disturbance. However, due to the limited prior application of remote sensing to mapping freshwater vegetation, major foundational knowledge gaps remain, specifically in terms of the specificity of the targets and the scales at which they can be monitored. The spectral separability of SAV from the St. Lawrence River, Ontario, Canada, was therefore examined at the leaf level (i.e., spectroradiometer) as well as at coarser spectral resolutions simulating airborne and satellite sensors commonly used in the SAV mapping literature. On a Leave-one-out Nearest Neighbor criterion (LNN) scale of values from 0 (inseparable) to 1 (entirely separable), an LNN criterion value between 0.82 (separating amongst

all species) and 1 (separating between vegetation and non-vegetation) was achieved for samples collected in the peak-growing season from the leaf level spectroradiometer data. In contrast, samples from the late-growing season and those resampled to coarser spectral resolutions were less separable (e.g., inter-specific LNN reduction of 0.25 in late-growing season samples as compared to the peak-growing season, and of 0.28 after resampling to the spectral response of Landsat TM5). The same SAV species were also mapped from actual airborne hyperspectral imagery using target detection analyses to illustrate how theoretical fine-scale separability translates to an in situ, moderate-spatial scale application. Novel radiometric correction, georeferencing, and water column compensation methods were applied to optimize the imagery analyzed. The SAV was generally well detected (overall recall of 88% and 94% detecting individual vegetation classes and vegetation/non-vegetation, respectively). In comparison, underwater photographs manually interpreted by a group of experts (i.e., a conventional SAV survey method) tended to be more effective than target detection at identifying individual classes, though responses varied substantially. These findings demonstrated that hyperspectral remote sensing is a viable alternative to conventional methods for identifying SAV at the leaf level and for monitoring at larger spatial scales of interest to ecosystem managers and aquatic researchers.

Keywords

hyperspectral remote sensing; freshwater; *Myriophyllum spicatum*; target detection; Depth Invariant Index; St. Lawrence River.

3.3. Introduction

Submerged aquatic vegetation (SAV) is vital to the health of aquatic ecosystems. It provides habitat and food for fauna, stabilizes sediments, modifies flow regimes, and improves water quality [5,12,15]. SAV is also facing severe threats in the forms of warming waters, increased water levels, invasive species, and human modification to water ways [5,13,19]. Monitoring is therefore critical to assessing the health of SAV communities, their population dynamics, and changes in their distributions due to these pressures as well as to evaluating the efficacy of ecological management projects [2,343]. As optical remote sensing is widely effective in terrestrial vegetation monitoring in many applications including biodiversity assessment, forestry, agriculture, etc. (e.g., [344-346], there is a desire to expand the use of the discipline to

underwater ecosystems. Optical remote sensing has been suggested as a preferred method for large scale SAV monitoring [2,4-6] and has been effective in detecting SAV communities at local and regional scales [16,178,191,204]. Past SAV monitoring applications have however largely focused on seagrasses and marine algae growing in clear coastal waters. Further exploration into freshwater plant species is therefore needed to determine if optical remote sensing is suited to freshwater SAV monitoring.

Detecting or identifying a target through optical remote sensing relies on the principle of spectroscopy whereby an unknown material is labeled according to the similarities in its spectral response to those of known reference materials or spectra [140]. This method requires that all materials being labeled are represented in the reference set and the spectral signatures of these materials as recorded by the sensor are sufficiently distinct to be separable. The spectral separability of terrestrial vegetation has been thoroughly evaluated (e.g., [347-349]) and has paved the way for very specific applications such as precision agriculture and forestry. While there is a small body of existing work examining the spectral separability of SAV (here including both plants and macroalgae due to their functional and spectral similarities), it does not sufficiently address freshwaters. For example, Fyfe (2003) examined three species of seagrasses across different habitats and water conditions using a spectroradiometer and found them to be separable amongst the species as well as separable within the same species depending on sampling location (i.e., population level separability). McIlwaine et al. (2019) separated between eight species of macroalgae. Both studies however exclusively treated marine SAV. A study conducted by Brooks et al. (2019) applied multiscale spectroradiometer data and multispectral imagery to investigate freshwater vegetation, but separated only amongst individual samples, not classes, thus limiting the applicability of the results to large scale SAV mapping. Thus, there remains a need to establish spectral separability amongst freshwater SAV before widescale mapping and monitoring efforts are pursued.

At the leaf level, the spectral signatures of vegetation are determined by the relative concentrations of their pigments and by their cellular structure [18,57]. As green vegetation shares a common set of pigments, the spectra of various green vegetation species tend to be similarly shaped: a notable reflectance peak at 550 nm represents chlorophyll-a (Chl-a) reflecting green light, troughs around 445 nm and 660 nm where blue and red light are absorbed, respectively, and a steep increase in reflectance in the near infrared (NIR) where multiple refractions produce

high apparent reflectance [57]. At the canopy level, the combination of illumination conditions and plant structure (e.g., leaf orientation relative to incident sunlight, self-shading, etc.), and intra-individual spectral diversity affect the recorded at-sensor reflectance [205,350]. SAV is, however, located beneath a water column, even if that water column is thin (i.e., < 0.5 m). All light reaching submerged leaves is thus affected by the water column which contains not only water but also suspended and dissolved constituents like phytoplankton or salts. The combined effect is that wavelengths of light below 450 nm are strongly scattered, NIR wavelengths are strongly absorbed, and the wavelengths in between – the visible region (VIS) – are inconsistently affected depending on the water column constituents and depth [50]. Depending on the state of the surface (e.g. roughness) and the viewing geometry of the sensors, surface reflectance effects such as glint may further confound analysis and need to be compensated for [351]. Because both water and water column constituents confound the signal from aquatic targets, optical remote sensing for SAV studies is limited to applications in shallow waters of clear to moderate water type [351]. These waters are highly transparent and demonstrate minimal interference from water column constituents [352]. The spectral information reasonably expected to be available for spectroscopy and mapping from *in situ* measurements of SAV, even in this subset of water types, is therefore limited to the visible portion of the spectrum and, in very shallow waters, the very short NIR. Considering that the NIR region can provide spectral information that is useful in classification [353], the truncation of spectral information may hinder the classification of SAV.

In addition to the water column, SAV is often covered by a thin biofilm, a layer of debris, bacteria, and epibionts, whose thickness and composition vary due to flow regime, disturbances, and water quality. This leaf fouling can thus not only obscure the signal originating from a target but also contribute its own [205]. As leaf pigment contents change throughout growth, the spectral signature of an individual plant may thus change substantially according to the stage of growth in which it is measured. Past work with estuarian SAV has suggested that measurements taken at the end of the growing season produce the most accurate classification results [71]. This has, however, not yet been tested in freshwater SAV. Understanding how sampling conditions such as presence of fouling and plant maturity affect their spectral response, and thereby the spectral separability of the SAV, is thus essential if freshwater SAV mapping efforts are to succeed.

To be useful for *in situ* monitoring campaigns, an examination of SAV spectral separability would thus need to not only establish a sufficient leaf-level spectral diversity, but also consider how this separability may be affected by the experimental conditions of larger-scale *in situ* applications (e.g., airborne and satellite based). The spectral resolution required to separate between SAV operational taxonomic units (OTUs), the minimum size of SAV stands that can be detected, the effect of biophysical vegetation conditions on separability, and how narrowly vegetation OTUs can be defined while remaining spectrally separable have all yet to be thoroughly examined. Addressing each of these knowledge gaps will inform what kind of research questions optical remote sensing can be used to answer in shallow, clear to moderate optical water types such as the freshwaters examined as well as many brackish and coastal waters of similar depth. In this study, our overall objective was to provide a foundational understanding of freshwater SAV spectral separability at different spectral and spatial scales. At the finest scale, the separability of different SAV species was evaluated at the leaf level and how this separability translates to both resampled airborne hyperspectral and multispectral satellite-based sensors commonly used in SAV studies was assessed. Both the full spectral resolution leaf-level and resampled air/spaceborne spectra were assessed in terms of OTUs (e.g., species, genus, kingdom), leaf biofouling and sampling season. Lastly, we conducted a target detection analysis with an actual airborne hyperspectral image (144 bands from 400-1000 nm), to explore the extent to which SAV can be mapped and discuss the implications of image characteristics (e.g., spatial resolution, image pre-processing) on the use of these data for operational SAV mapping.

3.4. Methods

3.4.1. Site description

The St Lawrence River connects the North American Great Lakes to the Northern Atlantic, with a large stretch forming the Canada-United States border. It is a major navigational channel for commercial and leisure traffic (nearly 15,000 vessels passed through the St. Lawrence Seaway in 2019 [354]) and is especially vulnerable to human disturbances and ecological invasions [355,356]. The St. Lawrence is also the subject of many restoration and ecological management programs from the local to international scales [357,358]. The study site was a shallow bay along the St. Lawrence to the west of Phillpott's Island, in the Long Sault

Parkway recreation area (Figure 3.1). The region surrounding the Parkway is primarily zoned for agriculture and residential space, though there is some industrial activity in the nearby towns [359]. The area had previously been the small town of Moulinette, Ontario, before being flooded in 1958 during construction of the Moses-Saunders hydroelectric dam [360]. Infrastructural remnants provided reference points during surveying and in imagery (Supplementary Figure 3.1). The sampling area was restricted to depths of less than 1.5 m due to strong currents in deeper waters and covered an area of approximately 1.85 ha. Vegetation found at the site includes various *Potamogeton* species, *Chara* sp., *Sagittaria graminea, Vallisnaria americana,* and the invasive *Myriophyllum spicatum* (Figure 3.2). Where not cpvered by vegetation or asphalt, the bottome varied between large rocks and gravel along the shoreline to a fine silt in the middle of the bay.

3.4.2 Multiscale approach

Figure 3.3 shows the different levels at which SAV was assessed including leaf-level spectroscopy (i.e., finest spectral resolution), resampled air/spaceborne sensors, and actual airborne hyperspectral imagery. The following sections thoroughly describe the data acquisition, processing and analysis employed in this study. A flowchart of the analytical steps is shown in Figure 3.4.

3.4.3 Submerged Aquatic Vegetation sampling

3.4.3.1 Spectralon panel measurements

A 99% reflective Spectralon (Labsphere, North Sutton, New Hampshire) panel was submerged to different depths to determine the absorptive properties of the water column in relation to a separate 99% reflective Spectralon panel which remained on dry land. Spectra of the panel were collected using an Analytical Spectral Devices (ASD) Fieldspec 3 spectroradiometer (Malvern Panalytical, Boulder Colorado), referred to hereafter as ‘ASD’, at depths from ~ 1 mm to 115 cm at 5 cm intervals (Supplementary Figure 3.1). This instrument measures reflected radiation in the 350-2500 nm range, has a spectral resolution of 3 nm and a sampling interval of 1.4 nm in the visible (VIS) and near infrared (NIR) regions and a spectral resolution of 10 nm with a sampling interval of 2 nm in the shortwave infrared (SWIR) (ASD, Inc., 2010). Measurements were repeated at three locations within the bay for each depth and then averaged following the calculation of the estimated absolute reflectance (R_{abs}) according to [113,120].

3.4.3.2 Plant sample collection

Plants were collected twice: on August 5th, 2019, and on August 12th 2020, with water temperatures of 21°C and 23.5°C, respectively. The 2020 flora was substantially more mature than the previous year, likely due to differences in springtime flooding (severe flooding in 2019 potentially delayed the growing season). Many plants were flowering in 2020 and leaves were senescing. The 2019 and 2020 samples were therefore designated as peak-growing season and late-growing season, respectively. The study area was informally surveyed by a snorkeler to identify as many species as possible and approximate their relative abundance; the plants were harvested according to those estimates. Whenever possible, plants of the same species were collected from different areas and depths to maximize intra-specific variability. Sampling in 2020 was additionally selective to find plants with healthy leaves. Two silt samples were collected in 2019. Samples were labeled, stored in river water, and transported to a dark room.

The taxonomy of each sample was determined according to [361]. In the cases of uncertainty at the species level, the sample was labelled to the genus level. Supplementary Table 3.1 presents an overview of the samples collected in both years and the coded nomenclature used throughout this work.

3.4.3 Microscopy

To supplement the leaf level spectral measurements (see section 3.4.6.1) because vegetation's NIR reflectance is strongly influenced by leaf structure [362], microscopy photographs were collected of each species sampled in 2020 to qualitatively assess the structural diversity present in the SAV being studied. Images were acquired at the McGill University Multi-Scale Imaging Facility, Sainte-Anne-de-Bellevue, Québec, Canada. Plants were kept in water until being prepared for imaging, ensuring their freshness; they were neither preserved nor stained before imaging. Thin cross sections were cut across the center of each leaf, ensuring all internal structures (i.e., mesophyll, lacunae, vascular bundles, etc.) were included in the images. Cross sections were placed in a small amount of water to avoid desiccation. Photographs were taken using an AxioCam MRm Rev.2. mounted on a Zeiss AxioImager Z1 microscope equipped with an LED light and a halogen lamp for illumination. Magnifications between x4 and x40 were applied depending on the subject.

3.4.4 SAV ground truth data collection

Ground truth points recording the locations of different SAV species in the bay were gathered to provide input and validation data for analysis of the airborne imagery. Points recording locations of exposed silt and cement and asphalt (i.e., from a submerged road and building foundations) without vegetation cover were also collected. These points were collected in two ways: recorded observations at each location of the 2019 plant sampling, and underwater video footage of four 20 m transects each with thirty-one location markers (Supplementary Figure 3.1). The locations sampled and the placement of the transects were stratified to include the full variability in vegetation cover present. Sampling points were included for use in imagery analysis if they were observed to have homogeneous cover of one of the operational taxonomic units (OTUs) considered over at least ~1 m2. Video footage of each transect was collected by tracing over the length of the transect in a square wave pattern with a Go Pro hero 5 held nadir at the surface of the water. Frames of each transect marker (124 in total) were extracted from this video and assessed to determine ground cover. Transect markers were assigned to a given OTU if the frame containing the marker was covered at least 40% by a single class; points could thus be assigned to up to two vegetation classes: unassigned points were discarded; points assigned to a single class were divided into training and validation sets; points assigned to two classes were used in validation but not training. Sampling locations and transect marker placements were recorded using a Reach RS+ (EMLID, St. Petersburg, Russia) Global Navigation Satellite System (GNSS) receiver unit according to [363], with incoming Network Transport of RTCM via Internet Protocol (NTRIP) corrections from a SmartNet North America base station located ~25 km away in Morrisburg, Ontario.

3.4.5 High spatial resolution orthomosaic

To supplement the input and validation data available for analysis from the ground truth points, a high spatial resolution RGB orthomosaic was produced from which additional training and validation data could be extracted. A DJI Inspire 2 Remotely Piloted Aircraft System (RPAS) with an X5S camera (micro 4/3 sensor) and a DJI MFT 15 mm/1.7 aspherical lens (72° diagonal field of view) was used to acquire photographs of the bay from an altitude of 40 m AGL. A total of 703 photographs were acquired in a double grid pattern with 85% front and side overlaps. The 20.8 MP .jpg photographs were 5,280 pixels wide by 3,956 pixels tall. Pix4D Mapper v4.7.1 was used to generate an orthomosaic following the Structure-from-Motion

MultiView Stereo workflow described in [193]. Twenty-three ground control points (GCPs) consisting of submerged targets placed throughout the bay were used to improve the positional accuracy of the orthomosaic during processing with Pix4D Mapper since the geotags of the Inspire 2 are neither real-time kinematic nor post-processing kinematic corrected [103]. The coordinates of the GCPs were measured with the Reach RS + GNSS receiver as described above. Two hundred and forty points over areas of at least 1 m2 of homogenous ground cover were manually identified from the orthomosaic. As not all species sampled at the site grow in canopy-forming stands and some stands were homogenous by growth type rather than species, the points were limited to the following 7 classes: ribbon-like leaves (*Sagittaria graminea* and *Vallisneria americana*), *Potamogeton richardsonii*, metaphyton, *Chara* sp., *Potamogeton* sp., paved asphalt, and other non-vegetation (silt and rock).

3.4.6 Leaf-level spectra

3.4.6.1. Leaf-level spectral measurements

The leaf level spectra of each sample were collected in a darkroom through a modified contact measurement procedure using the ASD and a low intensity halogen contact probe. The probe ensures a constant viewing and illumination geometry with a 1 cm diameter spot. The samples were placed in a matte black dish with a ~1-2 mm layer of water covering the leaves to avoid desiccation. The probe was placed close enough for the lens to touch the thin water layer over the leaves and a spectrum was collected over each leaf or leaf segment as there was often visible variability present within individual plants and leaves (Supplementary Table 3.1). The samples were measured both in their natural fouled state as well as after rinsing to remove the fouling. The 2019 samples of metaphyton, *Potamogeton crispus*, and *Nymphaea odorata* were not re-measured following rinsing due to sample degradation. The reflectance ratio of each sample acquired by the ASD was converted to R_{abs} following Elmer et al. (2020). Each sample was pressed and kept as records locally to be deposited within a herbarium at a later date. The leaf spectra were then sorted into 7 datasets in each year according to the OTUs outlined in Supplementary Table 3.2.

3.4.6.2 Resampled airborne HSI and multi-spectral satellite SAV spectra

Both airborne hyperspectral and multispectral satellite imagery have a lower spectral resolution and are thus incomparable to that of the leaf level spectra collected under laboratory

conditions with a spectroradiometer. It was therefore important to analyze the leaf level spectra resampled to the spectral response functions of the air/spaceborne sensors simulating how the signatures would be recorded by these coarser resolution sensors. The leaf spectra were resampled to the relative spectral response (RSR) functions of six former or current multispectral satellite sensors and an airborne hyperspectral imager, the Compact Airborne Spectrographic Imager-1500 (CASI) (Figure 3.5, Supplementary Table 3.3). See section 2.7.1 for a description of the CASI. The resampled spectra then underwent the subsequent analysis described below alongside the original ASD spectra to compare results across sensors.

3.4.6.3 Feature selection and Classification

The leaf level spectra underwent dimension reduction and classification, steps that are often also applied to imagery, to determine the theoretical best separability and classification accuracy achievable for this set of SAV species. All leaf spectra were subset to the 400 – 950 nm range due to the artificial illumination causing substantial noise in shorter wavelengths, and the near-complete absorption of longer wavelengths by even a very thin water column, as determined from measurements of the submerged Spectralon panel (see section 3.5.1). A forward feature selection (FFS) with a nearest neighbour criterion [364] was implemented in MATLAB R2020a (Mathworks, Natick Massachusetts) using the PRTools5 toolbox [365] to determine the optimal bandset to distinguish between the various OTUs. After feature selection, each dataset, reduced to the optimal bands was divided 60/40 into training and testing samples. After an initial trial run with all thirty-four classifiers in the PRTools toolbox on the peak-growing season, species level of both fouled and unfouled samples (a19 dataset; Supplementary Table 3.2), all classifiers that resulted in a validation accuracy ≥80% were retained and applied to all datasets (see section 3.5.2.5).

3.4.7 Airborne hyperspectral imagery

3.4.7.1 Image acquisition and processing

A 144-band airborne hyperspectral image (HSI) of the study area (Figure 3.1) was acquired with the CASI-1500 sensor (ITRES Ltd, Calgary, AB) on July 26th, 2019, by the National Research Council of Canada's Flight Research Laboratory (NRC-FRL) (acquisition parameters are provided in Supplementary Table 3.4). The image was preprocessed to units of radiance (uW/cm^2/sr/nm) using lab-derived calibration parameters applied using standard

processing modules as provided by the manufacturer [120]. Because surface water results in a weak signal, conventional radiometric correction procedures developed for imagery of terrestrial environments result in radiance values that are erroneously low and often negative at wavelengths below 450 nm (Soffer et al. 2021). As such, a two-part, non-linear In-Flight Radiometric Refinement (IFRR) methodology following Soffer et al. (2021) specifically developed for pixel spectral responses equivalent to surface reflectance levels < 3% was applied prior to atmospheric correction.

The IFRR refined radiance image was then atmospherically corrected with ATCOR4 v7.3.0. to generate surface reflectance (Figure 3.4, Supplementary Table 3.4). To compensate for the effect of the water column, the Depth Invariant Index (DII) [141,144] was calculated for all band pairs including only wavelengths below 950 nm (Inamdar et al. 2021, submitted). A maximum correlation coefficient threshold of 0.9 was applied to reduce the dimensionality of the DII data from 5,565 (all pairs) to 124. Following the methodology described in [366,367], the DII bands were geocorrected without raster resampling to generate a hyperspectral point cloud which assigns 3D spatial coordinates to each image spectrum without introducing the pixel duplications and loss that result from conventional nearest neighbour raster resampling. Next, in CloudCompare v2.12, the point cloud was subset to the study site and was rasterized to 25 cm pixels (empty cells were not interpolated over) to allow data visualization of the point cloud in raster data format without introducing pixel loss or duplication; NoData values were given to empty cells. In ENVI v5.5.3 (Harris Geospatial Solutions, Inc., Broomfield, CO), all NoData pixels were masked out. Ground truth points (section 3.4.4) and points extracted from the orthomosaic (section 3.4.5) were imported into ENVI and the nearest DII data pixel to each was manually selected and assigned the point's label, sometimes resulting in a single data pixel being assigned multiple ground truth point labels.

3.4.7.2 Target Detection

Target detection was used to identify SAV classes in the airborne HSI as not all materials in the HSI were known and the classes covered relatively small areas. A target detection was performed in ENVI on the 124 band DII image for each of the classes of interest (i.e., five canopy-forming vegetation types, the paved asphalt road, silt/rock, all vegetation combined, and a non-vegetation class). The selected pixels corresponding to the ground truth and orthomosaic points were divided 60/40 into input (target and non-target) spectra and validation points. The

Adaptive Coherence Estimator (ACE) algorithm [368] (Equation 1) was used to create rule images for each class with all other classes input as non-target spectra. Assignment thresholds were then selected to maximize the detection of known class extent while minimizing false positive detections (Supplementary Table 3.5). ACE was chosen for its ability to detect sub-pixel targets as was common at the field site due to the small areal extent of most SAV stands and is calculated as follows:

$$ACE = \frac{(S^T \Sigma_b^{-1} x)^2}{(S^T \Sigma_b^{-1} S)(x^T \Sigma_b^{-1} x)}$$

where S^T is the mean input spectrum of the target class after undergoing a matrix transposition, x is the pixel spectrum under consideration and b is the covariance matrix of the classes identified as non-target background [187].

3.4.7.3 Accuracy assessment

To account for the spatial uncertainty in both the reported locations of the ground truth data and the geocorrection of the CASI imagery, buffers were created around all detected pixels and validation points according to the spatial uncertainty of each data set. For the validation points recorded *in situ*, the buffer diameter was calculated as the sum of the manufacturer reported accuracy for NTRIP baselines >10 km (i.e., 1 m) and the average standard deviation of the points reported by the Reach RS+ unit [369]. For the pixels output from the target detection, the uncertainty buffer considered the reported spatial accuracy of the CASI imagery (2.25 m) [369] and the effective pixel resolution, the area corresponding to the full-width half-max of the CASI's point spread function [121] (i.e., 1.038 m in the across-track and 0.978 m in the along-track) as determined following [366]. The sum of the spatial accuracy and the effective pixel resolution resulted in elliptical uncertainty boundaries where materials contributing to each pixel's recorded signal were located. Validation points were deemed to have been correctly detected if the points' and the pixels' buffers overlapped.

3.4.8 Expert visual interpretation

To assess the relative utility of employing remote sensing methods to aquatic vegetation monitoring, the validation accuracy of the target detections performed on the imagery was compared to the accuracy a team of researchers could achieve by manually inspecting the same

vegetation OTUs. Field assistants that had participated in this fieldwork, and select external researchers with experience in botany and/or remote sensing, interpreted 135 pictures from the field site consisting of field photos and frames extracted from the underwater video transects. All pictures were color corrected to improve their interpretability. The pictures were made available online similar to the implementation described by [370]. The online platform chosen to host the pictures and record the selections was SurveyLegend (surveylegend.com). The content consisted of three sections: first, examples of vegetation were presented; second, expert interpreters identified photos with at least 40% of the frame covered by a specified vegetation type; and third, expert interpreters selected all photos with any amount of a specified vegetation type. It is acknowledged that this method did not account for user expertise or the choice of photos included; it is presented strictly as a coarse estimate of manual detection accuracy.

3.5 Results

3.5.1 Submerged panel measurements – determination of usable wavelength range

The average R_{abs} measurements of the Spectralon panel submerged across depths up to 115 cm are shown in Figure 3.6. In general, as expected, the reflected signal decreases in amplitude with increasing depth (Figure 3.6a). The reflectance of the panel in the VIS wavelengths (450 – 650 nm) does not however demonstrate consistent exponential decay across all depths; at certain wavelengths (e.g., 440 nm), increased reflectance values at lower depths were recorded (Figure 3.6b). Beyond 900 nm, there is strong absorption by the water column with reflectance < 0.06 for any depth of 5 cm or more. For all depths of more than 15 cm, reflectance is < 0.02 at wavelengths greater than 950 nm, indicating that spectral information from almost all aquatic targets would be limited to wavelengths shorter than 950 nm.

3.5.2 Leaf spectroscopy

3.5.2.1 Impact of biofouling and season

The average laboratory spectra for each leaf-level OTU for each year (Supplementary Table 3.2) are shown in Figure 3.7. While all plant and algae spectra have the expected spectral signature of green vegetation [57] the amplitude is low, especially in the NIR (< 0.27). Fouling had only a minimal effect on the spectra (Supplementary Figure 3.2a, b, Supplementary Figure 3.3a). Averaged across all species, removing the fouling produced a maximum difference in the reflectance amplitude of 3.9% at 921 nm in the peak growing season and of 1.1% at 900 nm in

the late season, with the average difference ranging from -0.1% to 3.9% and from -1.1% to 0.5%, respectively. Seasonality had a more varied effect on mean spectra across species (Supplementary Figure 3.2c, d, Supplementary Figure 3.3c, d). The maximum difference in reflectance between peak-growing season and late-growing season samples, averaged across all species, was 4.5% at 921 nm in fouled samples and 1.3% at 909 nm in unfouled samples, with the average differences between seasons ranging from -1.6% to 4.5% and -1% to 1.3%, respectively.

3.5.2.2 Forward feature selection across OTUs

The forward feature selection produced ranked lists of features (i.e., bands) according to the marginal contributions of each wavelength to maximum theoretical separability (Leave-one-out Nearest Neighbor criterion (LNN) for each dataset for each sensor (Supplemental Figures 3.4 and 3.5, Tables 3.1, 3.2). In both seasons and across all OTUs, features in the VIS tended to be higher ranked than those in the NIR (Supplementary Figure 3.4). In the peak-growing season samples, five of the seven OTUs' most important contributors to separability were near the Chl-a reflectance peak (~550 nm), with the other two top ranked features located in the total pigment absorbance peak (~450 nm) and the red edge region (~700 nm). In the late season however, five out of seven OTUs' top-ranked feature was located in the NIR region; the majority of subsequent highly ranked wavelengths remained in the VIS. In every case, most of the maximum separability between classes can be attributed to just a few of the top ranked wavelengths (Supplementary Figure 3.5). Ninety five percent of the total separability between classes could be achieved with at most 24 of the top ranked bands (out of a maximum 551 bands). Increasing the separability from 95% to the maximum value could require > 200 additional input bands (Table 3.1).

The original laboratory spectra produced the highest separability values in all cases (Table 3.2). On a scale from 0 (classes entirely inseparable) to 1 (classes perfectly separable), the peak-growing season samples had LNN criterion values ranging from 0.8 (all samples, grouped by species) to 1 (vegetation/non-vegetation) depending on the coarseness of the OTU definition. The late-growing season samples had LNN criterion values between 0.55 (unfouled and all samples, grouped by species) and 1 (vegetation/non-vegetation). While separation between kingdoms and between vegetation/non-vegetation were equally high (0.98 and 1, respectively) in both years, the more granular OTUs were found to be sensitive to the effect of seasonality; peak-

growing season samples were more separable than late-growing season samples (e.g., LNN values 0.80 and 0.55 for the species level OTU from the peak-growing season and late-growing season samples, respectively). A slight improvement in separability (from 0.82 to 0.84 and from 0.55 to 0.56 for peak-growing season and late-growing season samples, respectively) was seen in the fouled samples as compared to the unfouled samples, in both years (Table 3.2).

3.5.2.3 Leaf cross sections

Cross-section photographs of the leaves taken via microscope revealed common patterns in leaf structure, largely divided between the plants with thin flat leaves (*E. canadensis, P. richardsonii, P. robbinsii, S. graminea, V. americana*) and those with compound leaflets (*C. demersum, N. flexilis, M. spicatum*) or exclusively stems (*E. acicularis*) (Supplementary Figure 3.6). In all plants, large lacunae were visible (or developing) with a single layer of large mesophyll cells dividing them. There were no disaggregated intra-cellular air spaces as is common in the spongy mesophyll of terrestrial, emergent, and floating vegetation (Supplementary Figure 3.6g), nor was there columnar mesophyll in any submerged leaves. Thin flat leaves tended to only be a few cells thick except for in proximity to a vascular bundle where the cells were smaller and more densely packed. Leaflets and stems were roughly circular with up to four large central lacunae and radial thicknesses of only a few cells. *Chara* sp., a macroalgae, was distinct from the plants in lacking all interior structure.

3.5.2.4 Resampled airborne HSI and multispectral satellite spectral separability

Resampling the spectra to the RSRs of space- and air-borne sensors (Figure 3.5) clearly demonstrates the dependence of separability on spectral resolution and number of bands (Table 3.2). For example, spectra resampled to the RSR of Landsat TM5 resulted in LNN separability on the fouled, peak-growing season species level OTU of 0.56, compared to 0.84 from the original ASD spectra. This pattern of increasing separability with increasing spectral resolution and number of bands was consistent across resampled datasets (Table 3.2). The theoretical LNN separability from all RSR resampled spectra was found to be adequately (> 0.70) high to separate spectra between kingdoms and between vegetation/non-vegetation OTUs in both years. Spectra resampled to the RSRs of Sentinel-2, MODIS and the CASI (airborne hyperspectral) produced acceptably high separability values for the species level OTUs from the peak-growing season fouled and unfouled samples (i.e., 0.73 and 0.70, 0.73 and 0.70, and 0.81 and 0.76, respectively),

as well as for all genus level OTUs from the peak-growing season samples (0.70, 0.70, and 0.77, respectively) or the ad hoc OTU (0.75, 0.74, and 0.82, respectively) (Table 3.2).

3.5.2.5 Leaf level and resampled air/spaceborne spectral classification

Classification accuracy (at the species level OTU from the peak-growing season with both fouled and unfouled spectra) with the FDSC, NUSVC, and RBSVC classifiers was > 80% (Supplementary Table 3.1). Classification accuracies across OTUs for each of those three classifiers are presented in Table 3.3. Although the NUSVC performed well on the leaf level spectroradiometer data, it resulted in 26% and 23% lower accuracy at the species level than FDSC and RBSVC, respectively. The accuracies of the FDSC and RBSVC classifiers were similar across OTUs, years, and resampled sensors, with the resultant classification accuracies being similar to the maximum theoretical separability determined for each dataset (Table 3.3).

3.5.3 Imagery

3.5.3.1 High-spatial resolution RGB orthomosaic

The Structure from Motion photogrammetry (703 UAS photographs) produced a high-spatial resolution orthomosaic with a ground sampling distance of 1.16 cm (Figure 3.8a). Pix4D Mapper found a median of 71,013 key points per photograph (435 photographs out of the 703 input were calibrated), and a median of 1489.9 matches between adjacent photographs. The mean residual root mean square error in the positional accuracy of the orthomosaic related to the GCPs was 1.14 m. The blank spaces in the lower middle section of the final orthomosaic due to the interference of surface glare which precluded identifying key points in those areas (Figure 3.8a).

3.5.3.2 Airborne hyperspectral imagery target detection

The atmospherically corrected CASI HSI image and the directly-georeferenced DII image are presented in Figure 3.8b, c. SAV was detected in 5,444 pixels (5,527 m^2, 0.55 ha) of the total 65,160 water pixels (66,148 m^2, 6.6 ha) contained in the DII image, Likewise, non-vegetation substrate was detected in 2,518 pixels (2,556 m^2, 0.26 ha) (Supplementary Table 3.2). A total of 6,368 pixels (6,465 m^2, 0.65 ha) were detected to contain one of the seven more granular target classes. The range of the ACE detection statistic attributable to mixed pixels varied widely across classes, though the mean ACE value of the mixed pixels was never greater than the threshold value (Figure 3.9). For some classes, such as metaphyton and non-vegetation, the range of the

ACE detection statistic values representing mixed pixels is exceedingly small, perhaps indicating that the points considered mixed pixels did not contain enough of the material to produce an identifiable spectral contribution.

3.5.3.3 Target detection validation

An example of the target detection validation for *Potamogeton* sp. is shown in Figure 3.10. In this example, pure points of *Potamogeton* cover were detected in 10 of 13 instances, resulting in a recall of 77%; mixed pixels were however poorly detected with only one of nine mixed pixels detected (combined pure and mixed pixel recall of 50%). Overall, the target detections, for the OTUs and the binary vegetation/non-vegetation classes, were effective, especially when considering validation points representing pure pixels (Table 3.4). The target detection validation with pure pixels resulted in an overall, average accuracy of 87.8% across the individual OTUs and two non-vegetation classes, and 93.6% for the binary vegetation/non-vegetation classes. Including mixed pixels (i.e., points with more than one cover type present) in the validation reduced the overall accuracy of the target detection to an average of 67.0% across the OTUs. In this case the label of each class with > 40% areal coverage was assessed. The asphalt class was perfectly recalled, and the silt/rock class achieved 94% recall, however 408 (414 m^2, 0.04 ha) instances of asphalt were detected in the silt/rock class. The metaphyton class was poorly recalled; potentially due to the limited training and validation data or due to biophysical properties of the metaphyton itself. The binary vegetation and non-vegetation classes were very well detected (recall of 94%). Notably, 5 of the 6 instances of missed vegetation (false negatives) represented points of ribbon-like plants (*V. americana* and *S. graminea*).

3.5.3.4 Expert interpretation

Twelve visual interpreters completed the manual online SAV identification. The true positives from the visual interpreters are shown in Figure 3.11, alongside true positives of the ACE target detection validation. Generally, the visual interpreters accurately identified extensive (> 40% areal coverage) SAV cover, with class recall rates of between 67% and 96%. Detection of individual plants was however less effective and consistent, with recall between 49% and 89% (Figure 3.12). While manual image interpretation was more successful at detecting most of the SAV OTUs, higher recall values were achieved using ACE for detecting *Chara* sp. and *P. richardsonii* at the species level. There was a wide variability in interpretation responses, for

example in the detection of extensive *P. richardsonii* or ribbon-like plants as seen in Figure 3.11 suggesting that *in situ* manual observations of vegetation by those who are not already closely acquainted with the plants may not be accurate.

3.6 Discussion

The leaf-level separability analysis has shown that freshwater SAV does indeed contain sufficient spectral diversity within the VIS and NIR to be reliably separated with hyperspectral data across various OTU definitions (Table 3.2). *In situ* mapping of that same set of SAV, while successful overall, highlights that the use of remote sensing in monitoring SAV is limited by the spatial resolution of imagery available.

3.6.1 Water column impacts

Our submerged panels measurements reveal that the usable spectral region was limited to wavelengths <950 nm due to the strong absorption of radiation by water in the NIR (Figure 3.6). Although 950 nm is somewhat more restrictive than the maximum wavelength used in other work (e.g., 1050 nm by [26] and 1000 nm by [173]), the selection of this upper limit is supported by water's third harmonic absorption peak at ~960 nm, after which absorption remains high [50]. Therefore, future work should expect useful information exclusively from the VIS (e.g., up to 700nm) and shortest wavelengths in the NIR regardless of bathymetry for all water types. As little as 5 cm of submergence reduced the panel R_{abs} to 0.66 at 550 nm and to 0.34 at 900 nm. Under a 40 cm thick water column, R_{abs} reduced further to 0.52 at 550 nm and 0.00 at 900 nm (Figure 3.6). A very high signal-to-noise ratio (SNR) would hence be necessary to meaningfully capture radiance from underwater targets (e.g., Muller-Karger et al. (2018) cite an SNR of 800 as sufficient for aquatic studies). However, even upcoming sensors conceptualized specifically for aquatic applications are not expected to meet such high SNR demands (e.g. PRISM has a SNR of 500 in the blue region [94]; PACE is expected to have an SNR ranging from 400 to 1700 [371].

3.6.2 Leaf spectroscopy

3.6.2.1 Effect of biofouling and season

At the leaf-level, confirming previous findings by Fyfe (2003), it was found that light fouling had very little effect on species' mean reflectance signatures though it did mask some intra-class variability in the NIR (Supplementary Figure 3.1a, b), which may explain the minor,

yet positive, effect fouling produced on class separability in both years (Table 3.2). As neither the fouling load nor its composition were examined, the relationship between fouling and spectral response cannot be here defined. Still, these results are encouraging for future mapping efforts in fluvial freshwaters such as the St. Lawrence River where light fouling is common. As expected, season substantially affected the SAV species' spectral signatures (Supplementary Figure 3.2b). Increased variability was prominent in the late-growing season samples compared to their peak-growing season counterparts (Supplementary Figure 3.2c, d) potentially due to the increased relative concentration of accessory pigments later in the growing season [372,373]. This evolution in leaf spectral response through senescence, combined with the recorded changes in spectral response as a young leaf matures [57], indicate that SAV spectral measurements are temporally distinct and could be used to estimate plant maturity.

3.6.2.2 Leaf level feature selection and separability

Physiological changes occurring within leaves throughout maturation were reflected in the features selected as important contributors to class separability (Figure 3.8). Mesophyll thickness, intra-cellular space, and leaf thickness determine the number of multiple refractions within a leaf and mediate NIR reflectance, previously shown in terrestrial plants [353]. The lack of structural complexity and diversity in the SAV leaves examined here (Supplementary Figure 3.6) thus explain the NIR's irrelevance in achieving spectral separability in the peak-growing season. However, the introduced structural diversity in the late-growing season due to uneven senescence resulted in NIR features to contribute most to separability for the majority of the OTUs (e.g., 938 nm and 809 nm were top ranked for discriminating across all species and between vegetation and non-vegetation, respectively).

Besides changes in leaf and cellular structure, the selected features mirrored the evolution of pigment concentrations throughout the growing season. The Chl-a reflectance peak, referred to as the green peak (~550 nm) was the primary contributor to spectral separability for most OTUs during the peak-growing season when plants invest in Chl-a production. Chl-a absorptance was comparatively unimportant later in the summer when Chl-a is less abundant due to increased shading [374] and plants redirect resources toward accessory pigments [372]. This temporal variability in relative pigment abundance also explains the substantial increase in moderately to highly ranked features in the red and red edge regions (650–710 nm). The total pigment absorptance feature (~445 nm) was the most important contributor to separability in

both years when distinguishing between plants and algae possibly due to the differences in pigment composition and content between the two kingdoms [375]. The dissimilarity in selected features between the two seasons signifies that the spectral response of SAV is temporally specific; data collected in the peak of summer should not be used to train or validate work done later in the summer, or vice versa.

Contradictory to previous work (e.g. [71]), the decrease in OTU class separability in the late-growing season suggests that SAV monitoring campaigns should target the peak-growing season to maximize accuracy. The maximum separability between classes (Table 3.2) is also related directly to the coarseness of the OTUs. Though aggregating multiple similar species into more coarsely defined classes such as genera (rather than species) increases the intra-class spectral variability, it can likewise increase inter-class variability, improving classification results. Although this study is the first instance of it being documented in vascular aquatic plants, the improvement in class separability in higher-level OTUs has previously been demonstrated in macroalgae (species vs clade) and trees (population vs species) [87,376]. Interestingly, class separability increased not only across progressively higher taxa but also in the combination of species into the ad hoc group that was not exclusively based on evolutionary proximity. While spectral similarity *may* relate to a common phenotype or functional group, shared traits cannot be assumed to confer the spectral similarity that would produce accurate classification [377]. The high separability of the ad hoc group (Table 3.2) is therefore encouraging for ecosystem managers that may be interested in classes other than taxonomy, like growth type.

3.6.2.3 Resampled air and spaceborne sensor spectra

Even though high spectral separability was obtained after resampling the leaf level spectra to the RSRs of Sentinel-2 and MODIS (Table 3.2), these resampled spectra model a signal originating from a single species (i.e., pure pixels) and do not account for the uncertainties of even the most accurate radiometric, atmospheric and water column corrections, conditions that cannot be met with actual imagery. To be reliably detect in imagery, targets need to be at least twice the length of a pixel's diagonal [124]. Patches of vegetation would thus need to be at least 28 m in diameter to be detected by Sentinel-2's 10 m pixels; only one stand of this size was observed in this study, while all others were much smaller (<10 m in diameter). Reliable detection in MODIS pixels would require patches over 282 m in diameter. The spatial resolution of current spaceborne sensors thus precludes their use with many in-land freshwater ecosystems

in which such large extents of vegetation are rare. Past sensors, such as Landsat TM5 and EO-1 ALI, had been included to examine the feasibility of retrospective analysis on archived data (Table 3.2). While the retrieval of historical images to extend time series is common in other fields, the poor separability between all but the coarsest OTUs (i.e., the binary vegetation/non-vegetation classes) severely restricts the utility of archived satellite imagery in SAV research.

In contrast to the satellites, very good separability (LNN criterion values of between 0.76 and 1 for the species-level OTU of unfouled samples and the vegetation/non-vegetation OTU, respectively) was achieved for peak-growing season spectra resampled to the CASI RSR for all OTUs (Table 3.2). This is unsurprising, given the CASI's high spectral resolution in terms of both band width and number of bands. As the CASI is an airborne sensor, the high spatial resolution (~1 m pixel size) is also much better suited to the spatial distribution patterns of SAV than spaceborne platforms. Airborne hyperspectral imagery such as that produced by the CASI is thus expected to be appropriate for SAV mapping.

3.6.3 Imagery

3.6.3.1 Airborne hyperspectral imagery Depth Invariant Index (DII)

A novel DII transformation [141,144,378] based on a hyperspectral point cloud as opposed to conventional geocorrected, resampled raster imagery [366,367] was implemented to optimize the data quality of the CASI imagery. While Lyzenga's DII may be highly effective at distinguishing between bottom cover types, its performance depends entirely on the two input bands. If two (or more) targets do not reflect differently in the two wavelengths chosen, a DII calculated using those bands will not be unique to either material [141]. Considering that two materials may be spectrally alike in some, but not all pairs of wavelengths, computing all possible DIIs ensures that the spectral diversity in the signals is represented. A set of all possible DII values however increases the data dimensionality, rendering it (in the case of hyperspectral data) computationally unfeasible (i.e., 5565 DII bands from a 106 input-band image). The DII transformation used here addressed this by sub-setting all possible DIIs to only those below a 0.9 covariance threshold. Thus, most unique spectral information was retained, the imagery dimension was limited, and the water column was compensated for. Work by Mumby et al (1998) demonstrated that implementing as few as two DII bands and some contextual editing could improve bottom cover classification accuracy (between 4 and 13 classes) by up to 23%. It

is thus expected that maximizing the number of DII bands with unique information would similarly increase mapping accuracy. However, if reliable bathymetric information is available, empirical methods such as that described in Purkis and Pasterkamp (2004) could be used to retrieve relative bottom reflectance as opposed to the transformed DII values, facilitating interpretation. By rasterizing the georeferenced DII point cloud without resampling (Figure 3.9), the original image acquisition geometry was respected and facilitated extraction of the target DII spectra and validation points based on the RGB orthomosaic and field sampling. Furthermore, because the goal of this study was fine scale target detection, it was critical to preserve all pixels captured in the raw imagery. The Directly-georeferenced Hyperspectral Point Cloud method implemented here was shown to substantially reduce target detection false negatives due to pixel loss over conventionally georeferenced and resampled raster imagery [367]; applying this method therefore maximized the number of potential target pixels included in the analysis.

3.6.3.2 Airborne hyperspectral image target detection

The ACE detection statistic thresholds were chosen to discern known areas of class cover and minimize false positives. These thresholds were strict, as shown in Figure 3.9 by the mean mixed pixel always being outside the target class range. It is thus unlikely that these sub-pixel targets could be effectively detected without producing many false positives. The target classes were limited to the OTUs present in patches of similar size to the CASI pixel resolution (~1 m) to avoid classes of uniquely sub-pixel targets. Hence, not all SAV species included in the leaf-level analysis were targets in the imagery (e.g., *E. canadensis* and *M. spicatum* were both abundant at the site, but did not form large, monotypic stands). If a sparse or non-canopy forming species, such as the invasive *M. spicatum* were of critical interest, monitoring efforts would require imagery on the scale of a few centimeters such as that produced from RPAS-mounted sensors (e.g. [116]).

The ACE target detections identified points of pure bottom cover well, particularly for the binary vegetation/non-vegetation classes (Table 3.4, Figure 3.10). ACE uses target and non-target input spectra to estimate and disregard noise that is shared between the two groups. It produces a single statistic value that is invariant to changes in scaling (such as might be produced by changes in signal strength due to variable water column thickness) [380]. Previous work by Flynn and Chapra (2014) confirms the utility of ACE in mapping aquatic targets by correctly

detecting *Cladophora* extent with 90% accuracy. Macfarlane et al (2021) additionally determined the ACE algorithm to be most effective in airborne hyperspectral target detection in a cross-comparison of five target detection processes. As ACE uses all input target spectra to calculate a mean target profile, it is unsurprising that five of the six false negative vegetation points were in dense patches of ribbon-like plants. These plants (*S. graminea* and *V. americana*) tended to be visibly darker and redder than other species (Figure 3.2) and were, in some areas, sufficiently dark to be confused with deep water pixels. Thus, spectra of these dense stands were too different from the average of all vegetation (mostly greener and brighter) (Figure 3.7) to be detected without introducing innumerable false positives. Separating the darker, redder vegetation into its own class may thereby be more effective. The very good overall detection recall across vegetation types (Table 3.4) suggests that a similar methodology would be of use in management situations in which the growth type is of interest, such as in maintaining clear navigation corridors or preventing the establishment of tall vegetation near water intakes.

3.6.4 Manual field photograph interpretation

Manual interpretation of field photographs was conducted to compare the performance of traditional surveys of SAV and the remote sensing methodology used here. Interpreters completed two tasks (selecting images that presented >40% cover of a specified bottom type and identifying all images with any instance of the specified bottom type) to simulate detection of full-pixel and sub-pixel targets. Recall values were not substantially different between manual detection of extensive bottom cover and the ACE target detection of pure pixels (Figure 3.11), suggesting that the remote sensing methods used here could produce similarly accurate results to in person surveys conducted by researchers that are not already well acquainted with the vegetation. Photograph interpretation for sub-pixel target identification was generally less successful, with more response variability. This decrease in manual interpretation success mirrors the decline in recall of the ACE target detections when including mixed pixels in the validation set (Table 3.4). While manual interpretation remains more effective at detecting targets over a small area, the remote sensing methods used here provided acceptable target detection rates and could be applied to a larger spatial scale by a smaller team.

3.6.5 Overall importance

Our results show that the SAV examined do present enough spectral diversity to be separable despite the limited spectral range available in aquatic remote sensing and the general lack of identifying information in the NIR. That separability extends beyond taxonomic groupings, having been observed in the ad hoc grouping roughly based on phenotype. Mapping and identifying SAV through optical remote sensing is therefore anticipated to be an appropriate tool in a broad range of management and research applications. Using airborne hyperspectral imagery to map that same SAV demonstrated that very high detection rates can be achieved for targets of a similar size to the imagery pixels. The increasing availability of RPAS platforms, and thereby higher spatial resolution imagery, is expected to further extend to scope of aquatic targets suited to detection and mapping through remote sensing. This work has shown that optical remote sensing is indeed a viable alternative to manual surveys for monitoring SAV in shallow clear to moderate optical water types from freshwater ecosystems, and its spectrum of potential uses is still growing.

3.7 Conclusion

To address some of the fundamental knowledge gaps remaining in the application of optical remote sensing to freshwater ecosystems identified by Rowan and Kalacska (2021), the spectral separability amongst thirteen SAV species was examined under laboratory conditions and through actual airborne imagery. Implementing a multi-scale approach provided insight into what is currently possible for researchers/practitioners working across scales and with varying resources and highlighted future possibilities from further technological innovation and investment. The species of SAV were reliably separable under laboratory conditions from leaf-level spectroradiometer data, with light leaf fouling having minimal effect but seasonality being an important determinant of separability. As the samples were found to be less separable late in the growing season than at its peak, it is recommended that future studies consider avoiding late-growing season data collection. Additionally, separability was improved with progressively higher-level OTUs (i.e., genus or kingdom). Resampling the leaf level spectra to simulate spaceborne sensors reduced separability, demonstrating that most publicly available satellite data products do not have the necessary spectral resolution required for reliable SAV separation; those that do, lack the high spatial resolution needed to study freshwater SAV communities. Resampling the leaf level spectra to simulate the CASI, an airborne hyperspectral sensor, produced high separability results. Combining this high separability with the fine spatial

resolution achievable from airborne platforms, airborne HSI with similar spatial and spectral characteristics could be amenable to SAV monitoring applications. Detecting instances of target vegetation and bottom cover from the airborne HSI was effective, though it was limited to cover types occurring in patches of similar size to the imagery pixels, meaning not all species at the site could be detected. Before SAV can be operationally mapped in freshwaters across broad spatial extents, higher resolution spaceborne sensors and more precise pre-processing workflows for low signal level targets are needed. The enhanced radiometric correction (i.e., IFRR) used here enhanced the useable low-level signals and the novel DII transformation allowed for an effective water column compensation. Importantly, the directly-georeferenced point cloud data model ensured maximal retention of information and spatial integrity. These improvements over conventional aquatic remote sensing workflows are thus recommended for application in future SAV monitoring and mapping endeavors. Freshwater SAV has here been shown to contain sufficient spectral diversity for reliable separation, though the success of *in situ* applications remains limited by the spectral and spatial resolution of available data.

3.8. Tables and Figures

Table 3.1. Results of the forward feature selection algorithm for the full resolution ASD spectra. The 95% of maximum LNN criterion value and number of features required to produce 95% of the maximum separability are included as many selected features provide only marginal gains in separability.

Dataset grouping, fouling, season (code)	Max LNN	95% of max LNN	No. features selected to max LNN	No. features to 95% of max LNN
By species, fouled, peak-growing season (f19)	0.84	0.80	38	10
By species, unfouled, peak-growing season (u19)	0.82	0.77	281	13
By species, combined, peak-growing season (a19)	0.80	0.76	276	23
By genus, combined, peak-growing season (p19)	0.81	0.77	258	14
Ad hoc, combined, peak-growing season (g19)	0.84	0.80	267	10
By kingdom, combined, peak-growing season (alga19)	0.98	0.93	52	4
Vegetation/non-vegetation, combined, peak-growing season (s19)	1.00	0.95	58	1
By species, fouled, late-growing season (f20)	0.56	0.53	32	19
By species, unfouled, late-growing season (u20)	0.55	0.52	57	15
By species, combined, late-growing season (a20)	0.55	0.52	238	15
By genus, combined, late-growing season (p20)	0.56	0.54	162	15
Ad hoc, combined, late-growing season (g20)	0.62	0.59	64	10
By kingdom, combined, late-growing season (alga20)	0.98	0.93	13	3
Vegetation/non-vegetation, combined, late-growing season (s20)	1.00	0.95	6	1

Table 3.2. Maximum LNN values for each grouping and year for the original (ASD) spectra and all resampled spectra. Multi and hyperspectral sensors to which the spectra were resampled are ordered by increasing spectral information (No. bands). Cells have been coloured according to their value for rapid interpretation (gradient: red = 0.2, yellow = 0.6, blue = 1). All values above 0.7 have been bolded for easy identification. *CASI is an airborne hyperspectral imager, all others are multi-spectral spaceborne sensors.

	f19	**u19**	**a19**	**p19**	**g19**	**alga19**	**s19**	**f20**	**u20**	**a20**	**p20**	**g20**	**alga20**	**s20**
Landsat 5 TM	0.56	0.54	0.52	0.53	0.57	**0.86**	**1.00**	0.34	0.31	0.34	0.36	0.42	**0.92**	**0.99**
RapidEye	0.64	0.58	0.59	0.61	0.66	**0.89**	**1.00**	0.43	0.40	0.42	0.44	0.49	**0.93**	**0.99**
Landsat 8	0.58	0.55	0.53	0.54	0.59	**0.87**	**1.00**	0.36	0.33	0.33	0.35	0.43	**0.92**	**0.99**
EO-1 ALI	0.64	0.62	0.63	0.62	0.66	**0.87**	**1.00**	0.39	0.36	0.39	0.41	0.47	**0.93**	**1.00**
Sentinel 2	**0.73**	0.70	0.69	0.70	**0.75**	**0.90**	**1.00**	0.48	0.45	0.49	0.50	0.54	**0.93**	**1.00**
MODIS	**0.73**	0.70	0.69	**0.70**	**0.74**	**0.93**	**1.00**	0.45	0.43	0.43	0.45	0.52	**0.95**	**1.00**
CASI*	**0.81**	**0.76**	**0.76**	**0.77**	**0.82**	**0.98**	**1.00**	0.53	0.52	0.52	0.53	0.59	**0.97**	**1.00**
ASD	**0.84**	**0.82**	**0.80**	**0.81**	**0.84**	**0.98**	**1.00**	0.56	0.55	0.55	0.56	0.62	**0.98**	**1.00**

Table 3.3. Classification accuracy of the FSDC, NUSVC, and RBSVC classifiers for each grouping and year for the original (ASD) and all resampled spectra. Accuracy values have been colour coded for rapid interpretation (gradient: red = 0, yellow = 0.5, blue = 1). All values above 0.7 have been bolded for easy identification. Datasets are described in Table SM3.2

		Classification accuracy (%), by dataset													
Sensor	**Classifier**	**a19**	**f19**	**u19**	**p19**	**g19**	**alga19**	**s19**	**a20**	**f20**	**u20**	**p20**	**g20**	**alga20**	**s20**
Landsat 5 TM	FDSC	53	56	59	56	59	**89**	**100**	38	41	33	39	46	**94**	**100**
	NUSVC	17	33	30	21	49	**76**	**100**	26	31	29	28	40	**87**	**98**
	RBSVC	51	54	47	51	59	**86**	**100**	32	43	34	43	41	**94**	**100**
Rapideye	FDSC	61	64	61	63	66	**90**	**100**	50	48	43	51	53	**94**	**100**
	NUSVC	23	36	41	22	54	**75**	**100**	37	36	40	38	34	**93**	**98**
	RBSVC	61	60	58	61	67	**89**	**100**	49	42	47	49	51	**94**	**99**
Landsat 8 OLI	FDSC	55	63	54	58	63	**87**	**100**	42	38	37	41	47	**93**	**99**
	NUSVC	22	45	35	20	43	**75**	**100**	37	25	42	42	45	**93**	**99**
	RBSVC	50	59	55	53	68	**87**	**100**	38	41	36	47	43	**95**	**100**
EO-ALI	FDSC	63	65	64	63	**70**	**89**	**100**	46	46	41	48	54	**95**	**100**
	NUSVC	24	36	55	22	44	**76**	**100**	52	38	43	45	52	**91**	**100**
	RBSVC	60	63	58	62	66	**88**	**100**	48	56	46	46	55	**96**	**100**
Sentinel - 2	FDSC	**74**	**73**	**70**	**73**	**78**	**91**	**100**	56	56	55	61	63	**94**	**100**
	NUSVC	28	47	52	40	62	**79**	**100**	50	48	53	52	58	**93**	**100**
	RBSVC	67	**70**	65	68	**72**	**90**	**100**	53	52	56	54	66	**95**	**100**
MODIS	FDSC	**74**	**75**	**72**	**78**	**78**	**96**	**100**	57	57	52	53	65	**97**	**100**
	NUSVC	49	53	65	54	66	**94**	**100**	64	53	59	63	46	**100**	**100**
	RBSVC	**70**	**74**	**71**	**81**	**79**	**95**	**100**	64	67	57	60	68	**100**	**100**
CASI	FDSC	**85**	**85**	**82**	**87**	**89**	**98**	**100**	65	68	63	63	67	**98**	**100**
	NUSVC	**82**	**82**	**82**	**78**	**81**	**97**	**100**	62	65	61	54	66	**99**	**100**
	RBSVC	**82**	**81**	**77**	**88**	**86**	**98**	**100**	64	66	58	65	**71**	**99**	**99**
ASD	FDSC	**88**	**86**	**86**	**89**	**91**	**98**	**100**	**74**	64	61	**71**	**74**	**99**	**100**
	NUSVC	**80**	**73**	**83**	**79**	**84**	**97**	**100**	**71**	63	**70**	68	**72**	**100**	**100**
	RBSVC	**88**	**88**	**82**	**88**	**90**	**98**	**100**	**84**	68	66	**78**	**75**	**100**	**100**

Table 3.4. Validation results of the target detection analyses. Mixed pixels are identified as having at least 40% cover of the class in question.

	Pure pixels only			Pure and mixed pixels		
Class	**No. Validation points**	**True Positives**	**Recall**	**No. Validation points**	**True Positives**	**Recall**
Chara sp.	24	19	79%	81	53	65%
Metaphyton	2	0	0%	4	0	0%
P. richardsonii	6	6	100%	20	18	90%
Ribbon	18	15	83%	32	20	63%
Potamogeton sp.	13	10	77%	22	11	50%
Road	20	20	100%	20	20	100%
Silt / Rock	17	16	94%	51	32	63%
Overall	98	86	88%	230	154	67%
Vegetation	56	50	89%			
Non-vegetation	38	38	100%			
Overall	94	88	94%			

Table SM3.1. An overview of the samples collected, and the resulting number of darkroom spectra measured. Samples of *N. odorata* are separated according to their location in the water column at time of sampling due to potential differences in pigmentation and structure in immature (submerged) leaves. * Indicates samples that were not included in analysis of unfouled spectra due to degradation.

		No. Samples		**No. Spectra**	
Taxonomic designation	**Code**	**2019**	**2020**	**2019**	**2020**
Ceratophyllum demersum	cerde	1	2	134	63
Chara ssp.	chara	4	4	470	101
Elodea canadensis	eloca	3	7	309	162
Metaphyton	metap	2*	0	28	N/A
Myriophyllum spicatum	myrsp	3	3	141	164
Najas flexilis	najfl	3	4	102	95
Nympheae odorata (floating)	nymoa	3*	3	34	47
Nympheae odorata (submerged)	nymob	3*	3	26	34
Potamogeton ssp.	potas	3	0	126	N/A
Potamogeton crispus	potcr	1*	0	48	N/A
Potamogeton richarsonii	potri	3	4	182	204
Potamogeton robbinsii	potro	1	4	51	133
Sagittaria graminea	saggr	7	5	281	177
Vallisnaria americana	valam	3	6	147	329
Eleocharis acicularis	eleac	0	1	N/A	34
Total collected		**40**	**46**	**2079**	**1543**

Table SM3.2. Definition of the datasets and nomenclature used for the leaf level analysis. Presence/absence grouped all plants together as one class and the silt samples as a second class. The seven classes in the Ad hoc grouping are: 1. *S. graminea* and *V. americana*; 2. *M spicatum*; 3. all *Potamogeton* species; 4. submerged and floating *N. odorata*; 5. *C. demersum, E. canadensis, N. flexilis*, and *E. acicularis*; 6. *Chara* sp.; and 7. Metaphyton.

Year	Fouling	Grouping	No. spectra	No. classes	Dataset code
2019	Fouled	By species	973	14	f19
	Unfouled	By species	1106	10	u19
	Fouled and unfouled together	By species	2079	14	a19
		By genus	2079	11	p19
		By kingdom	2079	2	alga19
		Presence/Absence	2089	2	s19
		Ad hoc	2079	7	g19
2020	Fouled	By species	777	12	f20
	Unfouled	By species	766	12	u20
	Fouled and unfouled together	By species	1543	12	a20
		By genus	1543	11	p20
		By kingdom	1543	2	alga20
		Presence/Absence	1554	2	s20
		Ad hoc	1543	8	g20
Both	Fouled	By species	990	15	a1920

Table SM3.3. Band characteristics of the spaceborne sensors to which the leaf level spectra were resampled. 'Max RSR λ' refers to the wavelength at which the maximum Relative Spectral Response is found. The Full Width Half Max (FWHM) is an indication of band width; it is rounded and not an exact value.

Sensor	Band	Range (nm)	Max RSR λ (nm)	FWHM (nm)
Landsat 5 TM	Blue	420 - 550	503	65
	Green	501 - 645	594	81
	Red	580 - 740	677	67
	NIR	730 - 945	800	128
RapidEye	Blue	438 - 512	505	69
	Green	515 - 593	584	70
	Red	625 - 689	678	54
	Red Edge	684 - 736	698	43
	NIR	749 - 860	765	91
Landsat 8 OLI	Coastal Aerosol	427 - 459	445	16
	Blue	436 - 528	509	60
	Green	512 - 610	550	58
	Red	625 - 691	656	38
	NIR	829 - 900	859	28
	Pan	488 - 692	663	172
E-O1 ALI	1	415 - 559	509	62
	1p	415 - 494	446	20
	2	500 - 630	596	75
	3	575 - 740	683	59
	4	750 - 840	779	30
	4p	800 - 935	854	45
	Pan	440 - 740	656	166
Sentinel-2	1	430 - 457	446	17
	2	440 - 535	520	53
	3	537 - 582	560	35
	4	646 - 684	654	30
	5	694 - 713	700	14
	6	731 - 749	743	14
	7	769 - 797	778	19
	8	773 - 908	789	115
	8a	848 - 881	871	20
	9	932 - 958	947	19
MODIS	8	400 - 423	416	14
	9	433 - 448	441	10
	3	452 - 480	460	12
	10	478 - 495	488	10
	11	520 - 540	530	11
	12	538 - 556	547	11
	4	539 - 568	550	20
	1	614 - 681	658	47
	13	656 - 674	665	10
	14	666 - 687	676	11
	15	736 - 757	746	10
	2	820 - 898	863	38
	16	852 - 881	865	16
	17	471 - 938	902	44
	19	890 - 958	940	46
	18	923 - 948	935	14

Table SM3.4. Parameters of the CASI image acquisition and atmospheric compensation in ATCOR 4.

Stage of image preparation	Parameter name	Value and units
Flight and image acquisition	Date of collection	26/07/2019
	Time of collection	15:19:51 GMT
	Flight altitude	898 m AGL
	Flight speed	80 knots
	No. bands acquired	144
	CASI integration time	28 ms
	CASI frame time	28 ms
	Along track pixel spacing	1.152 m
	Across-track pixel spacing	0.434 m
	Wavelength range	376.5-1060.27 nm
	Full width half max (FWHM)	5.04 nm
Atmospheric Compensation	Aerosol Type	Rural
	Solar zenith angle (SZA)	33.8°
	Solar azimuth angle	130.6°
	Atmosphere	H01000_wv20_rura
	Visibility (scene average)	56.5

Table SM3.5. Classifier selection amongst classifiers tested from the PRtools toolbox through comparison of classification accuracy of the ASD a19 dataset. The classifiers which achieved at least 80|% classification accuracy (testing data) were selected for implementation on all datasets (original and resampled) and are bolded below.

Classifier name	**Abbreviation**	**Testing Accuracy**
Weak classifier	weakc	21%
Decision Tree classifier	dtc	53%
Construct binary decision tree classifier	treec	44%
k-nearest neighbour classifier	knnc	78%
Mixture of gaussians classifier	mogc	6%
Uncorrelated normal densities based quadratic classifier	udc	21%
Scaled nearest mean linear classifier	nmsc	16%
Parzen classifier	parzenc	6%
Parzen density-based classifier	parzendc	6%
Decision stump classifier	stumpc	29%
ADABoost classifier	adaboostc	32%
Breiman's random forest classifier	randomforestc	67%
Feature based dissimilarity space	**fdsc**	**89%**
Discriminative restricted Boltzmann machine classifier	drbmc	61%
Support vector classifier	svc	25%
Nu-support vector classifier	**nusvc**	**83%**
Radial basis support vector classifier	**rbsvc**	**85%**
Voted perceptron classifier	vpc	66%
Linear perceptron	perlc	74%

Table SM3.6. ACE detection statistic thresholds, number of detected pixels and detected area. 'Class' indicates the class being detected, with all other classes being identified as non-target spectra (overall vegetation was only identified as a non-target in detecting the non-vegetation class, as it includes pixels all vegetation types). The 'ribbon' class comprises both *S. graminea* and *V. americana.*

Class	**Threshold**	**No. of pixels**	**Area (m^2)**
Asphalt	0.110	580	589
Chara sp.	0.070	951	965
Metaphyton	0.100	186	189
Potamogeton sp.	0.070	473	480
P. richardsonii	0.080	776	788
Ribbon	0.060	1679	1,704
Silt / Rock	0.070	1723	1,749
Non-vegetation	0.060	2518	2,556
Vegetation	0.030	5444	5,527

Figure 3.1. Subset of CASI airborne hyperspectral imagery (red = 658.77 nm, green = 548.70 nm, blue = 481.71 nm) presenting the study site west of Philpott's Island in the Long Sault Parkway Provincial Park, Ontario, Canada. The yellow box outlines the shallow bay where samples were collected and SAV is mapped. The location of the two calibration tarps is shown in purple. The inset indicates the study site location (red star) in relation to the North American Great Lakes.

Figure 3.2. Examples of the vegetation encountered at the site (A-I) and examples of vegetation provided to expert interpreters (J-N). A) *V. americana*; B) *P. richardsonii*; C) *S. graminea*; D) *M. spicatum*; E) *E. canadensis*; F) Metaphyton; G) *P. robbinsii*; H) *Chara* sp.; I) *V. americana* with heavy leaf fouling; J) *Chara* sp.; K) *P. richardsonii*; L) *S. graminea*; M) *M. spicatum*; N) *Potamogeton* sp.

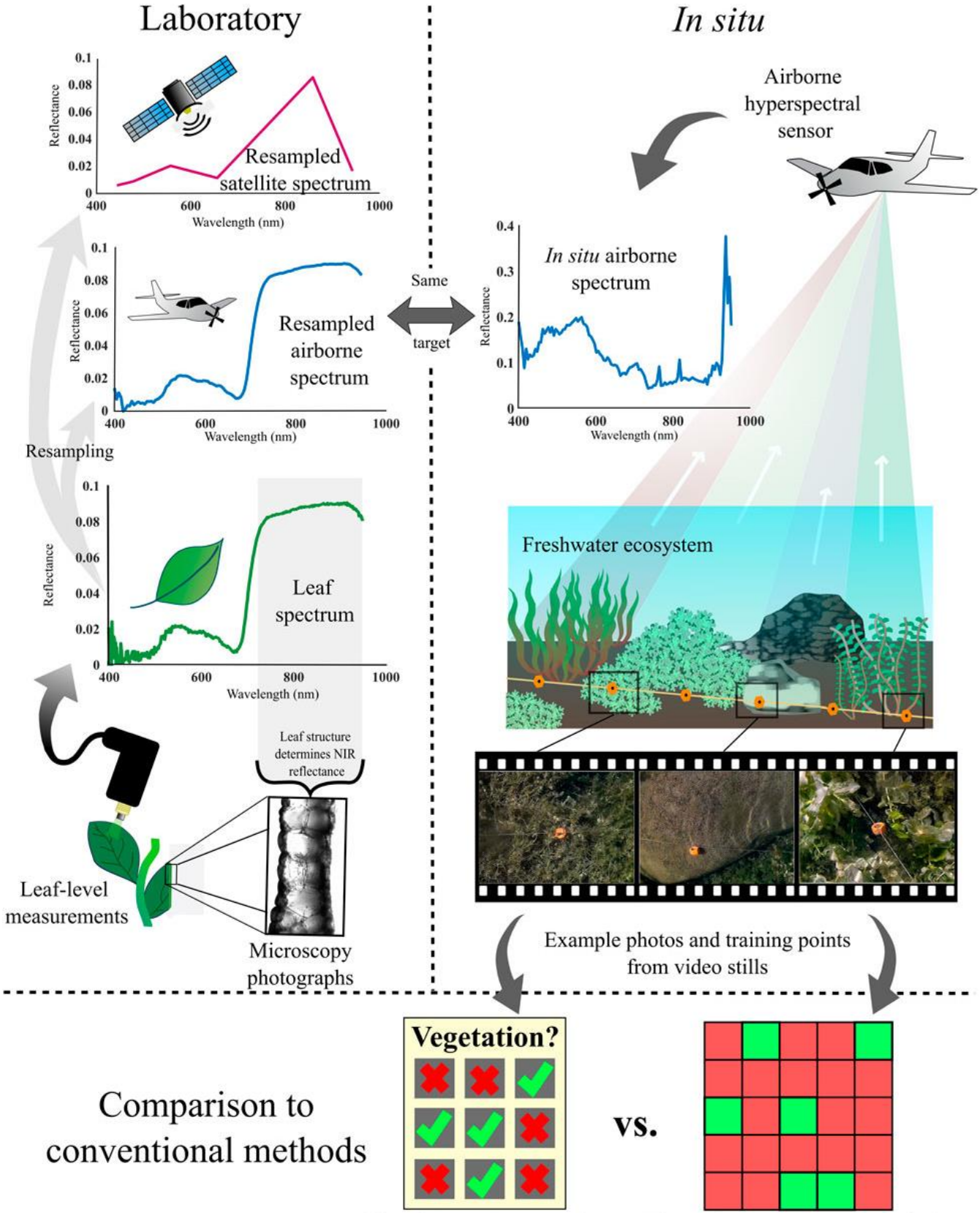
Laboratory
In situ
Reflectance
Wavelength (nm)
Resampled satellite spectrum
Airborne hyperspectral sensor
Resampled airborne spectrum
Same target
In situ airborne spectrum
Resampling
Leaf spectrum
Freshwater ecosystem
Leaf structure determines NIR reflectance
Leaf-level measurements
Microscopy photographs
Example photos and training points from video stills
Comparison to conventional methods
Vegetation?
vs.

Figure 3.3. The multi-scale approach implemented in this study. Laboratory spectral measurements were collected of the leaves of each plant sample collected from the site; microscopy images of leaf cross-sections were then taken for each species to inform subsequent analysis of the leaf spectra. Leaf spectra were then resampled to an airborne and six spaceborne imaging sensors that deploy for large scale in situ applications. A shallow freshwater site was imaged using an airborne hyperspectral sensor from which spectra of the same vegetation examined in the lab could be extracted. Underwater video footage of four transects provided training and ground truth points for SAV target detection from the airborne imagery. Video stills were additionally presented to fellow researchers to be manually interpreted to present the utility of remote sensing in the context of the performance of conventional SAV monitoring methods.

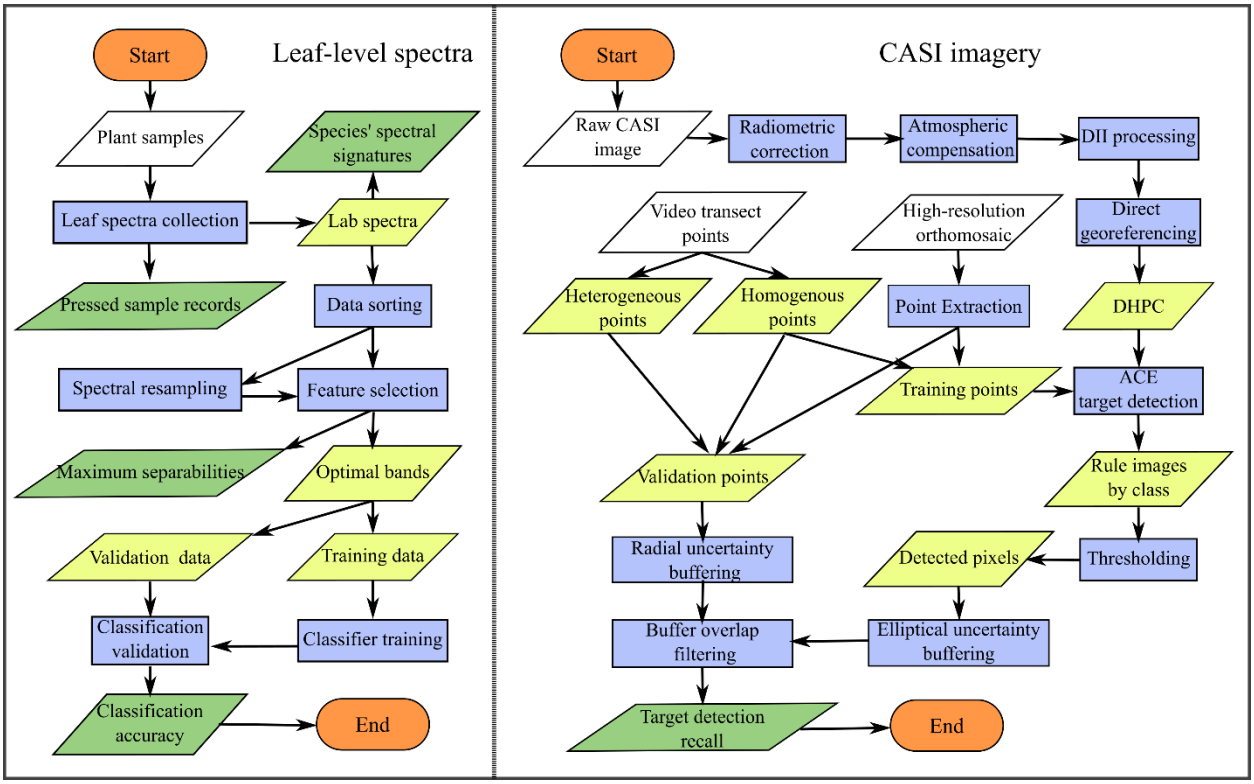

Figure 3.4. Workflow for both the leaf-level spectral analysis and the processing and analysis of the CASI image.

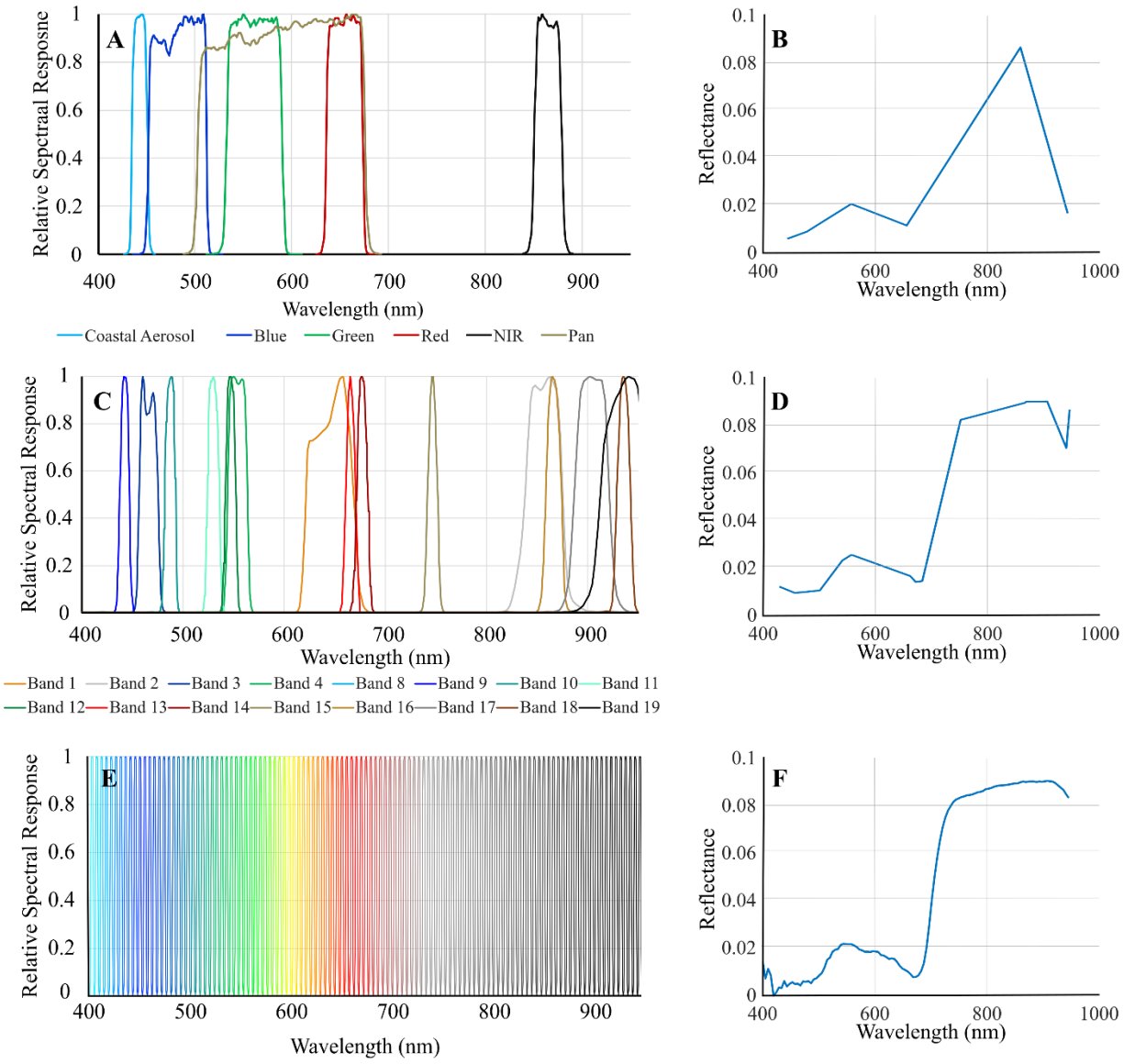

Figure 3.5. Relative Spectral Response (RSR) functions of two satellite sensors and the airborne sensor resampled to in this work for the 400-950 nm spectral range, and an example of a *V. americana* spectrum obtained after each spectral resampling. (**A**) RSR of the Landsat 8OLI sensor. (**B**) *V. americana* spectrum resampled to Landsat 8OLI. (**C**) MODIS's RSR. (**D**) *V. americana* spectrum resampled to MODIS. (**E**) RSR of the CASI airborne hyperspectral imager. (**F**) *V. americana* spectrum resampled to the CASI.

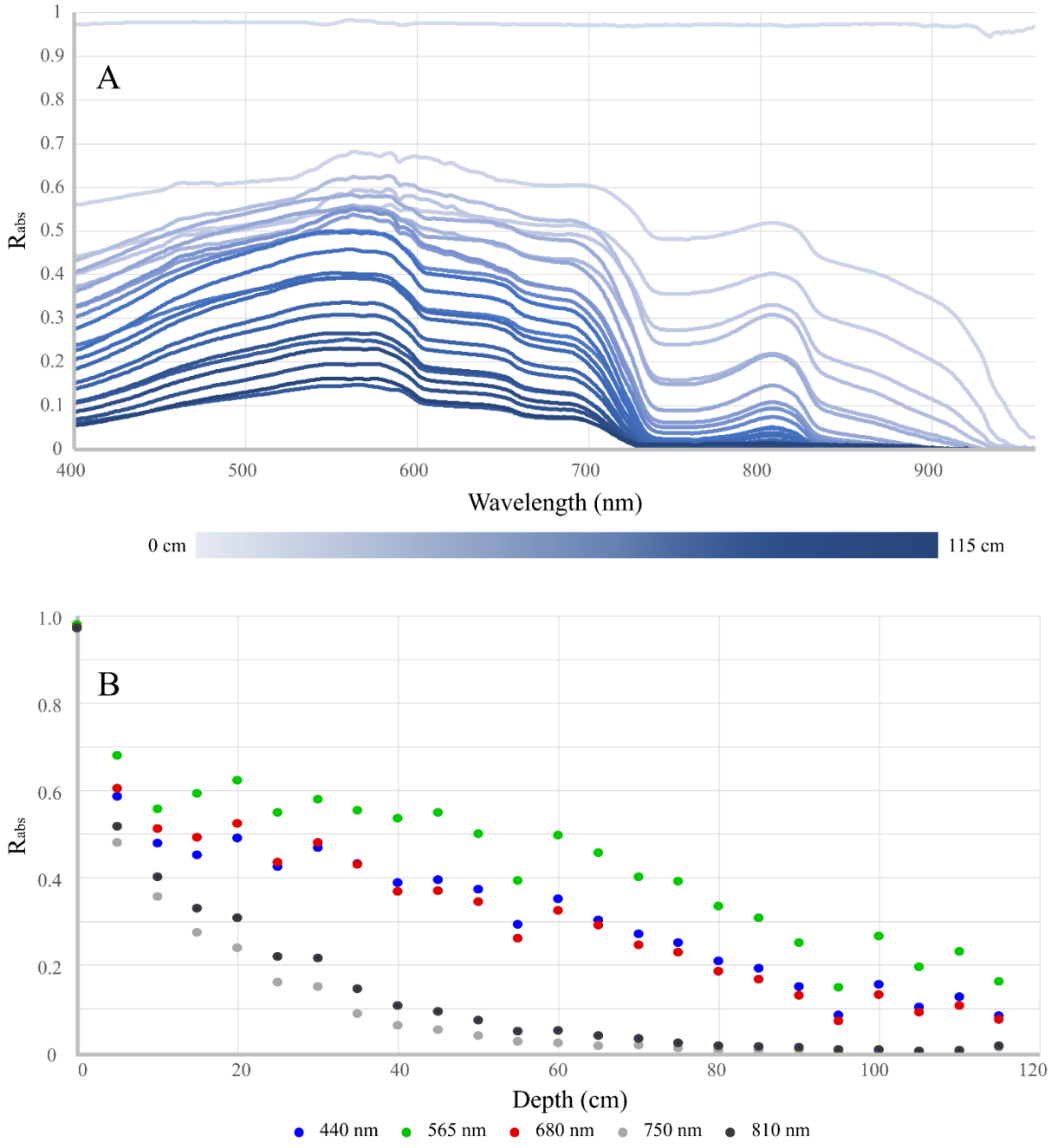

Figure 3.6. Effect of the water column on the reflectance of a submerged 99% Spectralon panel. (**A**) Estimated Absolute Reflectance (R_{abs}) at 5 cm depth intervals between ~0 cm to 115 cm. (**B**) R_{abs} at select VIS (440 nm, 565 nm, and 680 nm) and NIR (750 nm and 810 nm) wavelengths plotted against panel submergence depth.

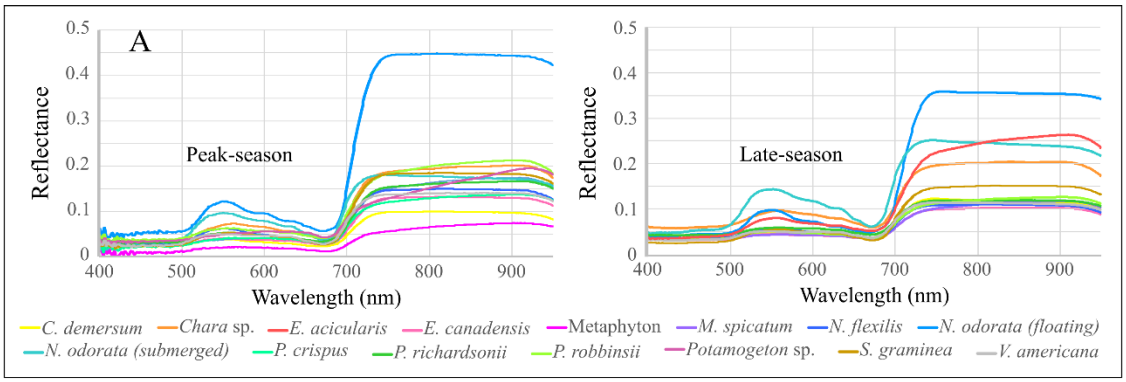
A
Peak-season
Late-season
Reflectance
Wavelength (nm)
C. demersum
Chara sp.
E. acicularis
E. canadensis
Metaphyton
M. spicatum
N. flexilis
N. odorata (floating)
N. odorata (submerged)
P. crispus
P. richardsonii
P. robbinsii
Potamogeton sp.
S. graminea
V. americana

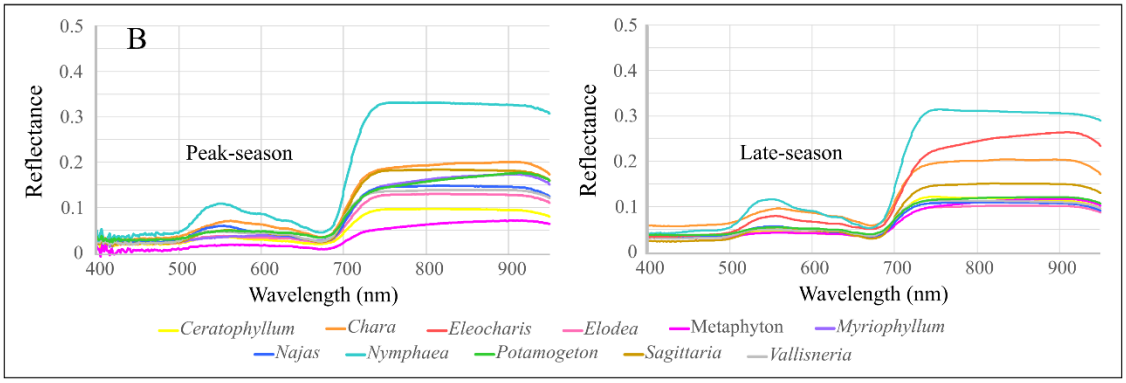
B
Peak-season
Late-season
Reflectance
Wavelength (nm)
Ceratophyllum
Chara
Eleocharis
Elodea
Metaphyton
Myriophyllum
Najas
Nymphaea
Potamogeton
Sagittaria
Vallisneria

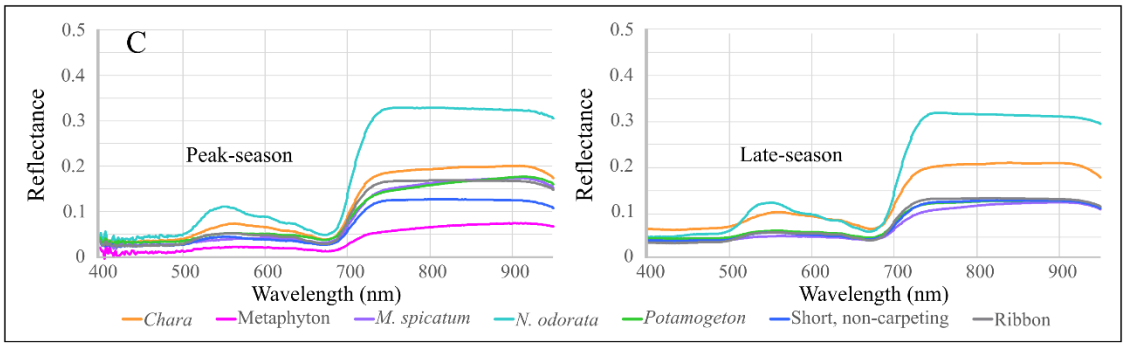
C
Peak-season
Late-season
Reflectance
Wavelength (nm)
Chara
Metaphyton
M. spicatum
N. odorata
Potamogeton
Short, non-carpeting
Ribbon

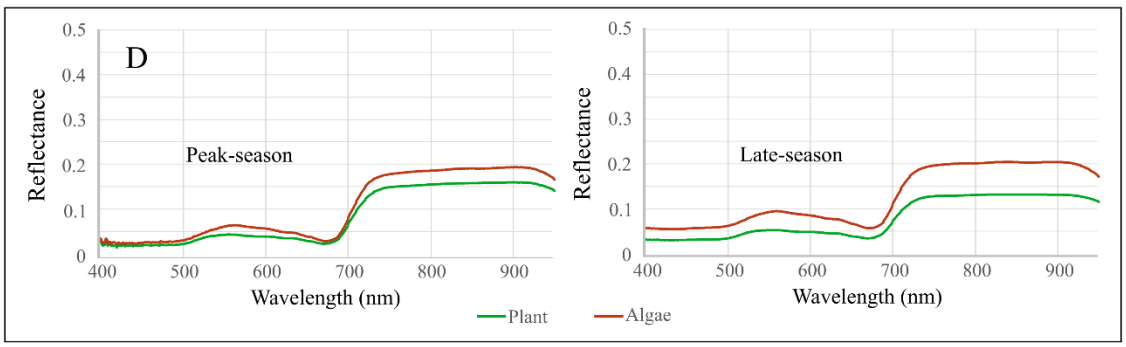
D
Peak-season
Late-season
Reflectance
Wavelength (nm)
Plant
Algae

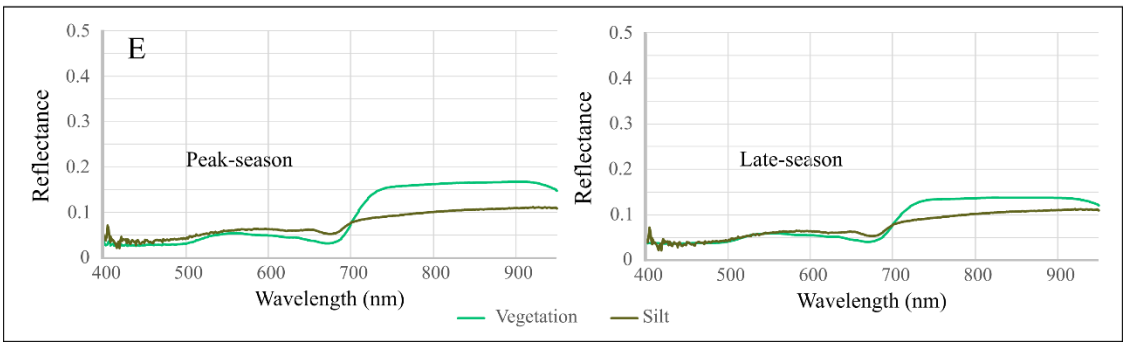
E
Peak-season
Late-season
Reflectance
Wavelength (nm)
Vegetation
Silt

Figure 3.7. Average spectra of all classes in each grouping scheme for both 2019 and 2020. (**A**) All samples grouped by species (a19 and a20); (**B**) All samples grouped by genus (p19 and p20); (**C**) All samples in ad hoc grouping (g19 and g20); (**D**) All samples grouped by kingdom (alga19 and alga20); (**E**) All vegetation samples plus silt samples grouped as vegetation or non-vegetation (s19 and s20).

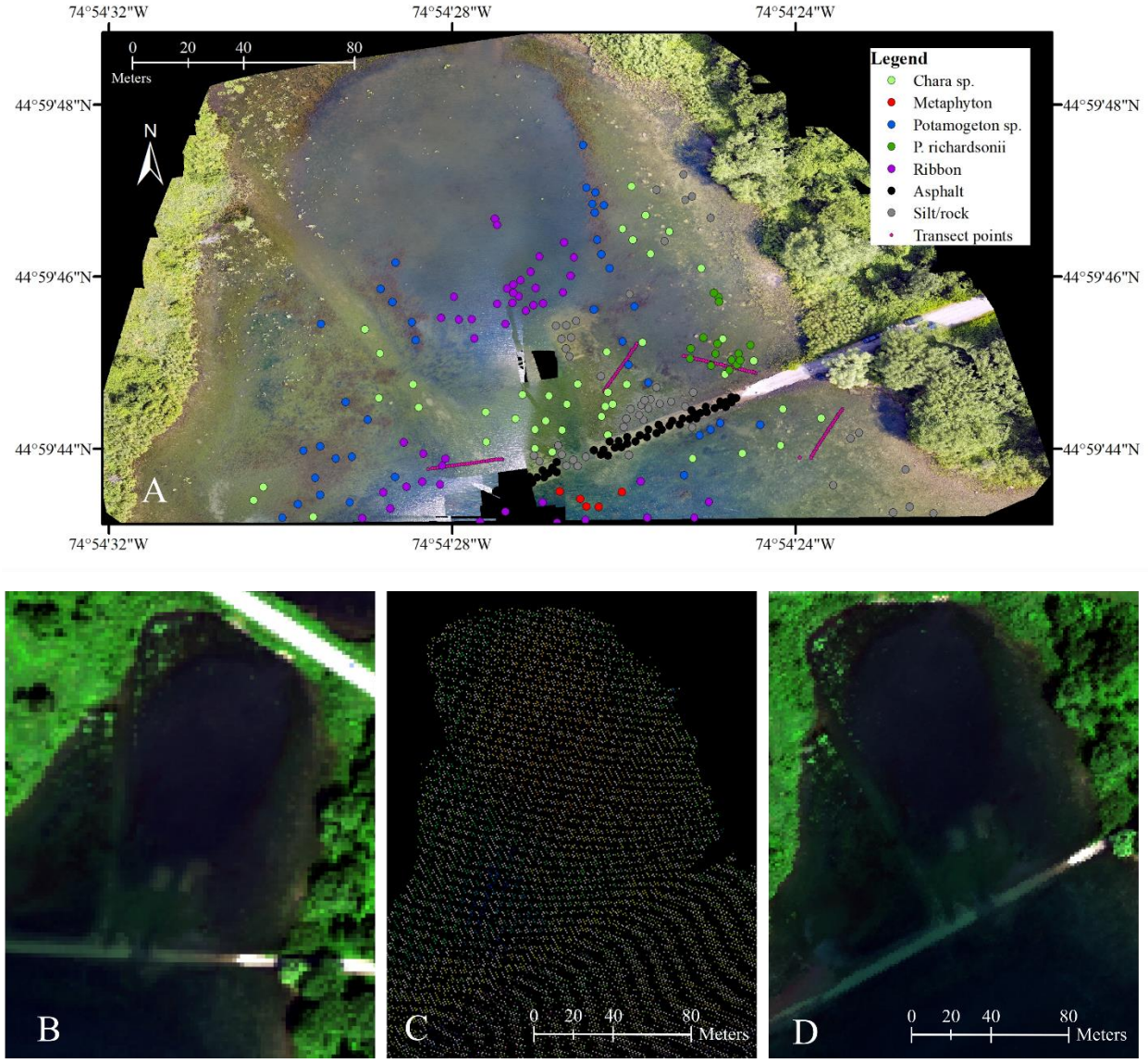

Figure 3.8. CASI imagery used in this work at various processing stages and the input points used in target detection and validation. (**A**) RPAS orthomosaic showing points of each class chosen through visual interpretation and the locations of the transect points. (**B**) Atmospherically compensated CASI image (red=687.5 nm, green = 548.7, blue = 500.3 nm, optimized linear stretch applied on extent) before geocorrection. (**C**) DII-transformed CASI image following rasterization of the directly georeferenced point cloud without resampling (red = 682.7 nm & 701.8 nm DII, green = 553.5 nm & 563.1 nm DII, blue = 424.3 nm & 438.7 nm DII, linear stretch on extent applied). Each pixel is a 25 cm by 25 cm visualization of the set of DIIs centered at the coordinates calculated to be where the signal originated from. (**D**) Conventionally geocorrected CASI imagery after atmospheric compensation, for reference.

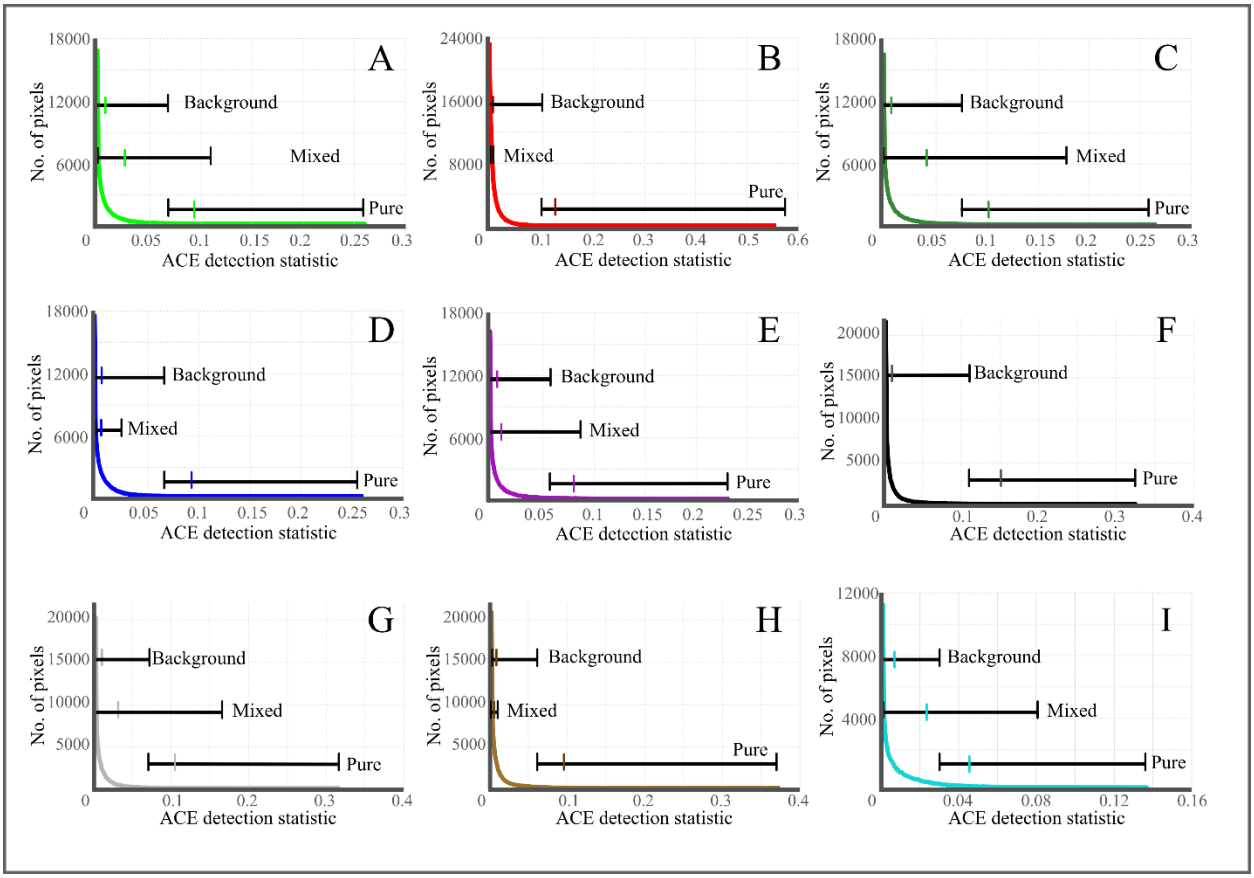

Figure 3.9. Results of the ACE target detection. Curves depict the number of pixels according to the ACE detection statistic assigned. Horizontal bars indicate the range of ACE detection statistic values attributable to each type of pixel (pure target, mixed target, background) with the mean value indicated by a coloured tick mark. Pure and background pixels are separated at the threshold values presented in Table SM3.6; mixed pixel ranges were determined according to ACE detection statistic values of mixed transect points. (**A**) *Chara* sp. (**B**) Metaphyton. (**C**) *P. richardsonii*. (**D**) *Potamogeton* sp. (**E**) Ribbon. (**F**) Road, no mixed pixels identified. (**G**) Silt / Rock. (**H**) Non-vegetation. (**I**) Vegetation.

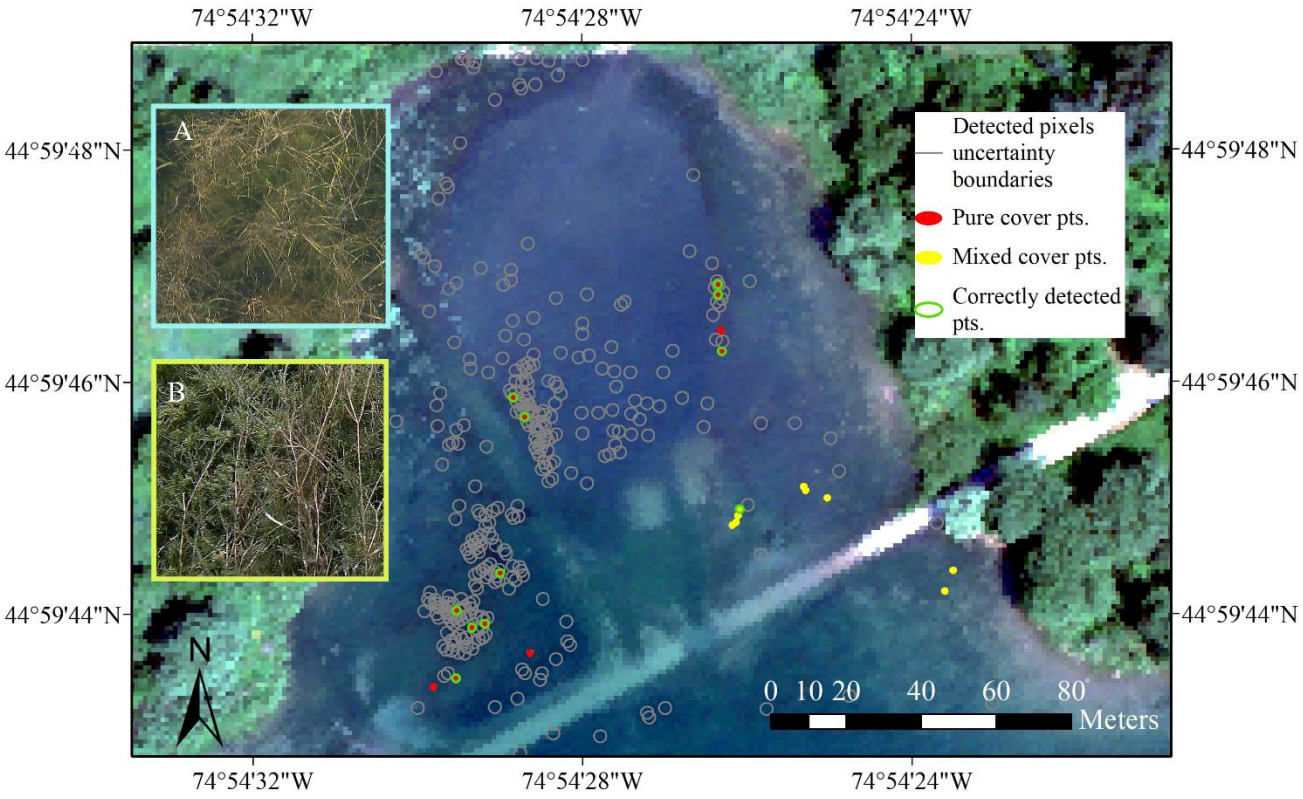

Figure 3.10. Example of validation for the *Potamogeton* sp. target detection with grey ellipses around detected pixels, pure validation points, mixed validation points, and validation points correctly detected identified. Conventionally geocorrected true colour CASI image shown in background for context. Insets are underwater photograph examples of pure *Potamogeton* sp. (**A**) and mixed (**B**) *Potamogeton* sp. and *Chara* sp. cover. In this example, 10 of the 13 pure cover points were detected shown by the green circles; one mixed cover point was detected.

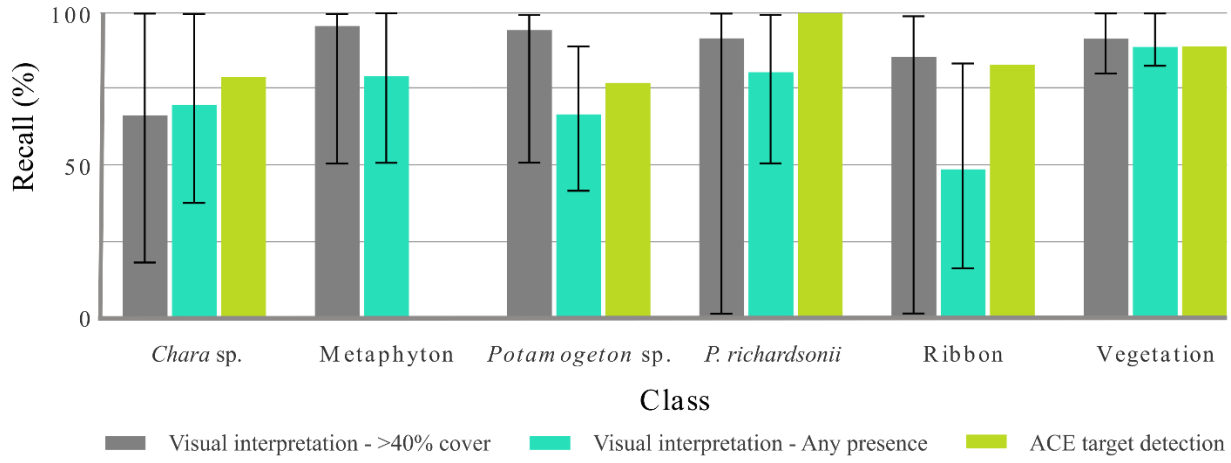

Figure 3.11. Comparison of recall results from visual interpretation, for both 40% class cover and any instance of class presence, and CASI airborne hyperspectral image target detection. The range of responses is shown by the error bars for visual interpretation results.

Figure SM3.1. Experimental field set up. A) RPAS photo of the site acquired the same day (07/26/2019) as the CASI HSI; B) reference target set up for verifying the atmospheric compensation of the CASI HSI, targets are two tarpaulins with known reflectance; C) GCP placed at the site for orthorectification of the RPAS images and orthomosaic; D) improvised floating platform for underwater ASD measurements, measurement of Spectralon reference panel at the water's surface is shown here; E) example transect marker captured in video footage (this point would have been labeled as *Chara* sp.).

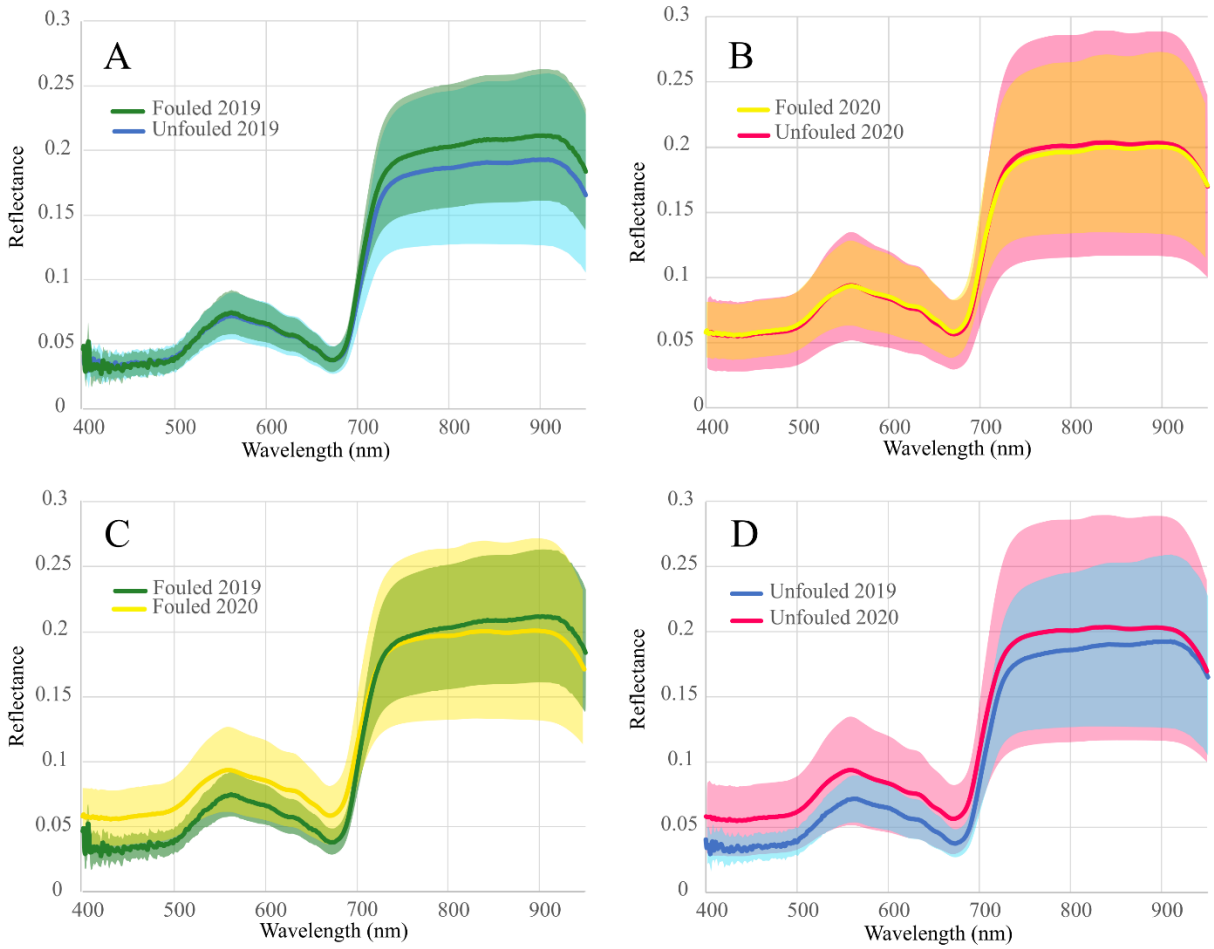

Figure SM3.2. Effect of fouling and season on the average spectral response and spectral variability of *Chara* sp. The average spectrum is shown as a solid line, with ± one standard deviation shaded. A) Effect of fouling, peak-growing season. B) Effect of fouling, late season. C) Effect of seasonality, fouled samples. D) Effect of seasonality, unfouled samples. While *Chara* sp. is shown as an example, the same pattern was found for all species.

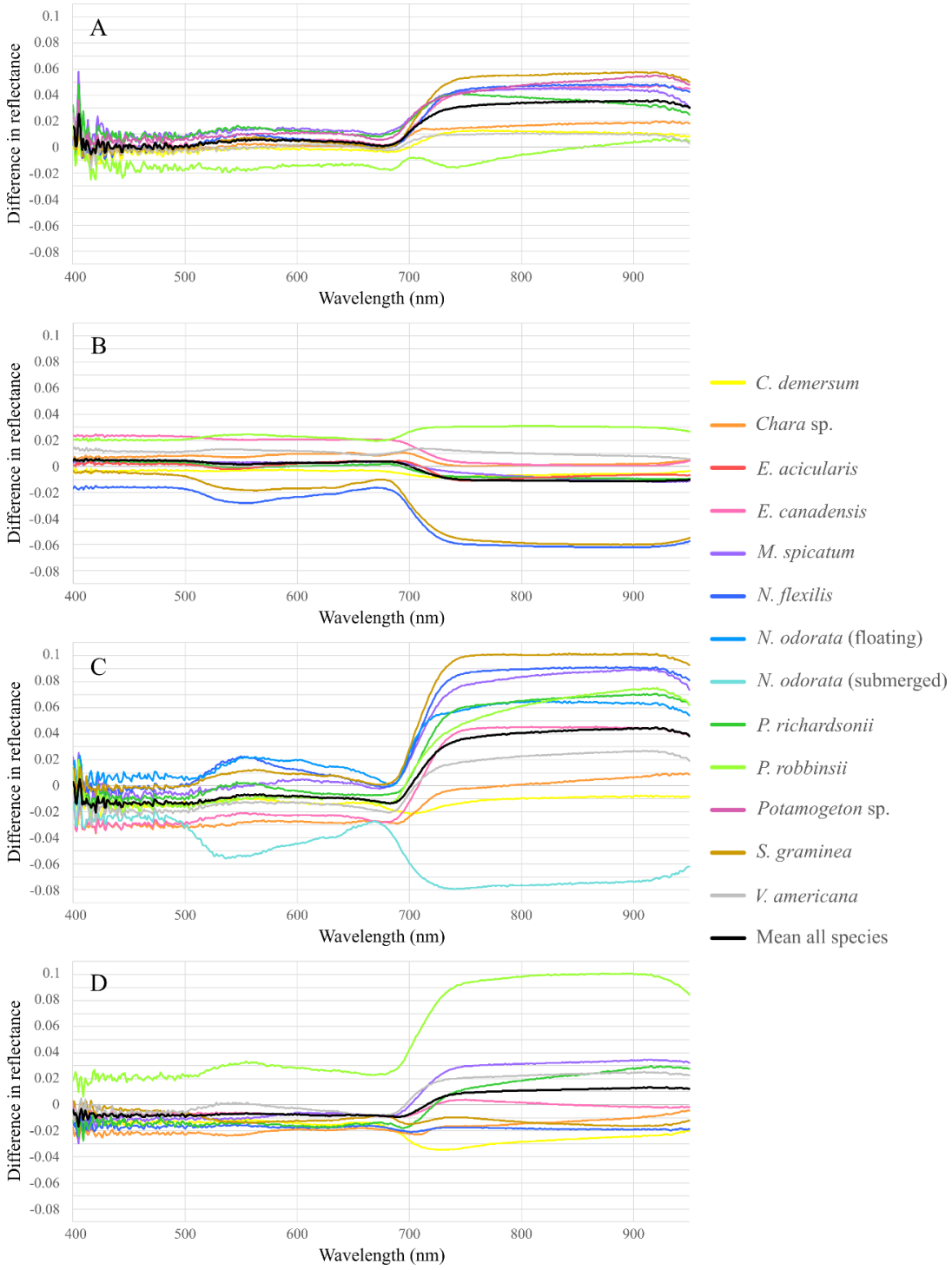

Figure SM3.3. Effect of fouling and season, shown as difference in mean spectra. The average change across all species is shown in black on both plots. A) peak season, fouled minus unfouled, B) late season, fouled minus unfouled, C) fouled, peak season minus late season, D) unfouled, peak season minus late season. Only species that were measured in both fouled and unfouled states and in both seasons are shown in panels A) and B) and panels C) and D), respectively.

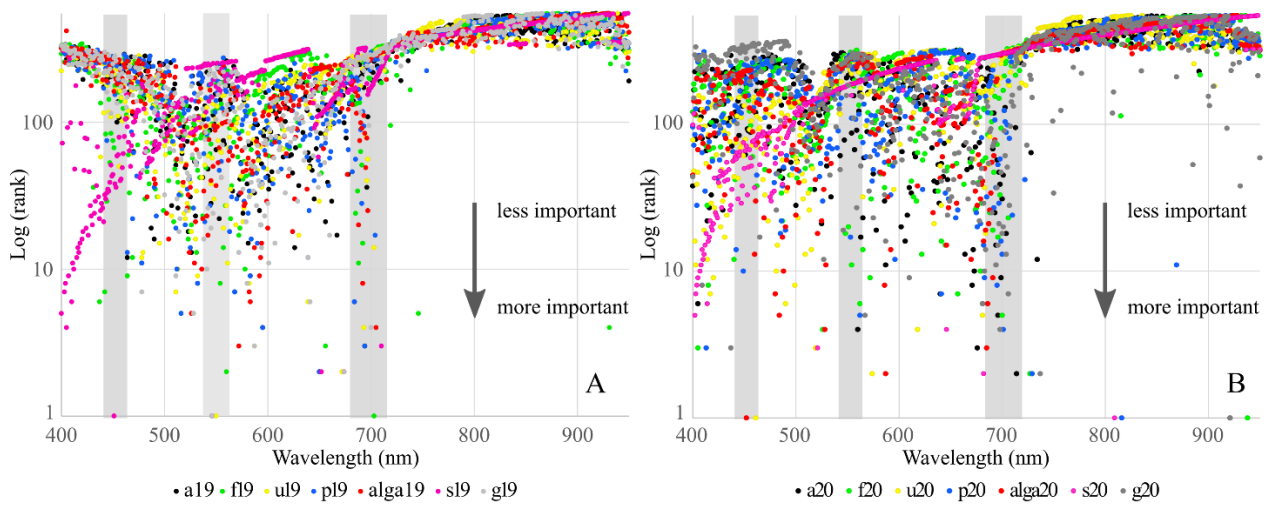

Figure SM3.4. Band rankings from the forward feature selection. The wavelengths of each band from the ASD spectra are ranked in descending order according to contribution to separability (i.e., a ranking of 1 indicates the most important contributor to separability for that dataset). The grey bars highlight three regions of notable green vegetation spectral features: the total pigment absorption feature (~ 450 nm), the Chl-a absorptance feature (~550 nm), and the red-edge (~ 700 nm). The Y-axis has been log-transformed to facilitate interpretation.

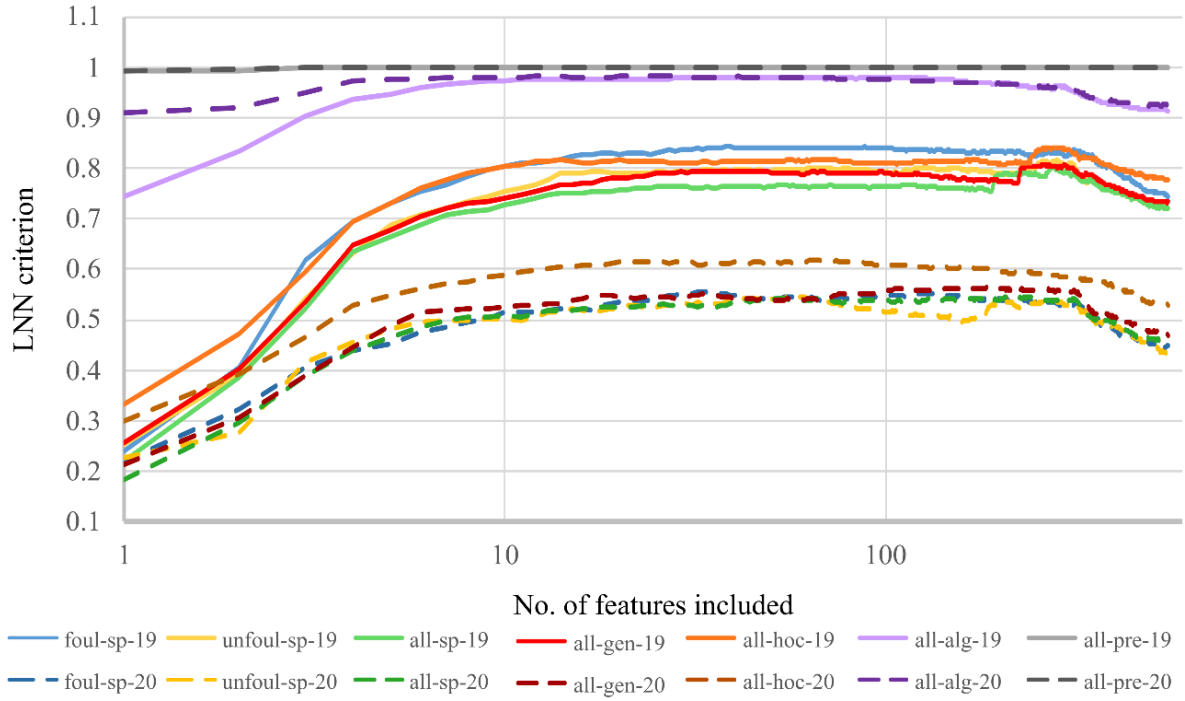

Figure SM3.5. Results from the forward feature selection (FFS) from all datasets (original ASD spectra). The X-axis has been log-transformed to facilitate interpretation.

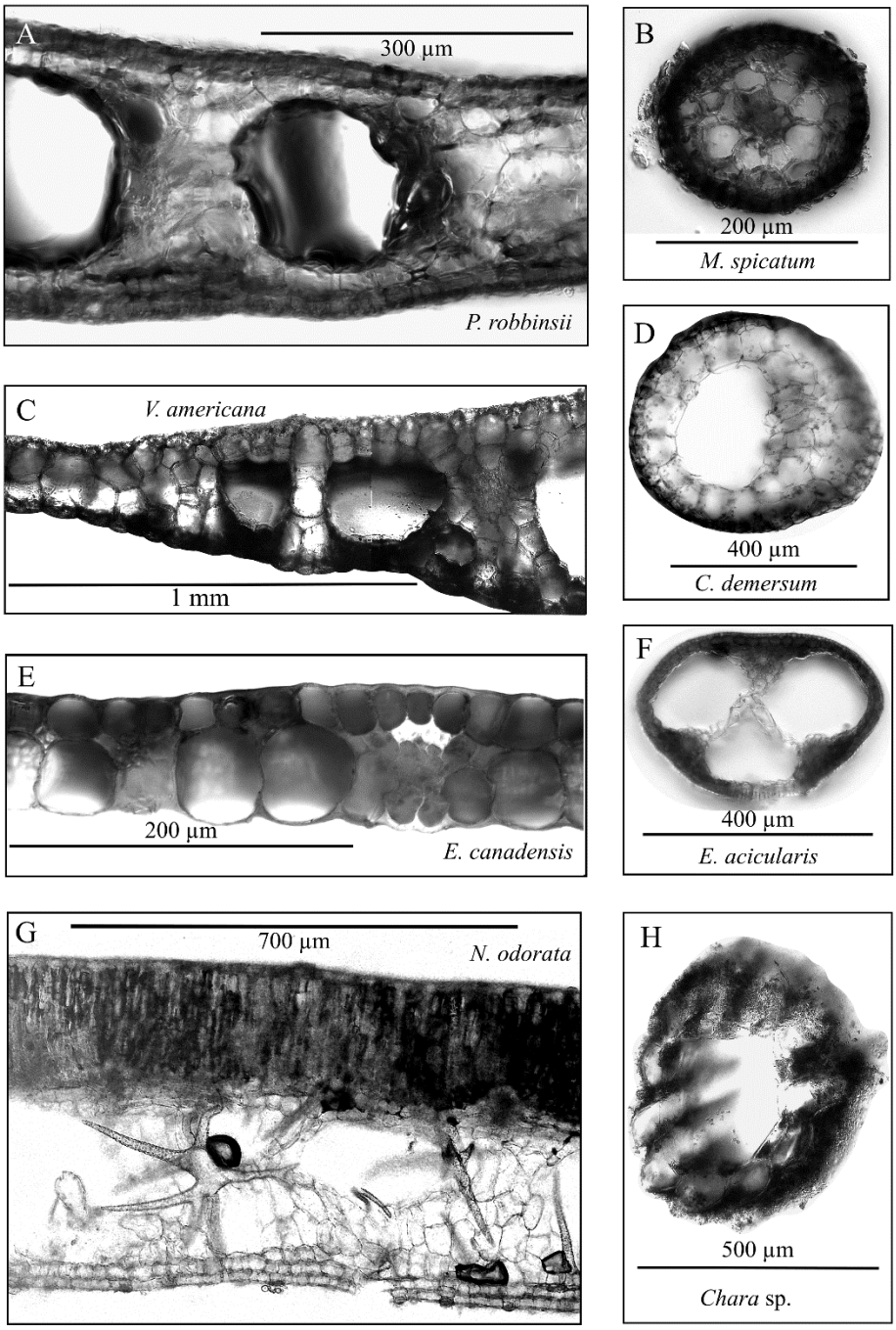

Figure SM3.6. Microscopy photographs of leaf cross sections of submerged plants, a floating plant and a macroalgae. Similarities (i.e., no air spaces between mesophyll cells; large lacunae within the mesophyll; single layer of epidermal cells; no stomata) in leaf structure across six genera of vascular SAV found at the site (**A-F**) contrast the complexity of leaf structure in floating leaves (i.e., columnar mesophyll, spongy mesophyll, defined epidermal cell layers, etc.) (**G**). The macroalgae lacks all internal structure (**H**). (**A**) *P. robbinsii.* (**B**) *M. spicatum.* (**C**) *V. americana*. (**D**) *C. demersum*. (**E**) *E. canadensis*. (**F**) *E. acicularis*. (**G**) *N. Odorata.* (**H**) *Chara* sp.

4. Conclusions

4.1. Summary of findings

A comprehensive resource for non-specialists was created to advise researchers from other fields on the theory and considerations involved in applying remote sensing to the aquatic environment. All aspects of a typical remote sensing workflow were presented with explicit mentions of how these steps might look or vary when dealing with aquatic subjects like SAV. Additionally, previous work in mapping SAV and recent innovations in the field were discussed. Most past studies examining SAV were restricted to marine environments where the water is clear and shallow and aimed to detect either community-level extent or large monospecific stands; these broad classes thus limited the specificity of the questions that could be addressed. Using hyperspectral data (either leaf-level or imagery) has provided increasingly more accurate study results and is opening new potential research avenues. Researchers must however be cognizant of their research design, particularly as it relates to water column compensation methodology, as no single method is best for all conditions, nor does there exist a structured framework to guide such decisions. Methods may also be better suited to one sensor or platform over another (e.g., NDVI was developed for use with Landsat, Structure from Motion would not be effective with satellite or coarse resolution airborne imagery, etc.). There have been many major recent investments in technological innovations intended for use in aquatic settings both in terms of sensors and processing methods. As the available data becomes better suited to the aquatic environment, and there are more powerful compensation and analytic methods well-suited to remote sensing over water, the potential scope of applications and the possible mapping accuracy of those applications are constantly growing.

In examining the spectral separability of a set of freshwater SAV, the vegetation was found to be sufficiently separable using hyperspectral data to suggest that accurate mapping could be achieved. Resampling the hyperspectral data to simulate the responses of multispectral satellite sensors however dramatically reduced how spectrally distinct the vegetation was. The choice of sampling season was also an influential determinant of the spectral separability, with classes being less distinct at the end of the growing season than at its peak. Researchers should thus aim to deploy high spectral resolution sensors at the peak of the SAV growing season to maximize the likelihood of producing accurate results. In situ target detection of SAV produced

acceptably high overall recall results, both when detecting single types of vegetation (88%) and when detecting for broad vegetation or non-vegetation classes (94%). The classes targeted in imagery were however limited to those occurring in patches of similar size as the spatial resolution of the imagery. This exemplifies one of the major limitations remaining to be addressed before remote sensing can be fully leveraged in aquatic studies: the targets of interest are often too small to be detectable in pixels of the spatial resolution that is currently available from satellite platforms. Researchers involved in future developments of sensors specifically for application in aquatic ecosystems should therefore prioritize appropriate band placement and fine spatial resolution over a high number of contiguous bands. Novel processing methods, such as those used here, are additionally widening the range of water types to which optical remote sensing can be applied. Once suitable data and appropriate processing methods are available, aquatic targets such as SAV are expected to be amenable to mapping from the local to global scale.

4.2. Future directions

While this thesis addressed some of the major knowledge gaps existing in aquatic remote sensing, a substantial amount of work remains to be done to make the discipline both well suited and easily implemented to aquatic environments for ecosystem monitoring.

Firstly, work must be done to remove the elements of trial and error and ambiguity when it comes to water column characterization and compensation. It is understandable that many systems have been developed to characterize water according to its characteristics, constituents, or optical properties (e.g., [8,352,382-384]). The numerous competing systems are however not all easily applicable nor meaningful in remote sensing, and there are no equivalency guidelines. The creation of a single system would allow standardization across the field. Synthesizing the results of past work to identify trends in the application and suitability of various water column compensation processes would assist in guiding future practitioners in selecting the most appropriate analytic methods. The combination of a standardized water type classification scheme and a thorough examination of the strengths and limitations of water column compensations in each water type would facilitate future research and ensure that results across different studies could be compared. Once the water column can be satisfactorily compensated

for across water types, SAV could more easily be monitored using remote sensing across regions and scales.

Secondly, as turbid waters have largely been avoided in past research, the effect of turbidity has not been comprehensively examined. SAV does indeed grow in turbid, or optically deep, waters, thus the presence of vegetation should not be used as an indicator that a water body would be well-suited to remote sensing. Rather, the combination of depth and turbidity itself must be considered. As turbidity varies in composition and intensity over space and time, defining the effect of turbidity could help interpret images collected over unideal water conditions; determining the maximum turbidity level possible while information is still extractable from imagery would guide researchers as to when remote sensing campaigns are worth investing in.

Thirdly, there remains much to be studied relating to the spectral properties of aquatic targets like SAV. As mentioned previously, research concentrating on determining the effect of fouling as a function of its abundance should be conducted to define the boundary of which ecosystems remote sensing should be applied to. Additionally, the in-situ mapping conducted here was limited to targets of similar spatial extent as the imagery pixels, but it did not quantitatively examine the effect of sub-pixel target size on detection rate. The minimum spatial extent for an aquatic target to be detected in imagery of a given resolution should therefore be investigated to comprehensively define the scope of research questions that can be addressed using remote sensing.

Fourthly, a 99% reflectance Spectralon panel was here used to examine the effect of water across depths under the assumption that the panel's own reflectivity remained unchanged. This has not been established and was beyond the scope of this work. The suitability of Spectralon panels for underwater operations should be investigated to determine if they can be used as appropriate targets for training and validation of empiric water column compensation methodologies.

Finally, a comprehensive resource was created in this thesis to guide non-specialists who are interested in exploring or implementing remote sensing. While this will hopefully facilitate their adoption of remote sensing, the fast-moving pace of the discipline and constant innovation mean that resources such as this must constantly be updated to remain useful. Remote sensing

experts in general, and those studying aquatic applications specifically, must therefore share their effort between advancing the field and exchanging knowledge with users from aquatic, biological and ecological specialities. Technological innovations are indeed needed and strongly desired, but the value in ensuring that there are others prepared to leverage those innovations into meaningful results can not be understated.

References

1. Rowan, G.S.L.; Kalacska, M. Determining the spectral separability of freshwater submerged aquatic vegetation of the St. Lawrence River. In Proceedings of 42nd Canadian Symposium on Remote Sensing, Virtual., June 21-25 2021.
2. Maasri, A.; Jähnig, S.C.; Adamescu, M.C.; Adrian, R.; Baigun, C.; Baird, D.; Kohlmann, B.; Kuemmerlen, M.; Kuiper, J.; Kupilas, B., et al. A Global Agenda for Advancing Freshwater Biodiversity Research. *EcoEvoRxiv [Preprint]* **2021**, 10.32942/osf.io/4pg7f, doi:10.32942/osf.io/4pg7f.
3. Tyberghein, L.; Verbruggen, H.; Pauly, K.; Troupin, C.; Mineur, F.; De Clerck, O. Bio-ORACLE: a global environmental dataset for marine species distribution modelling. *Global Ecology and Biogeography* **2012**, *21*, 272-281, doi:https://doi.org/10.1111/j.1466-8238.2011.00656.x.
4. Duffy, J.E.; Benedetti-Cecchi, L.; Trinanes, J.; Muller-Karger, F.E.; Ambo-Rappe, R.; Bostrom, C.; Buschmann, A.H.; Byrnes, J.; Coles, R.G.; Creed, J., et al. Toward a Coordinated Global Observing System for Seagrasses and Marine Macroalgae. *Frontiers in Marine Science* **2019**, *6*, doi:10.3389/fmars.2019.00317.
5. United Nations Environment Programme. *Out of the blue: The value of seagrasses to the environment and to people*; UNEP: Nairobi, 2020.
6. Dierssen, H.M.; Ackleson, S.G.; Joyce, K.E.; Hestir, E.L.; Castagna, A.; Lavender, S.; McManus, M.A. Living up to the Hype of Hyperspectral Aquatic Remote Sensing: Science, Resources and Outlook. *Frontiers in Environmental Science* **2021**, *9*, doi:10.3389/fenvs.2021.649528.
7. Farster, B.; Huynh, Q.; Messinger, D.; Middleton, C.; Resmini, R.G. Panel: How to meet the need for spectral expertise. In *Spectral Sessions*, Schmidt, J., Ed. L3Harris: 2021.
8. Kirk, J.T.O. Spectral Absorption Properties of Natural Waters: Contribution of the Soluble and Particulate Fractions to Light Absorption in some Inland Waters of South-eastern Australia. *Australian Journal of Marine and Freshwater Research* **1980**, *31*, 287-296, doi:10.1111/j.1365-2427.1986.tb01001.x.
9. Cetinić, I.; McClain, C.R.; Werdell, P.J. PACE Technical Report Series. Center, G.S.F., Ed. Greenbelt, Maryland, 2018; Vol. 5.
10. ESA Climate Office. Ocean Colour. Availabe online: https://climate.esa.int/en/projects/ocean-colour/ (accessed on August 02 2021).
11. Jia, Q.; Cao, L.; Yésou, H.; Huber, C.; Fox, A.D. Combating aggressive macrophyte encroachment on a typical Yangtze River lake: lessons from a long-term remote sensing study of vegetation. *Aquatic Ecology* **2017**, *51*, 177-189, doi:10.1007/s10452-016-9609-9.
12. Shinkareva, G.L.; Lychagin, M.Y.; Tarasov, M.K.; Pietroń, J.; Chichaeva, M.A.; R.chalov, S. Biogeochemical specialization of macrophytes and their role as a biofilter in the selenga delta. *Geography, Environment, Sustainability* **2019**, *12*, 240-263, doi:10.24057/2071-9388-2019-103.
13. Massicotte, P.; Bertolo, A.; Brodeur, P.; Hudon, C.; Mingelbier, M.; Magnan, P. Influence of the aquatic vegetation landscape on larval fish abundance. *Journal of Great Lakes Research* **2015**, *41*, 873-880, doi:10.1016/j.jglr.2015.05.010.
14. Hughes, A.R.; Williams, S.L.; Duarte, C.M.; Heck Jr, K.L.; Waycott, M. Associations of concern: declining seagrasses and threatened dependent species. *Frontiers in Ecology and the Environment* **2009**, *7*, 242-246, doi:10.1890/080041.

15. Hestir, E.L.; Schoellhamer, D.H.; Greenberg, J.; Morgan-King, T.; Ustin, S.L. The Effect of Submerged Aquatic Vegetation Expansion on a Declining Turbidity Trend in the Sacramento-San Joaquin River Delta. *Estuaries and Coasts* **2016**, *39*, 1100-1112, doi:10.1007/s12237-015-0055-z.
16. Wolter, P.T.; Johnston, C.A.; Niemi, G.J. Mapping submergent aquatic vegetation in the US Great Lakes using Quickbird satellite data. *International Journal of Remote Sensing* **2005**, *26*, 5255-5274, doi:10.1080/01431160500219208.
17. Malthus, T.J. Bio-optical Modeling and Remote Sensing of Aquatic Macrophytes. In *Bio-optical Modeling and Remote Sensing of Inland Waters*, 2017; 10.1016/B978-0-12-804644-9.00009-4pp. 263-308.
18. Silva, T.S.F.; Costa, M.P.F.; Melack, J.M.; Novo, E.M.L.M. Remote sensing of aquatic vegetation: Theory and applications. *Environmental Monitoring and Assessment* **2008**, *140*, 131-145, doi:10.1007/s10661-007-9855-3.
19. Zhang, Y.L.; Jeppesen, E.; Liu, X.H.; Qin, B.Q.; Shi, K.; Zhou, Y.Q.; Thomaz, S.M.; Deng, J.M. Global loss of aquatic vegetation in lakes. *Earth-Science Reviews* **2017**, *173*, 259-265, doi:10.1016/j.earscirev.2017.08.013.
20. Mcleod, E.; Chmura, G.L.; Bouillon, S.; Salm, R.; Björk, M.; Duarte, C.M.; Lovelock, C.E.; Schlesinger, W.H.; Silliman, B.R. A blueprint for blue carbon: toward an improved understanding of the role of vegetated coastal habitats in sequestering CO2. *Frontiers in Ecology and the Environment* **2011**, *9*, 552-560, doi:10.1890/110004.
21. Bostater, C.R.; Ghir, T.; Bassetti, L.; Hall, C.; Reyier, E.; Lowers, R.; Holloway-Adkins, K.; Virnstein, R. Hyperspectral Remote Sensing Protocol Development for Submerged Aquatic Vegetation in Shallow Water. In Proceedings of Proceedings of SPIE - The International Society for Optical Engineering, Barcelona, Spain, 8 -12 September 2003; pp. 199-215.
22. Ackleson, S.G.; Klemas, V. Remote sensing of submerged aquatic vegetation in lower chesapeake bay: A comparison of Landsat MSS to TM imagery. *Remote Sensing of Environment* **1987**, *22*, 235-248, doi:https://doi.org/10.1016/0034-4257(87)90060-5.
23. O'Neill, J.D.; Costa, M. Mapping eelgrass (Zostera marina) in the Gulf Islands National Park Reserve of Canada using high spatial resolution satellite and airborne imagery. *Remote Sensing of Environment* **2013**, *133*, 152-167, doi:10.1016/j.rse.2013.02.010.
24. Vis, C.; Hudon, C.; Carignan, R. An evaluation of approaches used to determine the distribution and biomass of emergent and submerged aquatic macrophytes over large spatial scales. *Aquatic Botany* **2003**, *77*, 187-201, doi:10.1016/S0304-3770(03)00105-0.
25. He, K.S.; Bradley, B.A.; Cord, A.F.; Rocchini, D.; Tuanmu, M.N.; Schmidtlein, S.; Turner, W.; Wegmann, M.; Pettorelli, N. Will remote sensing shape the next generation of species distribution models? *Remote Sensing in Ecology and Conservation* **2015**, *1*, 4-18, doi:10.1002/rse2.7.
26. Visser, F.; Wallis, C.; Sinnott, A.M. Optical remote sensing of submerged aquatic vegetation: Opportunities for shallow clearwater streams. *Limnologica* **2013**, *43*, 388-398, doi:10.1016/j.limno.2013.05.005.
27. Saravia, L.A.; Giorgi, A.; Momo, F.R. A photographic method for estimating chlorophyll in periphyton on artificial substrata. *Aquatic Ecology* **1999**, *33*, 325-330, doi:10.1023/A:1009934626188.

28. Free, G.; Bresciani, M.; Trodd, W.; Tierney, D.; O'Boyle, S.; Plant, C.; Deakin, J. Estimation of lake ecological quality from Sentinel-2 remote sensing imagery. *Hydrobiologia* **2020**, *847*, 1423-1438, doi:10.1007/s10750-020-04197-y.
29. Costa, V.; Serôdio, J.; Lillebø, A.I.; Sousa, A.I. Use of hyperspectral reflectance to non-destructively estimate seagrass Zostera noltei biomass. *Ecological Indicators* **2021**, *121*, doi:10.1016/j.ecolind.2020.107018.
30. Ashraf, S.; Brabyn, L.; Hicks, B.J.; Collier, K. Satellite remote sensing for mapping vegetation in New Zealand freshwater environments: A review. *New Zealand Geographer* **2010**, *66*, 33-43, doi:10.1111/j.1745-7939.2010.01168.x.
31. Kalacska, M.; Chmura, G.L.; Lucanus, O.; Bérubé, D.; Arroyo-Mora, J.P. Structure from motion will revolutionize analyses of tidal wetland landscapes. *Remote Sensing of Environment* **2017**, *199*, 14-24, doi:https://doi.org/10.1016/j.rse.2017.06.023.
32. Rhee, D.S.; Do Kim, Y.; Kang, B.; Kim, D. Applications of unmanned aerial vehicles in fluvial remote sensing: An overview of recent achievements. *KSCE Journal of Civil Engineering* **2018**, *22*, 588-602, doi:10.1007/s12205-017-1862-5.
33. Klemas, V. Remote Sensing of Submerged Aquatic Vegetation. In *Seafloor Mapping Along Continental Shelves: Research and Techniques for Visualizing Benthic Environments*, Finkl, C.W., Makowski, C., Eds. Springer International Publishing: Cham, Switzerland, 2016; Vol. 13, pp. 125-140.
34. Palmer, S.C.J.; Kutser, T.; Hunter, P.D. Remote sensing of inland waters: Challenges, progress and future directions. *Remote Sensing of Environment* **2015**, *157*, 1-8, doi:10.1016/j.rse.2014.09.021.
35. Linchant, J.; Lisein, J.; Semeki, J.; Lejeune, P.; Vermeulen, C. Are unmanned aircraft systems (UASs) the future of wildlife monitoring? A review of accomplishments and challenges. *Mammal Review* **2015**, *45*, 239-252.
36. Anderson, K.; Gaston, K.J. Lightweight unmmaned aerial vehicles will revolutionize spatial ecology. *Frontiers in Ecology and the Environment* **2013**, *11*, 138-146.
37. Brando, V.E.; Phinn, S.R. Coastal Aquatic Remote Sensing Applications for Environmental Monitoring and Management. *Journal of Applied Remote Sensing* **2007**, *1*, doi:10.1117/1.2835115.
38. Visser, F.; Buis, K.; Verschoren, V.; Schoelynck, J. Mapping of submerged aquatic vegetation in rivers from very high-resolution image data, using object-based image analysis combined with expert knowledge. *Hydrobiologia* **2018**, *812*, 157-175, doi:10.1007/s10750-016-2928-y.
39. Dörnhöfer, K.; Oppelt, N. Remote sensing for lake research and monitoring - Recent advances. *Ecological Indicators* **2016**, *64*, 105-122, doi:10.1016/j.ecolind.2015.12.009.
40. Nelson, S.A.C.; Cheruvelil, K.S.; Soranno, P.A. Satellite remote sensing of freshwater macrophytes and the influence of water clarity. *Aquatic Botany* **2006**, *85*, 289-298, doi:10.1016/j.aquabot.2006.06.003.
41. Stocks, J.R.; Rodgers, M.P.; Pera, J.B.; Gilligan, D.M. Monitoring aquatic plants: An evaluation of hydroacoustic, on-site digitising and airborne remote sensing techniques. *Knowledge and Management of Aquatic Ecosystems* **2019**, 10.1051/kmae/2019016, doi:10.1051/kmae/2019016.
42. Hossain, M.S.; Bujang, J.S.; Zakaria, M.H.; Hashim, M. The application of remote sensing to seagrass ecosystems: an overview and future research prospects. *International Journal of Remote Sensing* **2015**, *36*, 61-114, doi:10.1080/01431161.2014.990649.

43. Collin, A.; Ramambason, C.; Thiault, L.; Nakamura, N.; Pastol, Y.; Casella, E.; Rovere, A.; Espiau, B.; Siu, G.; Lerouvreur, F., et al. Very high resolution mapping of coral reef state using airborne bathymetric lidar surface-intensity and drone imagery. *International Journal of Remote Sensing* **2018**, *39*, 5676-5688, doi:10.1080/01431161.2018.1500072.
44. Giardino, C.; Brando, V.E.; Gege, P.; Pinnel, N.; Hochberg, E.; Knaeps, E.; Reusen, I.; Doerffer, R.; Bresciani, M.; Braga, F., et al. Imaging Spectrometry of Inland and Coastal Waters: State of the Art, Achievements and Perspectives. *Surveys in Geophysics* **2019**, *40*, 401-429, doi:10.1007/s10712-018-9476-0.
45. Pu, R.; Bell, S. Mapping seagrass coverage and spatial patterns with high spatial resolution IKONOS imagery. *International Journal of Applied Earth Observation and Geoinformation* **2017**, *54*, 145-158, doi:10.1016/j.jag.2016.09.011.
46. Wolf, P.; Rößler, S.; Schneider, T.; Melzer, A. Collecting in situ remote sensing reflectances of submersed macrophytes to build up a spectral library for lake monitoring. *European Journal of Remote Sensing* **2013**, *46*, 401-416, doi:10.5721/EuJRS20134623.
47. Markham, B.L.; Arvidson, T.; Barsi, J.A.; Choate, M.; Kaita, E.; Levy, R.; Lubke, M.; Masek, J.G. 1.03 - Landsat Program. In *Comprehensive Remote Sensing*, Liang, S., Ed. Elsevier: Oxford, 2018; https://doi.org/10.1016/B978-0-12-409548-9.10313-6pp. 27-90.
48. Planet. Planet Imagery Product Specifications. Availabe online: https://assets.planet.com/docs/Planet_Combined_Imagery_Product_Specs_letter_screen.pdf (accessed on February 7th 2020).
49. Klemas, V. Remote Sensing Techniques for Studying Coastal Ecosystems: An Overview. *Journal of Coastal Research* **2011**, *27*, 2-17, doi:10.2112/jcoastres-d-10-00103.1.
50. Kirk, J.T.O. *Light and photosynthesis in aquatic ecosystems.*, Second ed.; Cambridge University Press: Cambridge, Great Britain, 1994; pp. 509.
51. Seyhan, E.; Dekker, A. Application of remote sensing techniques for water quality monitoring. *Hydrobiological Bulletin* **1986**, *20*, 41-50, doi:10.1007/BF02291149.
52. Davie, A.; Hartmann, K.; Timms, G.; De Groot, M.; McCulloch, J. Benthic habitat mapping with autonomous underwater vehicles. In Proceedings of OCEANS 2008, Quebec City, Canada.
53. Bale, A.J.; Tocher, M.D.; Weaver, R.; Hudson, S.J.; Aiken, J. Laboratory measurements of the spectral properties of estuarine suspended particles. *Netherland Journal of Aquatic Ecology* **1994**, *28*, 237-244, doi:10.1007/BF02334190.
54. Han, L.; Rundquist, D.C. The spectral responses of Ceratophyllum demersum at varying depths in an experimental tank. *International Journal of Remote Sensing* **2003**, *24*, 859-864, doi:10.1080/0143116021000009868.
55. Chirayath, V.; Earle, S.A. Drones that see through waves – preliminary results from airborne fluid lensing for centimetre-scale aquatic conservation. *Aquatic Conservation: Marine and Freshwater Ecosystems* **2016**, *26*, 237-250, doi:10.1002/aqc.2654.
56. Kislik, C.; Genzoli, L.; Lyons, A.; Kelly, M. Application of UAV imagery to detect and quantify submerged filamentous algae and rooted macrophytes in a non-wadeable river. *Remote Sensing* **2020**, *12*, 1-24, doi:10.3390/rs12203332.
57. Gates, D.M.; Keegan, H.J.; Schleter, J.C.; Weidner, V.R. Spectral Properties of Plants. *Applied Optics* **1965**, *4*, 11-20.
58. Fyfe, S.K. Spatial and temporal variation in spectral reflectance: Are seagrass species spectrally distinct? *Limnology and Oceanography* **2003**, *48*, 464-479, doi: 10.4319/lo.2003.48.1_part_2.0464.

59. Cho, H.J. Depth-variant spectral characteristics of submersed aquatic vegetation detected by Landsat 7 ETM+. *International Journal of Remote Sensing* **2007**, *28*, 1455-1467, doi:10.1080/01431160600962772.
60. Haghi Vayghan, A.; Poorbagher, H.; Taheri Shahraiyni, H.; Fazli, H.; Nasrollahzadeh Saravi, H. Suitability indices and habitat suitability index model of Caspian kutum (Rutilus frisii kutum) in the southern Caspian Sea. *Aquatic Ecology* **2013**, *47*, 441-451, doi:10.1007/s10452-013-9457-9.
61. Purkis, S.J.; Graham, N.A.J.; Riegl, B.M. Predictability of reef fish diversity and abundance using remote sensing data in Diego Garcia (Chagos Archipelago). *Coral Reefs* **2008**, *27*, 167-178, doi:10.1007/s00338-007-0306-y.
62. Rotta, L.H.S.; Mishra, D.R.; Watanabe, F.S.Y.; Rodrigues, T.W.P.; Alcântara, E.H.; Imai, N.N. Analyzing the feasibility of a space-borne sensor (SPOT-6) to estimate the height of submerged aquatic vegetation (SAV) in inland waters. *ISPRS Journal of Photogrammetry and Remote Sensing* **2018**, *144*, 341-356, doi:10.1016/j.isprsjprs.2018.07.011.
63. Gao, Y.; Li, Q.; Wang, S.; Gao, J. Adaptive neural network based on segmented particle swarm optimization for remote-sensing estimations of vegetation biomass. *Remote Sensing of Environment* **2018**, *211*, 248-260, doi:10.1016/j.rse.2018.04.026.
64. Rotta, L.H.; Mishra, D.R.; Alcântara, E.; Imai, N.; Watanabe, F.; Rodrigues, T. K <inf>d(PAR)</inf> and a depth based model to estimate the height of submerged aquatic vegetation in an oligotrophic reservoir: A case study at Nova Avanhandava. *Remote Sensing* **2019**, *11*, doi:10.3390/rs11030317.
65. Hall, C.R.; Bostater, C.R.; Virnstein, R.W. Implementation of a ground truth process for development of a submerged aquatic vegetation (SAV) mapping protocol using hyperspectral imagery. *Remote Sensing of the Ocean, Sea Ice, and Large Water Regions* **2006**, *6360*, doi:10.1117/12.692354.
66. Hugue, F.; Lapointe, M.; Eaton, B.C.; Lepoutre, A. Satellite-based remote sensing of running water habitats at large riverscape scales: Tools to analyze habitat heterogeneity for river ecosystem management. *Geomorphology* **2016**, *253*, 353-369, doi:https://doi.org/10.1016/j.geomorph.2015.10.025.
67. Lee, Z.; Carder, K.L.; Chen, R.F.; Peacock, T.G. Properties of the water column and bottom derived from Airborne Visible Infrared Imaging Spectrometer (AVIRIS) data. *Journal of Geophysical Research: Oceans* **2001**, *106*, 11639-11651, doi:https://doi.org/10.1029/2000JC000554.
68. Giardino, C.; Candiani, G.; Bresciani, M.; Lee, Z.; Gagliano, S.; Pepe, M. BOMBER: A tool for estimating water quality and bottom properties from remote sensing images. *Computers & Geosciences* **2012**, *45*, 313-318, doi:https://doi.org/10.1016/j.cageo.2011.11.022.
69. Hudon, C.; Lalonde, S.; Gagnon, P. Ranking the effects of site exposure, plant growth form, water depth, and transparency on aquatic plant biomass. *Canadian Journal of Fisheries and Aquatic Sciences* **2000**, *57*, 31-42, doi:10.1139/f99-232.
70. Hill, V.J.; Zimmerman, R.C.; Bissett, W.P.; Dierssen, H.; Kohler, D.D.R. Evaluating Light Availability, Seagrass Biomass, and Productivity Using Hyperspectral Airborne Remote Sensing in Saint Joseph's Bay, Florida. *Estuaries and Coasts* **2014**, *37*, 1467-1489, doi:10.1007/s12237-013-9764-3.

71. Klemas, V. Remote Sensing of Emergent and Submerged Wetlands: An Overview. *International Journal of Remote Sensing* **2013**, *34*, 6286-6320, doi:10.1080/01431161.2013.800656.
72. Wedding, L.M.; Friedlander, A.M.; McGranaghan, M.; Yost, R.S.; Monaco, M.E. Using bathymetric lidar to define nearshore benthic habitat complexity: Implications for management of reef fish assemblages in Hawaii. *Remote Sensing of Environment* **2008**, *112*, 4159-4165, doi:https://doi.org/10.1016/j.rse.2008.01.025.
73. Costa, M.P.F.; Niemann, O.; Novo, E.; Ahern, F. Biophysical properties and mapping of aquatic vegetation during the hydrological cycle of the Amazon floodplain using JERS-1 and Radarsat. *International Journal of Remote Sensing* **2002**, *23*, 1401-1426, doi:10.1080/01431160110092957.
74. Idzanovic, M.; Ophaug, V.; Andersen, O.B. Coastal sea-level in Norway from CryoSat-2 SAR altimetry. *Advances in Space Research* **2018**, *62*, doi:https://doi.org/10.1016/j.asr.2017.07.043.
75. Wilson, B.A.; Rashid, H. Monitoring the 1997 flood in the Red River Valley using hydrologic regimes and RADARSAT imagery. *Canadian Geographer* **2005**, *49*, 100-109, doi:10.1111/j.0008-3658.2005.00082.x.
76. Dwivedi, R.S.; Rao, B.R.M.; Bhattacharya, S. Mapping wetlands of the Sundaban Delta and it's environs using ERS-1 SAR data. *International Journal of Remote Sensing* **1999**, *20*, 2235-2247.
77. Greene, A.; Rahman, A.F.; Kline, R.; Rahman, M.S. Side scan sonar: A cost-efficient alternative method for measuring seagrass cover in shallow environments. *Estuarine, Coastal and Shelf Science* **2018**, *207*, 250-258, doi:10.1016/j.ecss.2018.04.017.
78. Ford, K.H.; Voss, S.; Evans, N.T. Reproducibility, Precision, and Accuracy of a Hydroacoustic Method to Estimate Seagrass Canopy Height and Percent Cover in Massachusetts. *Estuaries and Coasts* **2019**, 10.1007/s12237-019-00618-x, doi:10.1007/s12237-019-00618-x.
79. Aasen, H.; Honkavaara, E.; Lucieer, A.; Zarco-Tejada, P.J. Quantitative Remote Sensing at Ultra-High Resolution with UAV Spectroscopy: A Review of Sensor Technology, Measurement Procedures, and Data Correction Workflows. *Remote Sensing* **2018**, *10*, 1091.
80. Cubert GmbH. Cubert Hyperspectral Video Cameras. Availabe online: https://cubert-gmbh.com/cubert-spectral-cameras/ (accessed on July 14 2020).
81. Madden, M. Remote sensing and geographic information system operations for vegetation mapping of invasive exotics. *Weed Technology* **2004**, *18*, 1457-1463, doi:10.1614/0890-037x(2004)018[1457:Rsagis]2.0.Co;2.
82. Valta-Hulkkonen, K.; Kanninen, A.; Ilvonen, R.; Leka, J. Assessment of aerial photography as a method for monitoring aquatic vegetation in lakes of varying trophic status. *Boreal Environment Research* **2005**, *10*, 57-66.
83. Flynn, K.F.; Chapra, S.C. Remote sensing of submerged aquatic vegetation in a shallow non-turbid river using an unmanned aerial vehicle. *Remote Sensing* **2014**, *6*, 12815-12836, doi:10.3390/rs61212815.
84. Jallad, A.-H.; Marpu, P.; Abdul Aziz, Z.; Al Marar, A.; Awad, M. MeznSat—A 3U CubeSat for Monitoring Greenhouse Gases Using Short Wave Infra-Red Spectrometry: Mission Concept and Analysis. *Aerospace* **2019**, *6*, 118, doi:10.3390/aerospace6110118.

85. Byfield, V. Optical remote sensing of marine, coastal, and inland waters. In *Handbook of Optoelectronics, Second Edition: Applied Optical Electronics Volume Three*, CRC Press: Boca Raton, USA, 2017; 10.1201/b22316pp. 103-114.
86. Tatem, A.J.; Goetz, S.J.; Hay, S.I. Fifty Years of Earth-observation Satellites. Availabe online: https://www.americanscientist.org/article/fifty-years-of-earth-observation-satellites (accessed on May 23rd 2020).
87. McIlwaine, B.; Casado, M.R.; Leinster, P. Using 1st Derivative Reflectance Signatures within a Remote Sensing Framework to Identify Macroalgae in Marine Environments. *Remote Sensing* **2019**, *11*, doi:10.3390/rs11060704.
88. TriOS. RAMSES. Availabe online: https://www.trios.de/en/ramses.html (accessed on November 24 2020).
89. Panalytical, M. ASD Range. Availabe online: https://www.malvernpanalytical.com/en/products/product-range/asd-range (accessed on March 20 2020).
90. Spectra Vista Corporation. HR-640i - High Resolution Field Portable Spectroradiometer. Availabe online: https://www.spectravista.com/our-instruments/hr-640i/ (accessed on March 20 2020).
91. Ocean Insight. Spectrometers. Availabe online: https://www.oceaninsight.com/products/spectrometers/ (accessed on July 14 2020).
92. Spectral Evolution. Products. Availabe online: https://spectralevolution.com/products/hardware/ (accessed on March 10th 2020).
93. Muller-Karger, F.E.; Hestir, E.; Ade, C.; Turpie, K.; Roberts, D.A.; Siegel, D.; Miller, R.J.; Humm, D.; Izenberg, N.; Keller, M., et al. Satellite sensor requirements for monitoring essential biodiversity variables of coastal ecosystems. **2018**, *28*, 749-760, doi:10.1002/eap.1682.
94. Mouroulis, P.; Van Gorp, B.; Green, R.O.; Dierssen, H.; Wilson, D.W.; Eastwood, M.; Boardman, J.; Gao, B.-C.; Cohen, D.; Franklin, B., et al. Portable Remote Imaging Spectrometer coastal ocean sensor: design, characteristics, and first flight results. *Applied Optics* **2014**, *53*, 1363-1380, doi:10.1364/AO.53.001363.
95. Qian, S.; Bergeron, M.; Djazovski, O.; Maszkiewicz, M.; Girard, R.; Kappus, M.; Bowles, J.; Mannino, A.; Matuszeski, A.; Furlong, M., et al. A spaceborne coastal and inland water color hyperspectral imager. In Proceedings of 2017 IEEE International Geoscience and Remote Sensing Symposium (IGARSS), 23-28 July 2017; pp. 447-450.
96. Achal, S.; SQian, S.-E.; Bergeron, M.; Liu, P.; Umana Diaz, A.; Leung, R. WaterSat Imaging Spectrometer Experiment (WISE) for Canadian Microsatellite Mission. In Proceedings of Ocean Optics, Dubrovnik, Croatia, October 8 2018.
97. Del Castillo, C.; Platnick, S. *Pre-Aerosol, Clouds and ocean Ecosystem (PACE) Mission Science Definition Team Report.*; NASA: 2012.
98. Fu, L.-L. SWOT: Tracking Water on Earth from Mountains to the Deep Sea. Availabe online: https://swot.jpl.nasa.gov/system/documents/files/2229_2229_swot_introduction_fu.pdf?undefined (accessed on July 14 2020).
99. Mission: AirSWOT. Availabe online: https://swot.jpl.nasa.gov/mission/airswot/ (accessed on December 10 2020).

100. Grewal, M.S.; Weill, L.R.; Andrews, A.P. Fundamentals of Satellite and Inertial Navigation. In *Global Positioning Systems, Inertial Navigation, and Integration*, 2006; 10.1002/9780470099728.ch2pp. 18-52.
101. Daakir, M.; Pierrot-Deseilligny, M.; Bosser, P.; Pichard, F.; Thom, C.; Rabot, Y.; Martin, O. Lightweight UAV with on-board photogrammetry and single-frequency GPS positioning for metrology applications. *ISPRS Journal of Photogrammetry and Remote Sensing* **2017**, *127*, 115-126, doi:https://doi.org/10.1016/j.isprsjprs.2016.12.007.
102. Zhang, H.; Aldana-Jaquw, E.; Clapuyt, F.; Wilken, F.; Vanacker, V.; Van Oost, K. Evaluating the potential of post-processing kinematic (PPK) georeferencing for UAV-based structure- from-motion (SfM) photogrammetry and surface change detection. *Earth Surf. Dyn.* **2019**, *7*, 807-827.
103. Kalacska, M.; Lucanus, O.; Arroyo-Mora, J.P.; Laliberté, É.; Elmer, K.; Leblanc, G.; Groves, A. Accuracy of 3D Landscape Reconstruction without Ground Control Points Using Different UAS Platforms. *Drones* **2020**, *4*, doi:10.3390/drones4020013.
104. Koenig, F.; Wong, D. *Real-time kinematics Global Positioning System (GPS) operation and setup method for the Synchronous Impulse Reconstruction (SIRE) radar.*; U.S. Army Research Laboratory: Adelphi, MD, 2010; p 22.
105. Joyce, K.E.; Duce, S.; Leahy, S.M.; Leon, J.; Maier, S.W. Principles and practice of acquiring drone-based image data in marine environments. *Marine and Freshwater Research* **2019**, *70*, 952-963.
106. Bostater, C.R.; Bassetti, L. Detecting submerged features in water: Modeling, sensors and measurements. In Proceedings of Remote Sensing of the Ocean and Sea Ice, Maspalomas, Canary Islands, Spain, 13-16 september 2004; pp. 87-97.
107. Chadwick, B. Remotely Operated Vehicles (ROVs) and Autonomous Underwater Vehicles (AUVs). Availabe online: https://oceanexplorer.noaa.gov/explorations/02fire/background/rovs_auvs/rov_auv.html (accessed on July 14 2020).
108. Antelme, M.; Boon, J.; Mills, O. Search for Endurance Ends. Availabe online: https://weddellseaexpedition.org/news/search-for-endurance-ends/ (accessed on December 13 2020).
109. Lippsett, L. R.I.P. A.B.E.: the pioneering Autonomous Benthic Explorer is lost at sea. *Oceanus* **2010**, *48*, 42+.
110. Odetti, A.; Bibuli, M.; Bruzzone, G.; Caccia, M.; Spirandelli, E.; Bruzzone, G. e-URoPe: a reconfigurable AUV/ROV for man-robot underwater cooperation. *Ifac Papersonline* **2017**, *50*, 11203-11208, doi:10.1016/j.ifacol.2017.08.2089.
111. Roelfsema, C.; Lyons, M.; Dunbabin, M.; Kovacs, E.M.; Phinn, S. Integrating field survey data with satellite image data to improve shallow water seagrass maps: The role of AUV and snorkeller surveys? *Remote Sensing Letters* **2015**, *6*, 135-144, doi:10.1080/2150704X.2015.1013643.
112. Thaler, A.D.; Freitag, A.; Bergman, E.; Fretz, D.; Saleu, W. Robots as vectors for marine invasions: best practices for minimizing transmission of invasive species via observation-class ROVs. *Tropical Conservation Science* **2015**, *8*, 711-717, doi:I - 10.1177/194008291500800308.
113. Elmer, K.; Soffer, R.J.; Arroyo-Mora, J.P.; Kalacska, M. ASDToolkit: A Novel MATLAB Processing Toolbox for ASD Field Spectroscopy Data. *Data* **2020**, *5*, 96, doi:10.3390/data5040096.

114. Watts, A.C.; Ambrosia, V.G.; Hinkley, E.A. Unmanned aircraft systems in remote sensing and scientific research: Classification and considerations of use. *Remote Sensing* **2012**, *4*.
115. Hruska, R.; Mitchell, J.; Anderson, M.; Glenn, N.F. Radiometric and Geometric Analysis of Hyperspectral Imagery Acquired from an Unmanned Aerial Vehicle. *Remote Sensing* **2012**, *4*, 2736-2752.
116. Arroyo-Mora, J.P.; Kalacska, M.; Inamdar, D.; Soffer, R.; Lucanus, O.; Gorman, J.; Naprstek, T.; Schaaf, E.S.; Ifimov, G.; Elmer, K., et al. Implementation of a UAV–Hyperspectral Pushbroom Imager for Ecological Monitoring. *Drones* **2019**, *3*, 12, doi:10.3390/drones3010012.
117. Lucieer, A.; Malenovský, Z.; Veness, T.; Wallace, L. HyperUAS—Imaging Spectroscopy from a Multirotor Unmanned Aircraft System. *Journal of Field Robotics* **2014**, *31*, 571-590, doi:https://doi.org/10.1002/rob.21508.
118. Turner, D.; Lucieer, A.; McCabe, M.; Parkes, S.; Clarke, I. PUSHBROOM HYPERSPECTRAL IMAGING FROM AN UNMANNED AIRCRAFT SYSTEM (UAS) – GEOMETRIC PROCESSINGWORKFLOW AND ACCURACY ASSESSMENT. *Int. Arch. Photogramm. Remote Sens. Spatial Inf. Sci.* **2017**, *XLII-2/W6*, 379-384, doi:10.5194/isprs-archives-XLII-2-W6-379-2017.
119. Arroyo-Mora, J.P.; Kalacska, M.; Soffer, R.; Ifimov, G.; Leblanc, G.; Schaaf, E.S.; Lucanus, O. Evaluation of phenospectral dynamics with Sentinel-2A using a bottom-up approach in a northern ombrotrophic peatland. *Remote Sensing of Environment* **2018**, *216*, 544-560, doi:https://doi.org/10.1016/j.rse.2018.07.021.
120. Soffer, R.; Ifimov, G.; Arroyo-Mora, J.P.; Kalacska, M. Validation of Airborne Hyperspectral Imagery from Laboratory Panel Characterization to Image Quality Assessment: Implications for an Arctic Peatland Surrogate Simulation Site. *Canadian Journal of Remote Sensing* **2019**, *45*, 476-508, doi:10.1080/07038992.2019.1650334.
121. Inamdar, D.; Kalacska, M.; LeBlanc, G.; Arroyo-Mora, J.P. Characterizing and Mitigating Sensor Generated Spatial Correlations in Airborne Hyperspectral Imaging Data. *Remote Sensing* **2020**, *12*, 641, doi:10.3390/rs12040641.
122. Klemas, V. Airborne Remote Sensing of Coastal Features and Processes: An Overview. *Journal of Coastal Research* **2013**, *29*, 239-255, doi:10.2112/jcoastres-d-12-00107.1.
123. Lehmann, A.; Lachavanne, J.B. Geographic information systems and remote sensing in aquatic botany. *Aquatic Botany* **1997**, *58*, 195-207, doi:10.1016/s0304-3770(97)00035-1.
124. Heblinski, J.; Schmieder, K.; Heege, T.; Agyemang, T.K.; Sayadyan, H.; Vardanyan, L. High-resolution satellite remote sensing of littoral vegetation of Lake Sevan (Armenia) as a basis for monitoring and assessment. *Hydrobiologia* **2011**, *661*, 97-111, doi:10.1007/s10750-010-0466-6.
125. Planet. 50 cm SKYSAT IMAGERY NOW AVAILABLE. Availabe online: https://www.planet.com/50cm/ (accessed on July 11 2020).
126. Maxar. WorldView-3 Data Sheet. Availabe online: https://cdn1-originals.webdamdb.com/13264_95553821_1?Policy=eyJTdGF0ZW1lbnQiOlt7IlJlc291cmNlIjoiaHR0cCo6Ly9jZG4xLW9yaWdpbmFscy53ZWJkYW1kYi5jb20vMTMyNjRfOTU1NTM4MjFfMSIsIkNvbmRpdGlvbiI6eyJEYXRlTGVzc1RoYW4iOnsiQVdTOkVwb2NoVGltZSI6MjE0NzQxNDQwMH19fV19&Signature=Xm0vWKqNhBtd5DzE96VX0raV1-kMKBV-MTpLT2qybqqzGqSLqeJ~su~f1TSEy1nd7FSihnWyvhn62jJbKyn9S3IUNFmovbGghp3

ZlYHrGn~uAM~2fO0D0KsIHhmC6WFdcCluTgacDnECsmbF3FV9PSGfBM7iauiW1IW8kMIZhzoC5yYDvujIEWIq~kaBd~TgWS3iMn9YUbtEQhBv7aX55LGmCU~onrHTmIkMUUCy-PP6K~TExG81qX4CVFh1Ia4uWwM5s-zJq9We7nF4crugRUmTRl50FQp~N9j3lLKJic~EEZBwpQN7LtKs8pWOG0BWDHES7FuejH94FCPO1r7uQw__&Key-Pair-Id=APKAI2ASI2IOLRFF2RHA (accessed on February 7th 2020).
127. European Space Agency. The Earth Observation Handbook: Key tables. European Space Agency: Frascati, Italy, 2010.
128. Ripley, H.T.; Dobberfuhl, D.; Hart, C.; Ieee. Mapping Submerged Aquatic Vegetation with Hyperspectral Techniques. In *Oceans 2009, Vols 1-3*, 2009; pp. 1999-+.
129. Lekki, J.; Anderson, R.; Avouris, D.; Becker, R.; Churnside, J.; Cline, M.; Demers, J.; Leshkevich, G.; Liou, L.; Luvall, J., et al. *Airborne Hyperspectral Sensing of Harmful Algal Blooms in the Great Lakes Region: System Calibration and Validation.*; 2017.
130. Wendel, A.; Underwood, J. Illumination compensation in ground based hyperspectral imaging. *ISPRS Journal of Photogrammetry and Remote Sensing* **2017**, *129*, 162-178, doi:https://doi.org/10.1016/j.isprsjprs.2017.04.010.
131. Schläpfer, D.; Richter, R. Geo-atmospheric processing of airborne imaging spectrometry data. Part 1: Parametric orthorectification. *International Journal of Remote Sensing* **2002**, *23*, 2609-2630, doi:10.1080/01431160110115825.
132. Seidel, F.; Schlapfer, D.; Nieke, J.; Itten, K. Sensor Performance Requirements for the Retrieval of Atmospheric Aerosols by Airborne Optical Remote Sensing. *Sensors (Basel)* **2008**, *8*, 1901-1914, doi:10.3390/s8031901.
133. Vincent, J.; Verrelst, J.; Sabater, N.; Alonso, L.; Rivera-Caicedo, J.P.; Martino, L.; Munoz-Mari, J.; Moreno, J. Comparative analysis of atmospheric radiative transfer models using the Atmospheric Look-up table Generator (ALG) toolbox (version2.0). *Geoscientific Model Development Discussions* **2019**, https://doi.org/10.5194/gmd-2019-188, doi:https://doi.org/10.5194/gmd-2019-188.
134. Smith, G.M.; Milton, E.J. The use of the empirical line method to calibrate remotely sensed data to reflectance. *International Journal of Remote Sensing* **1999**, *20*, 2653-2662, doi:10.1080/014311699211994.
135. Manolakis, D.; Lockwood, R.; Cooley, T. *Hyperspectral Imaging Remote Sensing: Physics, Sensors, and Algorithms.*; Cambridge University Press.: Cambridge, UK, 2016.
136. Brook, A.; Dor, E.B. Supervised vicarious calibration (SVC) of hyperspectral remote-sensing data. *Remote Sensing of Environment* **2011**, *115*, 1543-1555, doi:https://doi.org/10.1016/j.rse.2011.02.013.
137. Berk, A.; Bernstein, L.S.; Robertson, D.C. *MODTRAN: A Moderate Resolution Model for LOWTRAN 7.*; Geophysical Directorate Phillips Laboratory: Hanscom AFB, Massachusetts, 04/30/1989, 1989; p 44.
138. Mayer, B.; Kylling, A. Technical note: The libRadtran software package for radiative transfer calculations - description and examples of use. *Atmos. Chem. Phys.* **2005**, *5*, 1855-1877, doi:10.5194/acp-5-1855-2005.
139. Vermote, E.F.; Tanre, D.; Deuze, J.L.; Herman, M.; Morcette, J. Second Simulation of the Satellite Signal in the Solar Spectrum, 6S: An Overview. *IEEE Transactions on Geoscience and Remote Sensing* **1997**, *35*, 675-686, doi:10.1109/36.581987.
140. Lillesand, T.M.; Kiefer, R.W.; Chipman, J.W. *Remote sensing and image interpretation.*, 6th ed. ed.; John Wiley & Sons: Hoboken, NJ, 2008.

141. Lyzenga, D.R. Passive remote sensing techniques for mapping water depth and bottom features. *Applied Optics* **1978**, *17*, 379-383, doi:10.1364/AO.17.000379.
142. Gagnon, P.; Scheibling, R.E.; Jones, W.; Tully, D. The role of digital bathymetry in mapping shallow marine vegetation from hyperspectral image data. *International Journal of Remote Sensing* **2008**, *29*, 879-904, doi:10.1080/01431160701311283.
143. Purkis, S.J.; Pasterkamp, R. Integrating in situ reef-top reflectance spectra with Landsat TM imagery to aid shallow-tropical benthic habitat mapping. *Coral Reefs* **2004**, *23*, 5-20, doi:10.1007/s00338-003-0351-0.
144. Lyzenga, D.R. Remote sensing of bottom reflectance and water attenuation parameters in shallow water using aircraft and Landsat data. *International Journal of Remote Sensing* **1981**, *2*, 71-82, doi:10.1080/01431168108948342.
145. Sagawa, T.; Boisnier, E.; Komatsu, T.; Mustapha, K.B.; Hattour, A.; Kosaka, N.; Miyazaki, S. Using bottom surface reflectance to map coastal marine areas: a new application method for Lyzenga's model. *International Journal of Remote Sensing* **2010**, *31*, 3051-3064, doi:10.1080/01431160903154341.
146. Tassan, S. Modified Lyzenga's method for macroalgae detection in water with non-uniform composition. *International Journal of Remote Sensing* **1996**, *17*, 1601-1607, doi:10.1080/01431169608948725.
147. Bierwirth, P.N.; Lee, T.J.; Burne, R.V. Shallow Sea-Floor Reflectance and Water Depth Derived by Unmixing Multispectral Imagery. *Photogrammetric Engineering & Remote Sensing* **1993**, *59*, 7.
148. Cho, H.J.; Lu, D.J. A water-depth correction algorithm for submerged vegetation spectra. *Remote Sensing Letters* **2010**, *1*, 29-35, doi:10.1080/01431160903246709.
149. Akkaynak, D.; Treibitz, T. Sea-Thru: A Method for Removing Water From Underwater Images. In Proceedings of 2019 IEEE/CVF Conference on Computer Vision and Pattern Recognition (CVPR), 15-20 June 2019; pp. 1682-1691.
150. Manessa, M.D.M.; Haidar, M.; Budhiman, S.; Winarso, G.; Kanno, A.; Sagawa, T.; Sekine, M. Evaluating the performance of Lyzenga's water column correction in case-1 coral reef water using a simulated Wolrdview-2 imagery. In Proceedings of IOP Conf. Ser.:Earth Environ. Sci, October 17-19 2016.
151. Gao, J. Bathymetric mapping by means of remote sensing: methods, accuracy and limitations. *Progress in Physical Geography: Earth and Environment* **2009**, *33*, 103-116, doi:10.1177/0309133309105657.
152. Kay, S.; Hedley, J.D.; Lavender, S. Sun Glint Correction of High and Low Spatial Resolution Images of Aquatic Scenes: a Review of Methods for Visible and Near-Infrared Wavelengths. *Remote Sensing* **2009**, *1*, 697-730, doi:https://doi.org/10.3390/rs1040697.
153. Dobson, J.E.; Bright, E.A.; Ferguson, R.L.; Field, D.W.; Wood, L.L.; Haddad, K.D.; Iredale III, H.; J.R., J.; Klemas, V.; Orth, R.J., et al. *NOAA COASTAL CHANGE ANALYSIS PROGRAM (C-CAP): GUIDANCE FOR REGIONAL IMPLEMENTATION. NOAA Technical Report NMFS 123*; NMFS 123; 2003; p 140.
154. Hedley, J.D.; Harborne, A.R.; Mumby, P.J. Technical note: Simple and robust removal of sun glint for mapping shallow-water benthos. *International Journal of Remote Sensing* **2005**, *26*, 2107-2112, doi:10.1080/01431160500034086.
155. Kutser, T.; Vahtmäe, E.; Paavel, B. Removing air/water interface effects from hyperspectral radiometry data. In Proceedings of Program Book - OCEANS 2012

MTS/IEEE Yeosu: The Living Ocean and Coast - Diversity of Resources and Sustainable Activities.
156. Kutser, T.; Vahtmäe, E.; Praks, J. A sun glint correction method for hyperspectral imagery containing areas with non-negligible water leaving NIR signal. *Remote Sensing of Environment* **2009**, *113*, 2267-2274, doi:10.1016/j.rse.2009.06.016.
157. Andersson, B. Identification and inventory of aquatic plant communities using remote sensing. *Folia Geobotanica et Phytotaxonomica* **1990**, *25*, 227-233, doi:10.1007/BF02913015.
158. Valta-Hulkkonen, K.; Kanninen, A.; Pellikka, P. Remote sensing and GIS for detecting changes in the aquatic vegetation of a rehabilitated lake. *International Journal of Remote Sensing* **2004**, *25*, 5745-5758, doi:10.1080/01431160412331291170.
159. Anker, Y.; Hershkovitz, Y.; Ben Dor, E.; Gasith, A. APPLICATION OF AERIAL DIGITAL PHOTOGRAPHY FOR MACROPHYTE COVER AND COMPOSITION SURVEY IN SMALL RURAL STREAMS. *River Research and Applications* **2014**, *30*, 925-937, doi:10.1002/rra.2700.
160. Pe'eri, S.; Morrison, J.R.; Short, F.; Mathieson, A.; Lippmann, T. Eelgrass and Macroalgal Mapping to Develop Nutrient Criteria in New Hampshire's Estuaries using Hyperspectral Imagery. *Journal of Coastal Research* **2016**, 10.2112/si76-018, 209-218, doi:10.2112/si76-018.
161. Valta-Hulkkonen, K.; Pellikka, P.; Peltoniemi, J. Assessment of bidirectional effects over aquatic macrophyte vegetation in CIR aerial photographs. *Photogrammetric Engineering and Remote Sensing* **2004**, *70*, 581-587, doi:10.14358/pers.70.5.581.
162. Landgrebe, D. Hyperspectral image data analysis. *IEEE Signal Processing Magazine* **2002**, *19*, 17-28, doi:10.1109/79.974718.
163. Hughes, G. On the mean accuracy of statistical pattern recognizers. *IEEE Transactions on Information Theory* **1968**, *14*, 55-63, doi:10.1109/TIT.1968.1054102.
164. Niroumand-Jadidi, M.; Pahlevan, N.; Vitti, A. Mapping substrate types and compositions in shallow streams. *Remote Sensing* **2019**, *11*, doi:10.3390/rs11030262.
165. Mathur, A.; Bruce, L.M.; Robles, W.; Madsen, J. Feature extraction via spectro-temporal analysis of hyperspectral data for vegetative target detection. In Proceedings of Proceedings of the Third International Workshop on the Analysis of Multi-Temporal Remote Sensing Images 2005; pp. 64-66.
166. Bolón-Canedo, V.; Sánchez-Maroño, N.; Alonso-Betanzos, A. Foundations of Feature Selection. In *Feature Selection for High-Dimensional Data.*, Springer International Publishing: Cham, Switzerland, 2015; 10.1007/978-3-319-21858-8_2pp. 13-28.
167. van der Heijden, F.; Duin, R.P.W.; de Ridder, D.; Tax, D.M.J. *Classification, Parameter Estimation and State Estimation: An Engineering Approach Using MATLAB.*; Wiley: Chichester, 2004; 10.1002/0470090154pp. 423.
168. Keshava, N.; Mustard, J.F. Spectral Unmixing. *IEEE Signal Processing Magazine* **2002**, *19*.
169. Rouse , J.W.; Haas, R.H.; Schell, J.A.; Deering, D.W. Monitoring vegetation systems in the Great Plains with ERTS. In Proceedings of The Third Earth Resources Technology Satellite-1 Symposium, Greenbelt, MD, December 10-15 1974; pp. 309-317.
170. Peñuelas, J.; Gamon, J.A.; Griffin, K.L.; Field, C.B. Assessing community type, plant biomass, pigment composition, and photosynthetic efficiency of aquatic vegetation from

spectral reflectance. *Remote Sensing of Environment* **1993**, *46*, 110-118, doi:10.1016/0034-4257(93)90088-F.
171. Espel, D.; Courty, S.; Auda, Y.; Sheeren, D.; Elger, A. Submerged macrophyte assessment in rivers: An automatic mapping method using Pléiades imagery. *Water Research* **2020**, *186*, doi:10.1016/j.watres.2020.116353.
172. Hyun, J.C.; Kirui, P.; Natarajan, H. Test of multi-spectral vegetation index for floating and canopy-forming submerged vegetation. *International Journal of Environmental Research and Public Health* **2008**, *5*, 477-483, doi:10.3390/ijerph5050477.
173. Brooks, C.N.; Grimm, A.G.; Marcarelli, A.M.; Dobson, R.J. Multiscale collection and analysis of submerged aquatic vegetation spectral profiles for Eurasian watermilfoil detection. *Journal of Applied Remote Sensing* **2019**, *13*, doi:10.1117/1.Jrs.13.037501.
174. Villa, P.; Mousivand, A.; Bresciani, M. Aquatic vegetation indices assessment through radiative transfer modeling and linear mixture simulation. *International Journal of Applied Earth Observations and Geoinformation* **2014**, *30*, 113-127, doi:10.1016/j.jag.2014.01.017.
175. Villa, P.; Bresciani, M.; Braga, F.; Bolpagni, R. Comparative assessment of broadband vegetation indices over aquatic vegetation. *IEEE Journal of Selected Topics in Applied Earth Observations and Remote Sensing* **2014**, *7*, 3117-3127, doi:10.1109/JSTARS.2014.2315718.
176. Pande-Chhetri, R.; Abd-Elrahman, A.; Jacoby, C. Classification of submerged aquatic vegetation in black river using hyperspectral image analysis. *Geomatica* **2014**, *68*, 169-182, doi:10.5623/cig2014-302.
177. Zhou, G.H.; Ma, Z.Q.; Sathyendranath, S.; Platt, T.; Jiang, C.; Sun, K. Canopy Reflectance Modeling of Aquatic Vegetation for Algorithm Development: Global Sensitivity Analysis. *Remote Sensing* **2018**, *10*, doi:10.3390/rs10060837.
178. Chen, Q.; Yu, R.; Hao, Y.; Wu, L.; Zhang, W.; Zhang, Q.; Bu, X. A new method for mapping aquatic vegetation especially underwater vegetation in Lake Ulansuhai using GF-1 satellite data. *Remote Sensing* **2018**, *10*, doi:10.3390/rs10081279.
179. Li, F.; Li, C.; Xiao, B.; Wang, Y. Mapping large-scale distribution and changes of aquatic vegetation in Honghu Lake, China, using multitemporal satellite imagery. *Journal of Applied Remote Sensing* **2013**, *7*, doi:10.1117/1.JRS.7.073593.
180. Shaw, G.; Manolakis, D. Signal processing for hyperspectral image exploitation. *IEEE Signal Processing Magazine* **2002**, *19*, doi:10.1109/79.974715.
181. Thamaga, K.H.; Dube, T. Understanding seasonal dynamics of invasive water hyacinth (Eichhornia crassipes) in the Greater Letaba river system using Sentinel-2 satellite data. *GIScience and Remote Sensing* **2019**, 10.1080/15481603.2019.1646988, doi:10.1080/15481603.2019.1646988.
182. Tian, Y.Q.; Yu, Q.; Zimmerman, M.J.; Flint, S.; Waldron, M.C. Differentiating aquatic plant communities in a eutrophic river using hyperspectral and multispectral remote sensing. *Freshwater Biology* **2010**, *55*, 1658-1673, doi:10.1111/j.1365-2427.2010.02400.x.
183. Tilley, D.R.; Ahmed, M.; Son, J.H.; Badrinarayanan, H. Hyperspectral reflectance response of freshwater macrophytes to salinity in a brackish subtropical marsh. *Journal of Environmental Quality* **2007**, *36*, 780-789, doi:10.2134/jeq2005.0327.
184. Kruse, F.A.; Lefkoff, A.B.; Boardman, J.W.; Heidebrecht, K.B.; Shapiro, A.T.; Barloon, P.J.; Goetz, A.F.H. The spectral image processing system (SIPS)—interactive

visualization and analysis of imaging spectrometer data. *Remote Sensing of Environment* **1993**, *44*, 145-163, doi:https://doi.org/10.1016/0034-4257(93)90013-N.
185. Husson, E.; Ecke, F.; Reese, H. Comparison of manual mapping and automated object-based image analysis of non-submerged aquatic vegetation from very-high-resolution UAS images. *Remote Sensing* **2016**, *8*, doi:10.3390/rs8090724.
186. Chabot, D.; Dillon, C.; Shemrock, A.; Weissflog, N.; Sager, E.P.S. An object-based image analysis workflow for monitoring shallow-water aquatic vegetation in multispectral drone imagery. *ISPRS International Journal of Geo-Information* **2018**, *7*, doi:10.3390/ijgi7080294.
187. Manolakis, D.; Shaw, G. Detection Algorithms for Hyperspectral Imaging Applications. *IEEE Signal Processing Magazine* **2002**, *19*, 29-43, doi:10.1109/79.974724.
188. Zhu, C.M.; Zhang, X. Coastal Remote Sensing. In *Modeling with Digital Ocean and Digital Coast*, Zhang, X., Wang, L., Jiang, X., Zhu, C., Eds. 2017; Vol. 18, pp. 169-203.
189. Zhao, D.; Lv, M.; Jiang, H.; Cai, Y.; Xu, D.; An, S. Spatio-Temporal Variability of Aquatic Vegetation in Taihu Lake over the Past 30 Years. *PLoS ONE* **2013**, *8*, doi:10.1371/journal.pone.0066365.
190. Wang, S.; Gao, Y.; Li, Q.; Gao, J.; Zhai, S.; Zhou, Y.; Cheng, Y. Long-term and inter-monthly dynamics of aquatic vegetation and its relation with environmental factors in Taihu Lake, China. *Science of the Total Environment* **2019**, *651*, 367-380, doi:10.1016/j.scitotenv.2018.09.216.
191. Santos, M.J.; Khanna, S.; Hestir, E.L.; Greenberg, J.A.; Ustin, S.L. Measuring landscape-scale spread and persistence of an invaded submerged plant community from airborne Remote sensing. *Ecological Applications* **2016**, *26*, 1733-1744, doi:10.1890/15-0615.
192. Santos, M.J.; Khanna, S.; Hestir, E.L.; Andrew, M.E.; Rajapakse, S.S.; Greenberg, J.A.; Anderson, L.W.J.; Ustin, S.L. Use of hyperspectral remote sensing to evaluate efficacy of aquatic plant management. *Invasive Plant Science and Management* **2009**, *2*, 216-229, doi:10.1614/IPSM-08-115.1.
193. Kalacska, M.; Lucanus, O.; Sousa, L.; Vieira, T.; Arroyo-Mora, J.P. Freshwater Fish Habitat Complexity Mapping Using Above and Underwater Structure-From-Motion Photogrammetry. **2018**, *10*, 1912, doi:10.3390/rs10121912.
194. Carrivick, J.L.; Smith, M.W.; Quincey, D.J. Background to Structure from Motion. In *Structure from Motion in the Geosciences*, 2016; https://doi.org/10.1002/9781118895818.ch3pp. 37-59.
195. Slocum, R.K.; Wright, W.; Parrish, C.; Costa, B.; Sharr, M.; Battista, T.A. *Guidelines for Bathymetric Mapping and Orthoimage Generation using sUAS and SfM, An Approach for Conducting Nearshore Coastal Mapping. NOAA Technical Memorandum NOS NCCOS 265.*; NOAA NOS National Center for Coastal Ocean Science: Silver Spring, MD, 2019; p 83.
196. Reichert, J.; Backes, A.R.; Schubert, P.; Wilke, T. The power of 3D fractal dimensions for comparative shape and structural complexity analyses of irregularly shaped organisms. *Methods in Ecology and Evolution* **2017**, *8*, 1650-1658, doi:10.1111/2041-210x.12829.
197. Storlazzi, C.D.; Dartnell, P.; Hatcher, G.A.; Gibbs, A.E. End of the chain? Rugosity and fine-scale bathymetry from existing underwater digital imagery using structure-from-motion (SfM) technology. *Coral Reefs* **2016**, *35*, 889-894, doi:DOI 10.1007/s00338-016-1462-8.

198. Jing, R.; Gong, Z.N.; Zhao, W.J.; Pu, R.L.; Deng, L. Above-bottom biomass retrieval of aquatic plants with regression models and SfM data acquired by a UAV platform - A case study in Wild Duck Lake Wetland, Beijing, China. *Isprs Journal of Photogrammetry and Remote Sensing* **2017**, *134*, 122-134, doi:10.1016/j.isprsjprs.2017.11.002.
199. Fonstad, M.A.; Dietrich, J.T.; Courville, B.C.; Jensen, J.L.; Carbonneau, P.E. Topographic structure from motion: a new development in photogrammetric measurement. *Earth Surface Processes and Landforms* **2013**, *38*, 421-430.
200. Bryson, M.; Ferrari, R.; Figueira, W.; Pizarro, O.; Madin, J.; Williams, S.; Byrne, M. Characterization of measurement errors using structure-from-motion and photogrammetry to measure marine habitat structural complexity. *Ecology and Evolution* **2017**, *7*, 5669-5681, doi:10.1002/ece3.3127.
201. Leon, J.X.; Roelfsema, C.M.; Saunders, M.I.; Phinn, S.R. Measuring coral reef terrain roughness using 'Structure-from-Motion' close-range photogrammetry. *Geomorphology* **2015**, *242*, 21-28, doi:https://doi.org/10.1016/j.geomorph.2015.01.030.
202. Everitt, J.H.; Yang, C.; Summy, K.R.; Owens, C.S.; Glomski, L.M.; Smart, R.M. Using in situ hyperspectral reflectance data to distinguish nine aquatic plant species. *Geocarto International* **2011**, *26*, 459-473, doi:10.1080/10106049.2011.591944.
203. Dierssen, H.M.; Chlus, A.; Russell, B. Hyperspectral discrimination of floating mats of seagrass wrack and the macroalgae Sargassum in coastal waters of Greater Florida Bay using airborne remote sensing. *Remote Sensing of Environment* **2015**, *167*, 247-258, doi:10.1016/j.rse.2015.01.027.
204. Giardino, C.; Bresciani, M.; Valentini, E.; Gasperini, L.; Bolpagni, R.; Brando, V.E. Airborne hyperspectral data to assess suspended particulate matter and aquatic vegetation in a shallow and turbid lake. *Remote Sensing of Environment* **2015**, *157*, 48-57, doi:10.1016/j.rse.2014.04.034.
205. Williams, D.J.; Rybicki, N.B.; Lombana, A.V.; O'Brien, T.M.; Gomez, R.B. Preliminary Investigation of Submerged Aquatic Vegetation Mapping using Hyperspectral Remote Sensing. *Environmental Monitoring and Assessment* **2003**, *81*, 383-392, doi:10.1023/A:1021318217654.
206. Kumar, A.; Cooper, C.; Remillard, C.M.; Ghosh, S.; Haney, A.; Braun, F.; Conner, Z.; Page, B.; Boyd, K.; Wilde, S., et al. Spatiotemporal monitoring of hydrilla [Hydrilla verticillata (L. f.) Royle] to aid management actions. *Weed Technology* **2019**, *33*, 518-529, doi:10.1017/wet.2019.13.
207. Nahirnick, N.K.; Hunter, P.; Costa, M.; Schroeder, S.; Sharma, T. Benefits and challenges of UAS imagery for eelgrass (Zostera marina) mapping in small estuaries of the Canadian West Coast. *Journal of Coastal Research* **2019**, *35*, 673-683, doi:10.2112/JCOASTRES-D-18-00079.1.
208. Jakhu, R. International law governing acquisition and dissemination of satellite imagery. *Journal of Space Law* **2003**, *29*, 20.
209. National Research Council Canada. Drone site selection tool. Availabe online: https://nrc.canada.ca/en/drone-tool/ (accessed on February 23 2020).
210. Hueni, A.; Damm, A.; Kneubuehler, M.; Schaepman, M.E.; Schlapfer, D. Field and Airborne Spectroscopy Cross Validation -Some Considerations. *IEEE Journal of Selected Topics in Applied Earth Observations and Remote Sensing* **2017**, *10*, 1117-1135, doi:10.1109/JSTARS.2016.2593984.

211. QA4EO task team. A Quality Assurance Framework for Earth Observation: Principles. European Space Agency: Frascati, Italy, 2010.
212. Wei, Y.; Ramapriyan, H.; Downs, R.R.; Shie, C.-L.; Liu, Z.; Moroni, D.; Habermann, T.; Khalsa, S.J.; Peters, B. *Data Quality Working Group's Comprehensive Recommendations for Data Producers and Distributors: ESDS-RFC-033*; 2019.
213. Rijkeboer, M.; Dekker, A.G.; Gons, H.J. Subsurface irradiance reflectance spectra of inland waters differing in morphometry and hydrology. *Aquatic Ecology* **1997**, *31*, 313-323, doi:10.1023/A:1009916501492.
214. Huff, L.C. Acoustic Remote Sensing as a Tool for Habitat Mapping in Alaska Waters. In *Marine Habitat Mapping Technology for Alaska*, Reynolds, J.R.G., H.G., Ed. University of Fairbanks: Fairbanks, Alaska, 2008; 10.4027/mhmta.2008.03.
215. Bennett, D.L.; Bister, T.J.; Ott, R.A. Using Recreation-Grade Side-Scan Sonar to Produce Classified Maps of Submerged Aquatic Vegetation. *North American Journal of Fisheries Management* **2020**, *40*, 145-153, doi:10.1002/nafm.10386.
216. Mizuno, K.; Asada, A.; Ban, S.; Uehara, Y.; Ishida, T.; Okuda, N. Validation of a high-resolution acoustic imaging sonar method by estimating the biomass of submerged plants in shallow water. *Ecological Informatics* **2018**, *46*, 179-184, doi:10.1016/j.ecoinf.2018.07.002.
217. Abukawa, K.; Yamamuro, M.; Kikvidze, Z.; Asada, A.; Xu, C.; Sugimoto, K. Assessing the biomass and distribution of submerged aquatic vegetation using multibeam echo sounding in Lake Towada, Japan. *Limnology* **2013**, *14*, 39-42, doi:10.1007/s10201-012-0383-7.
218. Nayegandhi, A.; Brock, J.C.; Wright, C.W. Small-footprint, waveform-resolving lidar estimation of submerged and sub-canopy topography in coastal environments. *International Journal of Remote Sensing* **2009**, *30*, 861-878, doi:10.1080/01431160802395227.
219. Zharikov, V.V.; Bazarov, K.Y.; Egidarev, E.G.; Lebedev, A.M. Application of Landsat Data for Mapping Higher Aquatic Vegetation of the Far East Marine Reserve. *Oceanology* **2018**, *58*, 487-496, doi:10.1134/s0001437018030207.
220. Bakirman, T.; Gumusay, M.U.; Tuney, I. Mapping of the Seagrass cover along the Mediterranean coast of Turkey using Landsat 8 OLI images. In Proceedings of International Archives of the Photogrammetry, Remote Sensing and Spatial Information Sciences - ISPRS Archives, Prague, Czech Republic; pp. 1103-1105.
221. Hunter, P.D.; Gilvear, D.J.; Tyler, A.N.; Willby, N.J.; Kelly, A. Mapping macrophytic vegetation in shallow lakes using the Compact Airborne Spectrographic Imager (CASI). *Aquatic Conservation: Marine and Freshwater Ecosystems* **2010**, *20*, 717-727, doi:10.1002/aqc.1144.
222. Pu, R.; Bell, S.; Meyer, C.; Baggett, L.; Zhao, Y. Mapping and assessing seagrass along the western coast of Florida using Landsat TM and EO-1 ALI/Hyperion imagery. *Estuarine, Coastal and Shelf Science* **2012**, *115*, 234-245, doi:10.1016/j.ecss.2012.09.006.
223. Su, H.; Karna, D.; Fraim, E.; Fitzgerald, M.; Dominguez, R.; Myers, J.S.; Coffland, B.; Handley, L.R.; Mace, T. Evaluation of eelgrass beds mapping using a high-resolution airborne multispectral scanner. *Photogrammetric Engineering and Remote Sensing* **2006**, *72*, 789-797, doi:10.14358/PERS.72.7.789.

224. Johnsen, G.; Volent, Z.; Dierssen, H.; Pettersen, R.; Ardelan, M.V.; Søreide, F.; Fearns, P.; Ludvigsen, M.; Moline, M. Underwater hyperspectral imagery to create biogeochemical maps of seafloor properties. In *Subsea Optics and Imaging*, Watson, J., Zielinski, O., Eds. Woodhead Publishing: Oxford, UK, 2013; https://doi.org/10.1533/9780857093523.3.508pp. 508-540e.
225. Agjee, N.; Mutanga, O.; Ismail, R. Remote sensing bio-control damage on aquatic invasive alien plant species. *South African Journal of Geomatics* **2015**, *4*, 464-485, doi:10.4314/sajg.v4i4.8.
226. Albright, T.P.; Ode, D.J. Monitoring the dynamics of an invasive emergent macrophyte community using operational remote sensing data. *Hydrobiologia* **2011**, *661*, 469-474, doi:10.1007/s10750-010-0537-8.
227. Armstrong, R.A. Remote sensing of submerged vegetation canopies for biomass estimation. *International Journal of Remote Sensing* **1993**, *14*, 621-627, doi:10.1080/01431169308904363.
228. Bolpagni, R.; Bresciani, M.; Laini, A.; Pinardi, M.; Matta, E.; Ampe, E.M.; Giardino, C.; Viaroli, P.; Bartoli, M. Remote sensing of phytoplankton-macrophyte coexistence in shallow hypereutrophic fluvial lakes. *Hydrobiologia* **2014**, *737*, 67-76, doi:10.1007/s10750-013-1800-6.
229. Boschi, L.S.; Galo, M.; Rotta, L.H.S.; Watanabe, F.S.Y. Mapping the Bio-volume of Submerged Aquatic Vegetation through Hydro-acoustic Data and High-Resolution Multi-Spectral Imaging. *Planta Daninha* **2012**, *30*, 525-539, doi:10.1590/s0100-83582012000300008.
230. Brinkhoff, J.; Hornbuckle, J.; Barton, J.L. Assessment of Aquatic Weed in Irrigation Channels Using UAV and Satellite Imagery. *Water* **2018**, *10*, doi:10.3390/w10111497.
231. Cai, F.; Lu, W.; Shi, W.; He, S. A mobile device-based imaging spectrometer for environmental monitoring by attaching a lightweight small module to a commercial digital camera. *Scientific Reports* **2017**, *7*, doi:10.1038/s41598-017-15848-x.
232. Chami, M.; Lenot, X.; Guillaume, M.; Lafrance, B.; Briottet, X.; Minghelli, A.; Jay, S.; Deville, Y.; Serfaty, V. Analysis and quantification of seabed adjacency effects in the subsurface upward radiance in shallow waters. *Optics Express* **2019**, *27*, A319-A338, doi:10.1364/OE.27.00A319.
233. Chami, M.; Harmel, T. Remote Sensing and Ocean Color. In *Land Surface Remote Sensing in Urban and Coastal Areas*, 2016; 10.1016/B978-1-78548-160-4.50004-2pp. 141-183.
234. Chander, S.; Pompapathi, V.; Gujrati, A.; Singh, R.P.; Chaplot, N.; Patel, U.D. Growth of invasive aquatic macrophytes over Tapi river. In Proceedings of International Archives of the Photogrammetry, Remote Sensing and Spatial Information Sciences - ISPRS Archives; pp. 829-833.
235. Cheruiyot, E.K.; Mito, C.; Menenti, M.; Gorte, B.; Koenders, R.; Akdim, N. Evaluating MERIS-based aquatic vegetation mapping in lake victoria. *Remote Sensing* **2014**, *6*, 7762-7782, doi:10.3390/rs6087762.
236. Costa, B.M.; Battista, T.A.; Pittman, S.J. Comparative evaluation of airborne LiDAR and ship-based multibeam SoNAR bathymetry and intensity for mapping coral reef ecosystems. *Remote Sensing of Environment* **2009**, *113*, 1082-1100, doi:https://doi.org/10.1016/j.rse.2009.01.015.

237. Dekker, A.G.; Brando, V.E.; Anstee, J.M. Retrospective seagrass change detection in a shallow coastal tidal Australian lake. *Remote Sensing of Environment* **2005**, *97*, 415-433, doi:10.1016/j.rse.2005.02.017.
238. Dekker, A.G.; Phinn, S.R.; Anstee, J.; Bissett, P.; Brando, V.E.; Casey, B.; Fearns, P.; Hedley, J.; Klonowski, W.; Lee, Z.P., et al. Intercomparison of shallow water bathymetry, hydro-optics, and benthos mapping techniques in Australian and Caribbean coastal environments. **2011**, *9*, 396-425, doi:10.4319/lom.2011.9.396.
239. Dogan, O.K.; Akyurek, Z.; Beklioglu, M. Identification and mapping of submerged plants in a shallow lake using quickbird satellite data. *Journal of Environmental Management* **2009**, *90*, 2138-2143, doi:10.1016/j.jenvman.2007.06.022.
240. Fearns, P.R.C.; Klonowski, W.; Babcock, R.C.; England, P.; Phillips, J. Shallow water substrate mapping using hyperspectral remote sensing. *Continental Shelf Research* **2011**, *31*, 1249-1259, doi:https://doi.org/10.1016/j.csr.2011.04.005.
241. Ferguson, R.L.; Wood, L.L. Mapping Submerged Aquatic Vegetation in North Carolina with Conventional Aerial Photography. *Fish and Wildlife Service Biological Report* **1990**, *90*, 125-133.
242. Ferguson, R.L.; Korfmacher, K. Remote sensing and GIS analysis of seagrass meadows in North Carolina, USA. *Aquatic Botany* **1997**, *58*, 241-258, doi:https://doi.org/10.1016/S0304-3770(97)00038-7.
243. Ferretti, R.; Bibuli, M.; Caccia, M.; Chiarella, D.; Odetti, A.; Ranieri, A.; Zereik, E.; Bruzzone, G. Towards Posidonia Meadows Detection, Mapping and Automatic recognition using Unmanned Marine Vehicles. *IFAC-PapersOnLine* **2017**, *50*, 12386-12391, doi:10.1016/j.ifacol.2017.08.2504.
244. Fritz, C.; Schneider, T.; Geist, J. Seasonal variation in spectral response of submerged aquatic macrophytes: A case study at Lake Starnberg (Germany). *Water (Switzerland)* **2017**, *9*, doi:10.3390/w9070527.
245. Fritz, C.; Dörnhöfer, K.; Schneider, T.; Geist, J.; Oppelt, N. Mapping submerged aquatic vegetation using RapidEye satellite data: The example of Lake Kummerow (Germany). *Water (Switzerland)* **2017**, *9*, doi:10.3390/w9070510.
246. Fritz, C.; Kuhwald, K.; Schneider, T.; Geist, J.; Oppelt, N. Sentinel-2 for mapping the spatio-temporal development of submerged aquatic vegetation at Lake Starnberg (Germany). *Journal of Limnology* **2019**, *78*, 71-91, doi:10.4081/jlimnol.2019.1824.
247. Gao, Y.; Gao, J.; Wang, J.; Wang, S.; Li, Q.; Zhai, S.; Zhou, Y. Estimating the biomass of unevenly distributed aquatic vegetation in a lake using the normalized water-adjusted vegetation index and scale transformation method. *Science of the Total Environment* **2017**, *601-602*, 998-1007, doi:10.1016/j.scitotenv.2017.05.163.
248. Garcia, R.A.; Lee, Z.; Barnes, B.B.; Hu, C.; Dierssen, H.M.; Hochberg, E.J. Benthic classification and IOP retrievals in shallow water environments using MERIS imagery. *Remote Sensing of Environment* **2020**, *249*, doi:10.1016/j.rse.2020.112015.
249. Ghirardi, N.; Bolpagni, R.; Bresciani, M.; Valerio, G.; Pilotti, M.; Giardino, C. Spatiotemporal Dynamics of Submerged Aquatic Vegetation in a Deep Lake from Sentinel-2 Data. *Water* **2019**, *11*, doi:10.3390/w11030563.
250. Gower, J.; Hu, C.M.; Borstad, G.; King, S. Ocean color satellites show extensive lines of floating sargassum in the Gulf of Mexico. *Ieee Transactions on Geoscience and Remote Sensing* **2006**, *44*, 3619-3625, doi:10.1109/tgrs.2006.882258.

251. Gullström, M.; Lundén, B.; Bodin, M.; Kangwe, J.; Öhman, M.C.; Mtolera, M.S.P.; Björk, M. Assessment of changes in the seagrass-dominated submerged vegetation of tropical Chwaka Bay (Zanzibar) using satellite remote sensing. *Estuarine, Coastal and Shelf Science* **2006**, *67*, 399-408, doi:10.1016/j.ecss.2005.11.020.
252. Han, L. Spectral reflectance of Thalassid testudinum with varying depths. In Proceedings of Igarss 2002: Ieee International Geoscience and Remote Sensing Symposium and 24th Canadian Symposium on Remote Sensing, Vols I-Vi, Proceedings: Remote Sensing: Integrating Our View of the Planet; pp. 2123-2125.
253. Herkül, K.; Kotta, J.; Kutser, T.; Vahtmäe, E. Relating Remotely Sensed Optical Variability to Marine Benthic Biodiversity. *PLoS ONE* **2013**, *8*, doi:10.1371/journal.pone.0055624.
254. Hestir, E.L.; Khanna, S.; Andrew, M.E.; Santos, M.J.; Viers, J.H.; Greenberg, J.A.; Rajapakse, S.S.; Ustin, S.L. Identification of invasive vegetation using hyperspectral remote sensing in the California Delta ecosystem. *Remote Sensing of Environment* **2008**, *112*, 4034-4047, doi:10.1016/j.rse.2008.01.022.
255. Hestir, E.L.; Greenberg, J.A.; Ustin, S.L. Classification trees for aquatic vegetation community prediction from imaging spectroscopy. *IEEE Journal of Selected Topics in Applied Earth Observations and Remote Sensing* **2012**, *5*, 1572-1584, doi:10.1109/JSTARS.2012.2200878.
256. Hoang, T.; Garcia, R.; O'Leary, M.; Fotedar, R. Identification and mapping of marine submerged aquatic vegetation in shallow coastal waters with worldview-2 satellite data. *Journal of Coastal Research* **2016**, *1*, 1287-1291, doi:10.2112/SI75-258.1.
257. Hogrefe, K.R.; Ward, D.H.; Donnelly, T.F.; Dau, N. Establishing a baseline for regional scale monitoring of eelgrass (Zostera marina) habitat on the lower Alaska Peninsula. *Remote Sensing* **2014**, *6*, 12447-12477, doi:10.3390/rs61212447.
258. Howari, F.M.; Jordan, B.R.; Bouhouche, N.; Wyllie-Echeverria, S. Field and Remote-Sensing Assessment of Mangrove Forests and Seagrass Beds in the Northwestern Part of the United Arab Emirates. *Journal of Coastal Research* **2009**, *25*, 48-56, doi:10.2112/07-0867.1.
259. Hu, C.M.; Lee, Z.P.; Muller-Karger, F.E.; Carder, K.L.; Walsh, J.J. Ocean color reveals phase shift between marine plants and yellow substance. *Ieee Geoscience and Remote Sensing Letters* **2006**, *3*, 262-266, doi:10.1109/lgrs.2005.862527.
260. Huen, W.K.; Zhang, Y. Preliminary studies on coral mapping in tung ping chau of the eastern Hong Kong using high-resolution SPOT satellite imagery. *Annals of GIS* **2011**, *17*, 93-98, doi:10.1080/19475683.2011.576457.
261. Husson, E.; Reese, H.; Ecke, F. Combining spectral data and a DSM from UAS-images for improved classification of non-submerged aquatic vegetation. *Remote Sensing* **2017**, *9*, doi:10.3390/rs9030247.
262. Husson, E.; Hagner, O.; Ecke, F. Unmanned aircraft systems help to map aquatic vegetation. *Applied Vegetation Science* **2014**, *17*, 567-577, doi:10.1111/avsc.12072.
263. Irish, J.L.; Lillycrop, W.J. Monitoring New Pass, Florida, with High Density Lidar Bathymetry. *Journal of Coastal Research* **1997**, *13*, 1130-1140.
264. Jakubauskas, M.; Kindscher, K.; Fraser, A.; Debinski, D.; Price, K.P. Close-range remote sensing of aquatic macrophyte vegetation cover. *International Journal of Remote Sensing* **2000**, *21*, 3533-3538, doi:10.1080/014311600750037543.

265. Jenkins, C.; Eggleton, J.; Barry, J.; O'Connor, J. Advances in assessing Sabellaria spinulosa reefs for ongoing monitoring. *Ecology and Evolution* **2018**, *8*, 7673-7687, doi:10.1002/ece3.4292.
266. John, C.M.; Nath, K. Integration of multispectral satellite and hyperspectral field data for aquatic macrophyte studies. In Proceedings of International Archives of the Photogrammetry, Remote Sensing and Spatial Information Sciences - ISPRS Archives, Hyderabad, India; pp. 581-588.
267. Kasvi, E.; Salmela, J.; Lotsari, E.; Kumpula, T.; Lane, S.N. Comparison of remote sensing based approaches for mapping bathymetry of shallow, clear water rivers. *Geomorphology* **2019**, *333*, 180-197, doi:10.1016/j.geomorph.2019.02.017.
268. Khanh Ni, T.N.; Tin, H.C.; Thach, V.T.; Jamet, C.; Saizen, I. Mapping submerged aquatic vegetation along the central Vietnamese coast using multi-source remote sensing. *ISPRS International Journal of Geo-Information* **2020**, *9*, doi:10.3390/ijgi9060395.
269. Khanna, S.; Santos, M.J.; Hestir, E.L.; Ustin, S.L. Plant community dynamics relative to the changing distribution of a highly invasive species, Eichhornia crassipes: a remote sensing perspective. *Biological Invasions* **2012**, *14*, 717-733, doi:10.1007/s10530-011-0112-x.
270. Koedsin, W.; Intararuang, W.; Ritchie, R.J.; Huete, A. An integrated field and remote sensing method for mapping seagrass species, cover, and biomass in Southern Thailand. *Remote Sensing* **2016**, *8*, doi:10.3390/rs8040292.
271. Kotta, J.; Kutser, T.; Teeveer, K.; Vahtmäe, E.; Pärnoja, M. Predicting Species Cover of Marine Macrophyte and Invertebrate Species Combining Hyperspectral Remote Sensing, Machine Learning and Regression Techniques. *PLoS ONE* **2013**, *8*, doi:10.1371/journal.pone.0063946.
272. Lane, C.R.; Anenkhonov, O.; Liu, H.; Autrey, B.C.; Chepinoga, V. Classification and inventory of freshwater wetlands and aquatic habitats in the Selenga River Delta of Lake Baikal, Russia, using high-resolution satellite imagery. *Wetlands Ecology and Management* **2015**, *23*, 195-214, doi:10.1007/s11273-014-9369-z.
273. Lathrop, R.G.; Montesano, P.; Haag, S. A multi-scale segmentation approach to mapping seagrass habitats using airborne digital camera imagery. *Photogrammetric Engineering and Remote Sensing* **2006**, *72*, 665-675, doi:10.14358/PERS.72.6.665.
274. Liang, Q.; Zhang, Y.; Ma, R.; Loiselle, S.; Li, J.; Hu, M. A MODIS-based novel method to distinguish surface cyanobacterial scums and aquatic macrophytes in Lake Taihu. *Remote Sensing* **2017**, *9*, doi:10.3390/rs9020133.
275. Liu, X.; Zhang, Y.; Shi, K.; Zhou, Y.; Tang, X.; Zhu, G.; Qin, B. Mapping aquatic vegetation in a large, shallow eutrophic lake: A frequency-based approach using multiple years of MODIS data. *Remote Sensing* **2015**, *7*, 10295-10320, doi:10.3390/rs70810295.
276. Louchard, E.M.; Reid, R.P.; Stephens, F.C.; Davis, C.O.; Leathers, R.A.; T. Valerie, D. Optical remote sensing of benthic habitats and bathymetry in coastal environments at Lee Stocking Island, Bahamas: A comparative spectral classification approach. *Limnology and Oceanography* **2003**, *48*, 511-521, doi:10.4319/lo.2003.48.1_part_2.0511.
277. Lu, D.J.; Cho, H.J. An improved water-depth correction algorithm for seagrass mapping using hyperspectral data. *Remote Sensing Letters* **2011**, *2*, 91-97, doi:10.1080/01431161.2010.502152.
278. Luo, J.H.; Ma, R.H.; Duan, H.T.; Hu, W.P.; Zhu, J.G.; Huang, W.J.; Lin, C. A New Method for Modifying Thresholds in the Classification of Tree Models for Mapping

Aquatic Vegetation in Taihu Lake with Satellite Images. *Remote Sensing* **2014**, *6*, 7442-7462, doi:10.3390/rs6087442.
279. Luo, J.H.; Li, X.C.; Ma, R.H.; Li, F.; Duan, H.T.; Hu, W.P.; Qin, B.Q.; Huang, W.J. Applying remote sensing techniques to monitoring seasonal and interannual changes of aquatic vegetation in Taihu Lake, China. *Ecological Indicators* **2016**, *60*, 503-513, doi:10.1016/j.ecolind.2015.07.029.
280. Luo, J.; Duan, H.; Ma, R.; Jin, X.; Li, F.; Hu, W.; Shi, K.; Huang, W. Mapping species of submerged aquatic vegetation with multi-seasonal satellite images and considering life history information. *International Journal of Applied Earth Observation and Geoinformation* **2017**, *57*, 154-165, doi:10.1016/j.jag.2016.11.007.
281. Lyons, M.; Phinn, S.; Roelfsema, C. Long Term Land Cover and Seagrass Mapping Using Landsat Sensors from 1972 – 2010 in the Coastal Environment of South East Queensland, Australia *ISPRS J. Photogramm. Remote Sens.* **2012**, *71*, 34-46.
282. Macleod, R.D.; Congalton, R.G. A quantitative comparison of change-detection algorithms for monitoring eelgrass from remotely sensed data. *Photogrammetric engineering and remote sensing* **1998**, *64*, 207-216.
283. Malthus, T.J.; George, D.G. Airborne remote sensing of macrophytes in Cefni Reservoir, Anglesey, UK. *Aquatic Botany* **1997**, *58*, 317-332, doi:10.1016/s0304-3770(97)00043-0.
284. McLaren, K.; McIntyre, K.; Prospere, K. Using the random forest algorithm to integrate hydroacoustic data with satellite images to improve the mapping of shallow nearshore benthic features in a marine protected area in Jamaica. *GIScience and Remote Sensing* **2019**, 10.1080/15481603.2019.1613803, doi:10.1080/15481603.2019.1613803.
285. Mehrubeoglu, M.; Trombley, C.; Shanks, S.E.; Cammarata, K.; Simons, J.; Zimba, P.V.; McLauchlan, L. Empirical mode decomposition of hyperspectral images for segmentation of seagrass coverage. In Proceedings of IST 2014 - 2014 IEEE International Conference on Imaging Systems and Techniques, Proceedings; pp. 33-37.
286. Meyer, C.A.; Pu, R. Seagrass resource assessment using remote sensing methods in St. Joseph Sound and Clearwater Harbor, Florida, USA. *Environmental Monitoring and Assessment* **2012**, *184*, 1131-1143, doi:10.1007/s10661-011-2028-4.
287. Modjeski, A.C. Submerged Aquatic Vegetation (SAV) Aerial Hyperspectral Imaging and Groundtruthing Survey: Use of Aerial Hyperspectral Imaging in Defining Habitat Areas of Particular-Concern for Summer Flounder in a High-Energy Estuarine Environment. In *Environment Concerns in Rights-of-Way Management 8th International Symposium*, 2008; 10.1016/B978-044453223-7.50079-4pp. 723-728.
288. Mumby, P.J.; Edwards, A.J. Mapping marine environments with IKONOS imagery: enhanced spatial resolution can deliver greater thematic accuracy. *Remote Sensing of Environment* **2002**, *82*, 248-257, doi:https://doi.org/10.1016/S0034-4257(02)00041-X.
289. Nelson, T.A.; Gillanders, S.N.; Harper, J.; Morris, M. Nearshore Aquatic Habitat Monitoring: A Seabed Imaging and Mapping Approach. *Journal of Coastal Research* **2011**, *27*, 348-355, doi:10.2112/jcoastres-d-10-00110.1.
290. Nieder, W.C.; Barnaba, E.; Findlay, S.E.G.; Hoskins, S.; Holochuck, N.; Blair, E.A. Distribution and abundance of submerged aquatic vegetation and Trapa natans in the Hudson River estuary. *Journal of Coastal Research* **2004**, *20*, 150-161, doi:10.2112/si45-150.1.

291. Nobi, E.P.; Thangaradjou, T. Evaluation of the spatial changes in seagrass cover in the lagoons of Lakshadweep islands, India, using IRS LISS III satellite images. *Geocarto International* **2012**, *27*, 647-660, doi:10.1080/10106049.2012.665501.
292. Olmanson, L.G.; Page, B.P.; Finlay, J.C.; Brezonik, P.L.; Bauer, M.E.; Griffin, C.G.; Hozalski, R.M. Regional measurements and spatial/temporal analysis of CDOM in 10,000+ optically variable Minnesota lakes using Landsat 8 imagery. *Science of the Total Environment* **2020**, *724*, doi:10.1016/j.scitotenv.2020.138141.
293. Olmanson, L.G.; Brezonik, P.L.; Bauer, M.E. Airborne hyperspectral remote sensing to assess spatial distribution of water quality characteristics in large rivers: The Mississippi River and its tributaries in Minnesota. *Remote Sensing of Environment* **2013**, *130*, 254-265, doi:10.1016/j.rse.2012.11.023.
294. O'Neill, J.D.; Costa, M.P.F.; Sharma, T. Remote sensing of shallow coastal benthic substrates: *In situ* spectra and mapping of eelgrass (*Zostera marina)* in the Gulf Islands National Park Reserve of Canada. *Remote Sensing* **2011**, *3*, 975-1005.
295. Orth, R.J.; Carruthers, T.J.; Dennison, W.C.; Duarte, C.M.; Fourqurean, J.W.; Heck, K.L.; Hughes, A.R.; Kendrick, G.A.; Kenworthy, W.J.; Olyarnik, S. A global crisis for seagrass ecosystems. *Bioscience* **2006**, *56*, 987-996.
296. Oyama, Y.; Matsushita, B.; Fukushima, T. Distinguishing surface cyanobacterial blooms and aquatic macrophytes using Landsat/TM and ETM+ shortwave infrared bands. *Remote Sensing of Environment* **2015**, *157*, 35-47, doi:10.1016/j.rse.2014.04.031.
297. Parson, L.E.; Lillycrop, W.J.; Klein, C.J.; Ives, R.C.P.; Orlando, S.P. Use of Lidar Technology for Collecting Shallow Water Bathymetry of Florida Bay. *Journal of Coastal Research* **1997**, *13*, 1173-1180.
298. Peneva, E.; Griffith, J.; Carter, G. Seagrass Mapping in the Northern Gulf of Mexico using Airborne Hyperspectral Imagery: A Comparison of Classification Methods. *Journal of Coastal Research - J COASTAL RES* **2008**, *24*, doi:10.2112/06-0764.1.
299. Phinn, S.; Roelfsema, C.; Dekker, A.; Brando, V.; Anstee, J. Mapping seagrass species, cover and biomass in shallow waters: An assessment of satellite multi-spectral and airborne hyper-spectral imaging systems in Moreton Bay (Australia). *Remote Sensing of Environment* **2008**, *112*, 3413-3425, doi:https://doi.org/10.1016/j.rse.2007.09.017.
300. Pinardi, M.; Bresciani, M.; Villa, P.; Cazzaniga, I.; Laini, A.; Tóth, V.; Fadel, A.; Austoni, M.; Lami, A.; Giardino, C. Spatial and temporal dynamics of primary producers in shallow lakes as seen from space: Intra-annual observations from Sentinel-2A. *Limnologica* **2018**, *72*, 32-43, doi:10.1016/j.limno.2018.08.002.
301. Pinnel, N.; Heege, T.; Zimmermann, S. Spectral discrimination of submerged macrophytes in lakes using hyperspectral remote sensing data. In Proceedings of Ocean Optics XVII, Freemantle, Australia, 25-29 October 2004; pp. 1-16.
302. Pu, R.L.; Bell, S. A protocol for improving mapping and assessing of seagrass abundance along the West Central Coast of Florida using Landsat TM and EO-1 ALI/Hyperion images. *Isprs Journal of Photogrammetry and Remote Sensing* **2013**, *83*, 116-129, doi:10.1016/j.isprsjprs.2013.06.008.
303. Pu, R.; Bell, S.; Meyer, C. Mapping and assessing seagrass bed changes in Central Florida's west coast using multitemporal Landsat TM imagery. *Estuarine, Coastal and Shelf Science* **2014**, *149*, 68-79, doi:10.1016/j.ecss.2014.07.014.

304. Pu, R.; Bell, S.; Baggett, L.; Meyer, C.; Zhao, Y. Discrimination of seagrass species and cover classes with in situ hyperspectral data. *Journal of Coastal Research* **2012**, *28*, 1330-1344, doi:10.2112/JCOASTRES-D-11-00229.1.
305. Qing, S.; A, R.; Shun, B.; Zhao, W.; Bao, Y.; Hao, Y. Distinguishing and mapping of aquatic vegetations and yellow algae bloom with Landsat satellite data in a complex shallow Lake, China during 1986–2018. *Ecological Indicators* **2020**, *112*, doi:10.1016/j.ecolind.2020.106073.
306. Quintino, V.; Freitas, R.; Mamede, R.; Ricardo, F.; Rodrigues, A.M.; Mota, J.; Pérez-Ruzafa, Á.; Marcos, C. Remote sensing of underwater vegetation using single-beam acoustics. *ICES Journal of Marine Science* **2010**, *67*, 594-605, doi:10.1093/icesjms/fsp251.
307. Rahnemoonfar, M.; Yari, M.; Rahman, A.; Kline, R. The First Automatic Method for Mapping the Pothole in Seagrass. In Proceedings of IEEE Computer Society Conference on Computer Vision and Pattern Recognition Workshops; pp. 267-274.
308. Reshitnyk, L.; Costa, M.; Robinson, C.; Dearden, P. Evaluation of WorldView-2 and acoustic remote sensing for mapping benthic habitats in temperate coastal Pacific waters. *Remote Sensing of Environment* **2014**, *153*, 7-23, doi:10.1016/j.rse.2014.07.016.
309. Roessler, S.; Wolf, P.; Schneider, T.; Melzer, A. Multispectral remote sensing of invasive aquatic plants using RapidEye. In *Lecture Notes in Geoinformation and Cartography*, 2013; 10.1007/978-3-642-32714-8_7pp 109-123.
310. Rotta, L.H.D.S.; Imai, N.N. Submerged macrophytes height estimation by echosounder data sample. In Proceedings of International Geoscience and Remote Sensing Symposium (IGARSS); pp. 808-811.
311. Sabol, B.M.; Melton, R.E.; Chamberlain, R.; Doering, P.; Haunert, K. Evaluation of a digital echo sounder system for detection of submersed aquatic vegetation. *Estuaries* **2002**, *25*, 133-141, doi:10.1007/bf02696057.
312. Saul, S.; Purkis, S. Semi-Automated Object-Based Classification of Coral Reef Habitat using Discrete Choice Models. *Remote Sensing* **2015**, *7*, 15894-15916, doi:10.3390/rs71215810.
313. Schweizer, D.; Armstrong, R.A.; Posada, J. Remote sensing characterization of benthic habitats and submerged vegetation biomass in Los Roques Archipelago National Park, Venezuela. *International Journal of Remote Sensing* **2005**, *26*, 2657-2667, doi:10.1080/01431160500104111.
314. Shapiro, A.C.; Rohmann, S.O. Mapping changes in submerged aquatic vegetation using Landsat imagery and benthic habitat data: Coral reef ecosystem monitoring in Vieques Sound between 1985 and 2000. *Bulletin of Marine Science* **2006**, *79*, 375-388.
315. Shekede, M.D.; Kusangaya, S.; Schmidt, K. Spatio-temporal variations of aquatic weeds abundance and coverage in Lake Chivero, Zimbabwe. *Physics and Chemistry of the Earth* **2008**, *33*, 714-721, doi:10.1016/j.pce.2008.06.052.
316. Shuchman, R.A.; Sayers, M.J.; Brooks, C.N. Mapping and monitoring the extent of submerged aquatic vegetation in the laurentian great lakes with multi-scale satellite remote sensing. *Journal of Great Lakes Research* **2013**, *39*, 78-89, doi:10.1016/j.jglr.2013.05.006.
317. Silva, T.S.F.; Costa, M.P.F.; Melack, J.M. Spatial and temporal variability of macrophyte cover and productivity in the eastern Amazon floodplain: A remote sensing approach. *Remote Sensing of Environment* **2010**, *114*, 1998-2010, doi:10.1016/j.rse.2010.04.007.

318. Soo Lee, B.; McGwire, K.C.; Fritsen, C.H. Identification and quantification of aquatic vegetation with hyperspectral remote sensing in Western Nevada rivers, USA. *International Journal of Remote Sensing* **2011**, *32*, 9093-9117, doi:10.1080/01431161.2010.549850.
319. Sprenkle, E.S.; Smock, L.A.; Anderson, J.E. Distribution and growth of submerged aquatic vegetation in the Piedmont section of the James river, Virginia. *Southeastern Naturalist* **2004**, *3*, 517-530, doi:10.1656/1528-7092(2004)003[0517:Dagosa]2.0.Co;2.
320. Theriault, C.; Scheibling, R.; Hatcher, B.; Jones, W. Mapping the distribution of an invasive marine alga (Codium fragile spp. tomentosoides) in optically shallow coastal waters using the compact airborne spectrographic imager (CASI). *Canadian Journal of Remote Sensing* **2006**, *32*, 315-329, doi:10.5589/m06-027.
321. Thomson, A.G.; Fuller, R.M.; Sparks, T.H.; Yates, M.G.; Eastwood, J.A. Ground and airborne radiometry over intertidal surfaces: Waveband selection for cover classification. *International Journal of Remote Sensing* **1998**, *19*, 1189-1205, doi:10.1080/014311698215685.
322. Thorhaug, A.; Richardson, A.D.; Berlyn, G.P. Spectral reflectance of the seagrasses: Thalassia testudinum, Halodule wrightii, Syringodium filiforme and five marine algae. *International Journal of Remote Sensing* **2007**, *28*, 1487-1501, doi:10.1080/01431160600954662.
323. Torres-Pulliza, D.; Wilson, J.R.; Darmawan, A.; Campbell, S.J.; Andrefouet, S. Ecoregional scale seagrass mapping: A tool to support resilient MPA network design in the Coral Triangle. *Ocean & Coastal Management* **2013**, *80*, 55-64, doi:10.1016/j.ocecoaman.2013.04.005.
324. Traganos, D.; Reinartz, P. Interannual change detection of mediterranean seagrasses using RapidEye image time series. *Frontiers in Plant Science* **2018**, *9*, doi:10.3389/fpls.2018.00096.
325. Uhl, F.; Bartsch, I.; Oppelt, N. Submerged Kelp Detection with Hyperspectral Data. *Remote Sensing* **2016**, *8*, doi:10.3390/rs8060487.
326. Underwood, E.C.; Mulitsch, M.J.; Greenberg, J.A.; Whiting, M.L.; Ustin, S.L.; Kefauver, S.C. Mapping invasive aquatic vegetation in the sacramento-san Joaquin Delta using hyperspectral imagery. *Environmental Monitoring and Assessment* **2006**, *121*, 47-64, doi:10.1007/s10661-005-9106-4.
327. Villa, P.; Pinardi, M.; Bolpagni, R.; Gillier, J.M.; Zinke, P.; Nedelcut, F.; Bresciani, M. Assessing macrophyte seasonal dynamics using dense time series of medium resolution satellite data. *Remote Sensing of Environment* **2018**, *216*, 230-244, doi:10.1016/j.rse.2018.06.048.
328. VonBank, J.A.; Casper, A.F.; Yetter, A.P.; Hagy, H.M. Evaluating a Rapid Aerial Survey for Floating-Leaved Aquatic Vegetation. *Wetlands* **2017**, *37*, 753-762, doi:10.1007/s13157-017-0910-8.
329. Wabnitz, C.C.; Andréfouët, S.; Torres-Pulliza, D.; Müller-Karger, F.E.; Kramer, P.A. Regional-scale seagrass habitat mapping in the Wider Caribbean region using Landsat sensors: Applications to conservation and ecology. *Remote Sensing of Environment* **2008**, *112*, 3455-3467, doi:https://doi.org/10.1016/j.rse.2008.01.020.
330. Wang, Y.; Traber, M.; Milstead, B.; Stevens, S. Terrestrial and submerged aquatic vegetation mapping in fire Island National Seashore using high spatial resolution remote sensing data. *Marine Geodesy* **2007**, *30*, 77-95, doi:10.1080/01490410701296226.

331. Wang, L.; Gong, P.; Dronova, I. Aquatic plant functional type spectral characteristics analysis and comparison using multi-temporal and multi-sensor remote sensing over the Poyang Lake Wetland, China. In Proceedings of 2010 18th International Conference on Geoinformatics, Geoinformatics 2010.
332. Wang, C.-K.; Philpot, W.D. Using airborne bathymetric lidar to detect bottom type variation in shallow waters. *Remote Sensing of Environment* **2007**, *106*, 123-135, doi:https://doi.org/10.1016/j.rse.2006.08.003.
333. Watanabe, F.S.Y.; Imai, N.N.; Alcântara, E.H.; Da Silva Rotta, L.H.; Utsumi, A.G. Signal classification of submerged aquatic vegetation based on the hemispherical-conical reflectance factor spectrum shape in the yellow and red regions. *Remote Sensing* **2013**, *5*, 1856-1874, doi:10.3390/rs5041856.
334. Wilson, K.L.; Skinner, M.A.; Lotze, H.K. Eelgrass (Zostera marina) and benthic habitat mapping in Atlantic Canada using high-resolution SPOT 6/7 satellite imagery. *Estuarine, Coastal and Shelf Science* **2019**, *226*, doi:10.1016/j.ecss.2019.106292.
335. Yadav, S.; Yoneda, M.; Tamura, M.; Susaki, J.; Ishikawa, K.; Yamashiki, Y. A satellite-based assessment of the distribution and biomass of submerged aquatic vegetation in the optically shallow basin of Lake Biwa. *Remote Sensing* **2017**, *9*, 966, doi:10.3390/rs9090966.
336. Yang, C.; Everitt, J.H. Mapping three invasive weeds using airborne hyperspectral imagery. *Ecological Informatics* **2010**, *5*, 429-439, doi:10.1016/j.ecoinf.2010.03.002.
337. Yuan, L.; Zhang, L.Q. Mapping large-scale distribution of submerged aquatic vegetation coverage using remote sensing. *Ecological Informatics* **2008**, *3*, 245-251, doi:10.1016/j.ecoinf.2008.01.004.
338. Zhang, X. On the estimation of biomass of submerged vegetation using Landsat thematic mapper (TM) imagery: a case study of the Honghu Lake, PR China. *International Journal of Remote Sensing* **1998**, *19*, 11-20.
339. Zhao, D.; Jiang, H.; Yang, T.; Cai, Y.; Xu, D.; An, S. Remote sensing of aquatic vegetation distribution in Taihu Lake using an improved classification tree with modified thresholds. *Journal of Environmental Management* **2012**, *95*, 98-107, doi:10.1016/j.jenvman.2011.10.007.
340. Zharikov, V.V.; Bazarov, K.Y.; Egidarev, E.G. Use of remotely sensed data in mapping underwater landscapes of Srednyaya Bay (Peter the Great Gulf, Sea of Japan). *Geography and Natural Resources* **2017**, *38*, 188-195, doi:10.1134/S187537281702010X.
341. Zheng, Y.H.; Duarte, C.M.; Chen, J.; Li, D.; Lou, Z.H.; Wu, J.P. Remote sensing mapping of macroalgal farms by modifying thresholds in the classification tree. *Geocarto International* **2019**, *34*, 1098-1108, doi:10.1080/10106049.2018.1474272.
342. Zou, W.; Yuan, L.; Zhang, L. Analyzing the spectral response of submerged aquatic vegetation in a eutrophic lake, Shanghai, China. *Ecological Engineering* **2013**, *57*, 65-71, doi:10.1016/j.ecoleng.2013.04.008.
343. Harper, M.; Mejbel, H.S.; Longert, D.; Abell, R.; Beard, T.D.; Bennett, J.R.; Carlson, S.M.; Darwall, W.; Dell, A.; Domisch, S., et al. Twenty-five essential research questions to inform the protection and restoration of freshwater biodiversity. *Aquatic Conservation: Marine and Freshwater Ecosystems* **2021**, *n/a*, doi:10.1002/aqc.3634.

344. Asner, G.; Knapp, D.; Balaji, A.; Paez-Acosta, G. Automated mapping of tropical deforestation and forest degradation: CLASlite. *Journal of Applied Remote Sensing* **2009**, *3*, 033543.
345. Johansen, K.; Duan, Q.; Tu, Y.H.; Searle, C.; Wu, D.; Phinn, S.; Robson, A.; McCabe, M.F. Mapping the condition of macadamia tree crops using multi-spectral UAV and WorldView-3 imagery. *ISPRS Journal of Photogrammetry and Remote Sensing* **2020**, *165*, 28-40, doi:10.1016/j.isprsjprs.2020.04.017.
346. Sanders, J.T.; Jones, E.A.L.; Minter, A.; Austin, R.; Roberson, G.T.; Richardson, R.J.; Everman, W.J. Remote Sensing for Italian Ryegrass [Lolium perenne L. ssp. multiflorum (Lam.) Husnot] Detection in Winter Wheat (Triticum aestivum L.). *Frontiers in Agronomy* **2021**, *3*, doi:10.3389/fagro.2021.687112.
347. Cochrane, M.A. Using vegetation reflectance variability for species level classification of hyperspectral data. *International Journal of Remote Sensing* **2000**, *21*, 2075-2087, doi:10.1080/01431160050021303.
348. Clark, M.L.; Roberts, D.A.; Clark, D.B. Hyperspectral discrimination of tropical rain forest tree species at leaf to crown scales. *Remote Sensing of Environment* **2005**, *96*, 375-398, doi:10.1016/j.rse.2005.03.009.
349. Martin, M.E.; Newman, S.D.; Aber, J.D.; Congalton, R.G. Determining forest species composition using high spectral resolution remote sensing data. *Remote Sensing of Environment* **1998**, *65*, 249-254, doi:10.1016/S0034-4257(98)00035-2.
350. Arroyo-Mora, J.P.; Kalacska, M.; Løke, T.; Schläpfer, D.; Coops, N.C.; Lucanus, O.; Leblanc, G. Assessing the impact of illumination on UAV pushbroom hyperspectral imagery collected under various cloud cover conditions. *Remote Sensing of Environment* **2021**, *258*, 112396, doi:10.1016/j.rse.2021.112396.
351. Rowan, G.S.L.; Kalacska, M. A Review of Remote Sensing of Submerged Aquatic Vegetation for Non-Specialists. *Remote Sensing* **2021**, *13*, 623, doi:10.3390/rs13040623.
352. Uudeberg, K.; Ansko, I.; Põru, G.; Ansper, A.; Reinart, A. Using Optical Water Types to Monitor Changes in Optically Complex Inland and Coastal Waters. *Remote Sensing* **2019**, *11*, 2297.
353. Castro-Esau, K.L.; Sánchez-Azofeifa, G.A.; Rivard, B.; Wright, S.J.; Quesada, M. Variability in leaf optical properties of Mesoamerican trees and the potential for species classification. *American Journal of Botany* **2006**, *93*, 517-530, doi:https://doi.org/10.3732/ajb.93.4.517.
354. The St. Lawrence Seaway Management Corporation; Saint Larence Seaway Development Corporation. The St. Lawrence Seaway 2019 Traffic Report. Availabe online: https://greatlakes-seaway.com/wp-content/uploads/2020/03/traffic_report_2019_en.pdf (accessed on 09-09-2021).
355. International Joint Commission. St. Lawrence River: Area of Concern Status Assessment. . Availabe online: https://ijc.org/sites/default/files/C185.pdf (accessed on June 28 2021).
356. Pagnucco, K.S.; Maynard, G.A.; Fera, S.A.; Yan, N.D.; Nalepa, T.F.; Ricciardi, A. The future of species invasions in the Great Lakes-St. Lawrence River basin. *Journal of Great Lakes Research* **2015**, *41*, 96-107, doi:10.1016/j.jglr.2014.11.004.
357. Raisin Region Conservation Authority. Wildlife and Habitat Restoration. . Availabe online: https://www.rrca.on.ca/page.php?id=21 (accessed on June 28 2021).
358. Ministere de l'Environment et de la Lutte Contre les Changements Climatiques. Entente sur les Ressources en Eaux Durables du Bassin des Grands Lacs et du Fleuve Saint-

Laurent. . Availabe online: https://www.environnement.gouv.qc.ca/eau/grandslacs/2005/ (accessed on July 1 2021).
359. Township of South Stormont. Zoning. Availabe online: https://www.southstormont.ca/en/business-and-development/zoning.aspx (accessed on 09-09-2021).
360. Rasky, H. St. Lawrence Seaway: Let the flooding begin. . In *CBC Newsmagazine*, Canada, 1954.
361. Crow, G.E.; Hellquist, C.B.; Fassett, N.C. *Aquatic and wetland plants of northeastern North America: a revised and enlarged edition of Norman C. Fassett's a manual of aquatic plants.* ; University of Wisconsin Press.: Madison, 2000.
362. Knipling, E.B. Physical and physiological basis for the reflectance of visible and near-infrared radiation from vegetation. *Remote Sensing of Environment* **1970**, *1*, 155-159, doi:10.1016/S0034-4257(70)80021-9.
363. Kalacska, M. Emlid GPS NTRIP Protocol. *Protocols.io* **2018**, 10.17504/protocols.io.qs8dwhw, doi:10.17504/protocols.io.qs8dwhw.
364. Devijver, P.A.; Kittler, J. *Pattern recognition: a statistical approach*; Prentice/Hall International.: Englewood Cliffs, N.J., 1982.
365. Duin, R.P.W.; Pekalska, E. Pattern Recognition: Introduction and Terminology. . 2016.
366. Inamdar, D.; Kalacska, M.; Leblanc, G.; Arroyo-Mora, J.P. Implementation of the directly-georeferenced hyperspectral point cloud. *MethodsX* **2021**, *8*, 101429, doi:10.1016/j.mex.2021.101429.
367. Inamdar, D.; Kalacska, M.; Arroyo-Mora, J.P.; Leblanc, G. The Directly-Georeferenced Hyperspectral Point Cloud: Preserving the Integrity of Hyperspectral Imaging Data. *Frontiers in Remote Sensing* **2021**, *2*, doi:10.3389/frsen.2021.675323.
368. Scharf, L.L.; McWhorter, L.T. Adaptive matched subspace detectors and adaptive coherence estimators. In Proceedings of Conference Record of The Thirtieth Asilomar Conference on Signals, Systems and Computers, 3-6 Nov. 1996; pp. 1114-1117 vol.1112.
369. Elmer, K.; Kalacska, M. A High-Accuracy GNSS Dataset of Ground Truth Points Collected within Îles-de-Boucherville National Park, Quebec, Canada. *Data* **2021**, *6*, 32, doi:10.3390/data6030032.
370. Danylo, O.; Pirker, J.; Lemoine, G.; Ceccherini, G.; See, L.; McCallum, I.; Hadi; Kraxner, F.; Achard, F.; Fritz, S. A map of the extent and year of detection of oil palm plantations in Indonesia, Malaysia and Thailand. *Scientific Data* **2021**, *8*, 96, doi:10.1038/s41597-021-00867-1.
371. Werdell, P.J.; Behrenfeld, M.J.; Bontempi, P.S.; Boss, E.; Cairns, B.; Davis, G.T.; Franz, B.A.; Gliese, U.B.; Gorman, E.T.; Hasekamp, O., et al. The Plankton, Aerosol, Cloud, Ocean Ecosystem Mission: Status, Science, Advances. *Bulletin of the American Meteorological Society* **2019**, *100*, 1775-1794, doi:10.1175/bams-d-18-0056.1.
372. Salisbury, F.B.; Ross, C.W. *Plant Physiology*; Wadworth Publishing Company.: Belmont, California, 1992.
373. Gitelson, A.; Merzlyak, M.N. Spectral Reflectance Changes Associated with Autumn Senescence of Aesculus hippocastanum L. and Acer platanoides L. Leaves. Spectral Features and Relation to Chlorophyll Estimation. *Journal of Plant Physiology* **1994**, *143*, 286-292, doi:10.1016/S0176-1617(11)81633-0.

374. Maksimović, T.; Lolić, S.; Kukavica, B. Seasonal Changes in the Content of Photosynthetic Pigments of Dominant Macrophytes in the Bardača Fishpond Area. *Ekológia (Bratislava)* **2020**, *39*, 201-213, doi:doi:10.2478/eko-2020-0015.
375. UC Museum of Paleontology. Photosynthetic Pigments. Availabe online: https://ucmp.berkeley.edu/glossary/gloss3/pigments.html (accessed on July 26th 2021).
376. Cavender-Bares, J.; Meireles, J.E.; Couture, J.J.; Kaproth, M.A.; Kingdon, C.C.; Singh, A.; Serbin, S.P.; Center, A.; Zuniga, E.; Pilz, G., et al. Associations of Leaf Spectra with Genetic and Phylogenetic Variation in Oaks: Prospects for Remote Detection of Biodiversity. *Remote Sensing* **2016**, *8*, 221, doi:doi:10.3390/rs8030221.
377. Laliberté, E.; Schweiger, A.K.; Legendre, P. Partitioning plant spectral diversity into alpha and beta components. *Ecology Letters* **2020**, *23*, 370-380, doi:10.1111/ele.13429.
378. Inamdar, D.; Rowan, G.S.L.; Kalacska, M.; Arroyo-Mora, J.P. Water Column Compensation Workflow for Hyperspectral Imaging Data. *MethodsX* **subm**.
379. Mumby, P.J.; Clark, C.D.; Green, E.P.; Edwards, A.J. Benefits of water column correction and contextual editing for mapping coral reefs. *International Journal of Remote Sensing* **1998**, *19*, doi:10.1080/014311698216521.
380. Kraut, S.; Scharf, L.L.; Butler, R.W. The adaptive coherence estimator: a uniformly most-powerful-invariant adaptive detection statistic. *Trans. Sig. Proc.* **2005**, *53*, 427–438, doi:10.1109/tsp.2004.840823.
381. Macfarlane, F.; Murray, P.; Marshall, S.; White, H. Investigating the Effects of a Combined Spatial and Spectral Dimensionality Reduction Approach for Aerial Hyperspectral Target Detection Applications. *Remote Sensing* **2021**, *13*, 1647, doi:10.3390/rs13091647.
382. Jerlov, N.G. Classification of sea water in terms of quanta irradiance. *ICES Journal of Marine Science* **1977**, *37*, 281-287, doi:10.1093/icesjms/37.3.281.
383. Morel, A.; Prieur, L. Analysis of variations in ocean color1. *Limnology and Oceanography* **1977**, *22*, 709-722, doi:https://doi.org/10.4319/lo.1977.22.4.0709.
384. McKee, D.; Cunningham, A.; Dudek, A. Optical water type discrimination and tuning remote sensing band-ratio algorithms: Application to retrieval of chlorophyll and Kd(490) in the Irish and Celtic Seas. *Estuarine, Coastal and Shelf Science* **2007**, *73*, 827-834, doi:https://doi.org/10.1016/j.ecss.2007.03.028.